

Dissertation
submitted to the
Combined Faculties for the Natural Sciences and for Mathematics
of the Ruperto-Carola University of Heidelberg, Germany
for the degree of
Doctor of Natural Sciences

presented by
Dipl.-Phys. Henrik Buhr
born in Heidelberg
Oral examination: July 26th, 2006

Electron collisions and internal excitation in stored molecular ion beams

Referees:

Prof. Dr. Andreas Wolf
Prof. Dr. Peter Schmelcher

Kurzfassung

Elektronenstöße und interne Anregung schneller gespeicherter Molekülionen

In Speicherring-Experimenten untersuchen wir Stöße von Elektronen mit Molekülionen, deren innere Anregung und, wie sich diese beiden Aspekte gegenseitig beeinflussen. Für He_2^+ werden besonders dissoziative Rekombination und superelastische Stöße betrachtet. Der DR-Ratenkoeffizient hängt sehr stark von der Vibrationsanregung des Molekülions vor dem Stoß ab. Deshalb ist man durch die Messung des DR-Ratenkoeffizienten in der Lage, sehr kleine Veränderungen in der mittleren Vibrationsanregung von He_2^+ durch Stöße mit Elektronen oder Restgas zu beobachten, wovon in dieser Arbeit Gebrauch gemacht wird.

Der DR-Ratenkoeffizient von HD^+ weist im Bereich niedriger Elektronenenergie zahlreiche Resonanzen aus dem indirekten DR Prozess auf, die durch das Zusammenspiel von Rotationsleveln im Molekülion und in Rydberg-Zuständen des neutralen Moleküls entstehen. Mit einem hier neu entwickelten Verfahren zur hochauflösenden Elektronenstoßspektroskopie können die Resonanzen im DR-Ratenkoeffizienten mit hoher Energieselektivität gemessen werden. Dies erlaubt den detaillierten Vergleich mit den Ergebnissen einer MQDT-Rechnung und den Versuch, die Resonanzen einzelnen intermediären Rydberg-Zuständen zuzuordnen.

Abstract

Electron collisions and internal excitation in stored molecular ion beams

In storage ring experiments the role, which the initial internal excitation of a molecular ion can play in electron collisions, and the effect of these collisions on the internal excitation are investigated. Dissociative recombination (DR) and inelastic and super-elastic collisions are studied in the system of He_2^+ . The DR rate coefficient at low energies depends strongly on the initial vibrational excitation in this system. Therefore changes in the DR rate coefficient are a very sensitive probe for changes in the vibrational excitation in He_2^+ , which is used to investigate the effects of collisions with electrons and residual gas species.

The low-energy DR of HD^+ is rich with resonances from the indirect DR process, when certain initial rotational levels in the molecular ion are coupled to levels in neutral Rydberg states lying below the ion state. Using new procedures for high-resolution electron-ion collision spectroscopy developed here, these resonances in the DR cross section can be measured with high energy sensitivity. This allows a detailed comparison with results of a MQDT calculation in an effort to assign some or all of the resonances to certain intermediate Rydberg levels.

Contents

1	Introduction	1
2	Electron-molecular ion reactions at small energies	5
2.1	Born-Oppenheimer approximation and potential energy surfaces	5
2.2	Molecule-electron reactions	6
2.2.1	Dissociative recombination	6
2.2.2	More electron-molecular ion reactions	8
2.3	Collisions of fast molecular ions with residual gas species	10
2.4	Franck-Condon suppressed direct DR in He_2^+	10
2.4.1	Previous studies of the DR of He_2^+	11
2.4.2	The latest theoretical treatments of He_2^+ DR	13
2.4.3	Experimental goals	14
2.5	HD^+ , the indirect process and low energy rotational resonances	15
2.5.1	Earlier experimental results on the low-energy DR of HD^+	15
2.5.2	Other electron collisions studied with HD^+	17
2.5.3	A simple model to predict the positions of resonances	18
3	Experimental method	27
3.1	Ion production, acceleration and storage	27
3.2	Vibrational excitation diagnostics	29
3.2.1	Principles of foil-induced Coulomb Explosion Imaging	29
3.2.2	The CEI Setup	31
3.3	Standard collision experiments at the TSR	33
3.3.1	Ion beam preparation and temperature of a merged electron beam	33
3.3.2	Detectors at the TSR electron cooler	34
3.3.3	Energy dependent collision measurements with the electron cooler	35
3.4	A new arrangement for high resolution collision experiments	37

3.4.1	The ultra-cold electron beam device	37
3.4.2	A beamline for advanced molecular breakup imaging (BAMBI)	39
3.4.3	New fragment detector station	40
3.4.4	The new data acquisition system	42
4	Franck-Condon suppressed dissociative recombination in He_2^+	45
4.1	Vibrational excitation as a function of time in He_2^+ – CEI results	45
4.1.1	The infrared-active, heteronuclear $^3\text{He}^4\text{He}^+$	46
4.1.2	The homonuclear $^4\text{He}_2^+$	47
4.2	Absolute DR rate coefficients at high electron energy	49
4.2.1	A method for an absolute normalization without measuring the ion current	50
4.2.2	Absolute rate coefficients of both He_2^+ species	53
4.2.3	Comparison to other experiments and to theory	57
4.3	Rovibrational cooling by electron collisions	57
4.3.1	Time dependence of the DR rate coefficient of $^4\text{He}_2^+$	57
4.3.2	Vibrational state dependent DR rate coefficients $\alpha_{DR}^v(0\text{eV})$ and SEC in $^4\text{He}_2^+$	59
4.3.3	Time dependent DR rate coefficient of $^3\text{He}^4\text{He}^+$ at 0 eV – rotational SEC	62
4.4	Rovibrational excitation by electron collisions	63
4.5	Rovibrational excitation by residual gas collisions	66
4.6	Energy dependent DR rate coefficients of He_2^+	68
4.6.1	Time dependence of $\alpha_{DR}(E_d)$ in $^4\text{He}_2^+$	68
4.6.2	High energy structures in the DR rate coefficient of He_2^+	70
4.7	Summary	72
5	Rotational resonances in the recombination of HD^+	75
5.1	Measurements with two electron beam devices	75
5.1.1	Ion beam dragging with one and two electron beams	75
5.1.2	Stability of the relative electron beam velocity	77
5.2	Improved energy resolution with electron target and photocathode	79
5.3	Comparison to MQDT	83
5.4	Time dependence in HD^+ DR	85
5.5	Summary	90
6	Summary and outlook	91

6.1	He ₂ ⁺ as a probe for rovibrational excitation	91
6.2	Improvement of the energy resolution seen with DR of HD ⁺	92
6.3	Opportunities with the new system	92
6.4	Future experiments	93
References		95

1. Introduction

Molecular ions appear in plasmas [KTS⁺98, DMCL76], in the top layers of the atmosphere [PHT⁺05] and in interstellar clouds [MGHO98]. In plasmas they are usually created in a high temperature environment which leads to molecules with a lot of internal excitation in the form of rotations and vibrations. In interstellar clouds, however, the same molecules can cool down to extremely low internal temperatures, if radiative transitions are allowed, freezing out or quenching all vibrational and rotational levels apart from the ground state. One example is H_3^+ , which is a key molecular ion in interstellar clouds [MGHO98], for which internal temperatures between 25 and 50 K were observed in dense clouds [MGHO99].

A very important loss process for the molecular ions is the dissociative recombination (DR) with electrons that leads to break up into neutral fragments and it occurs in the above mentioned environments. It even occurs in fusion plasmas in tokamak reactors [KTS⁺98] and thus is of technical interest. In storage rings this process can be studied under well defined conditions regarding the collision energy. Infrared-active molecular ions also can deexcite to reach a thermal population of vibrational and rotational levels at 300 K, reducing drastically the range of involved initial states. Even evidence for subthermal rotational temperatures in D_2H^+ were observed reached by interaction with an intense electron beam [LKL⁺03]. The very fast recombining, highly excited levels were depleted, while molecular ions with low excitation and DR rate coefficient remained.

For H_3^+ the DR rate coefficient at very low collision energy was not known for sure, because many experiments yielded results orders of magnitude different from each other. It was concluded that this must be due to different rovibrational excitation present in the H_3^+ ions. When two storage rings experiments succeeded to produce rotational ground state H_3^+ with different methods [MHS⁺04, KMM⁺05] they measured the same dissociative recombination rate coefficient. This is just one, but a very prominent, example for the influence of internal excitation on the dissociative recombination.

The helium dimer ion He_2^+ is another system in which the dissociative recombination rate coefficient with meV-electrons was measured to be extremely low [DMCL76] and quite high [JG72] in different experiments. The reason seems to be a very strong dependence of the rate coeffi-

cient on the vibrational excitation of the molecular ion: Excited molecular ions were found to be recombining fast, while He_2^+ in the vibrational ground state yielded a very small rate coefficient for dissociative recombination. The explanation lies in the shape and position of the potential energy curves of the states involved in the process. Excited He_2^+ can easily access a dissociative neutral state of He_2 , whereas helium dimer ions in the vibrational ground state can all but not couple to this neutral state [COS99].

Depending on whether it is formed by different He isotopes ($^3\text{He}^4\text{He}^+$) or not (like in $^4\text{He}_2^+$), radiative transitions are allowed or not. The heteronuclear species will adopt the temperature of the surrounding within seconds, if it is left undisturbed. In the storage ring TSR at Heidelberg this is 300 K – resulting in a vibrational ground state population of more than 99.99 % [PBA⁺05]. So this isotopomer seems to be ideal to study the properties of the vibrational ground state. It also makes comparisons to theoretical results easier, because one needs to take into account only one vibrational level.

The homonuclear species $^4\text{He}_2^+$ on the other hand is not subject to radiative thermalization, so one can expect to find vibrationally excited molecular ions even after long times of storage. Such a system is ideal to study effects of the storage and measurement procedures on the excitation of the molecules while the radiative interactions are switched off. During the storage collisions with residual gas or with electrons of all kinds of energies can influence the excitation (Secs. 4.4 and 4.5). And with the strong dependence of the rate coefficient of dissociative recombination on vibrational excitation, one has a very sensitive probe of changes in the excitation. In addition, the vibrational excitation can be observed directly at the TSR using the foil-induced Coulomb explosion imaging technique. This is not so sensitive for small changes, but can yield relative numbers on the populations, not only changes. With these tools it seems possible to extract rate coefficients for several vibrational levels.

The dissociative recombination and other reactions with electrons like super-elastic collisions and ion-pair formation have been studied intensively for H_2^+ [TTK⁺99, KAB⁺00, Kro02], D_2^+ [LCD⁺94, Kro02] and HD^+ [ARD⁺03, TKK⁺95, Lan01, LDZ⁺00] in merged beam experiments in storage rings. These are the simplest molecular ions and as such the benchmark case for comparisons of theory and experiment. Therefore there is also a large number of theoretical treatments of the dissociative recombination for this ion with e. g. a configuration mixing ansatz [Bar68] or using a multichannel quantum defect (MQDT) approach [GBD83, NTN87, Tak93, SSC⁺97]. Super-elastic collisions were also treated in the latter context [NMF⁺03, NTN87] or with a molecular R-matrix [ST93]. Ion-pair formation [LO01] was recently studied, too.

The average rate coefficient of dissociative recombination can be predicted very well. But in

addition, a large number of low energy resonances from coupling to rotational levels in neutral Rydberg states (Secs. 2.2.1 and 2.5) was measured. These resonances are not well reproduced by the theoretical results, especially compared to the precision with which resonances in dielectronic recombination of atomic ions can be predicted in shape, strength and energy, e. g. for F^{6+} [TEG⁺02] which consists of one particle more than HD^+ , but of course lacks the vibrational and rotational degrees of freedom of a molecule. Even the origins of the resonances in the dissociative recombination of HD^+ , i. e. the exact states involved, are not known for most of the measured low energy resonances. With the existing experimental data, an unambiguous assignment is not possible. A measurement with higher resolution, which defines better the energy of the existing resonances and perhaps observes new ones, could give new momentum to theory, to come forward with labelings of the calculated resonance structures which then hopefully can be assigned to the experimental data, too.

At the TSR, the new electron target [Spr04] in combination with a liquid nitrogen cooled photocathode [OWS⁺04] provide an ultra-cold electron beam. In combination with a new neutral fragment detector setup (Sec. 3.4) this allows to re-measure the DR rate coefficient of HD^+ with a unprecedented energy resolution (Sec. 5). With these experimental data a new comparison to the theoretical results can be undertaken.

2. Electron-molecular ion reactions at small energies

Molecular dynamics and processes in molecules are often considered in terms of potential energy surfaces. The concept of these is introduced in the following section. Potential energy surfaces help us to discuss then reactions between molecular ions and electrons like *dissociative recombination*. Also collisions with residual gas species are specified. The helium dimer ion He_2^+ serves as an example for the direct dissociative recombination mechanism. Existing results on the molecular ion are shortly described.

The indirect dissociative recombination mechanism is important in HD^+ , where a large number of resonances in low energy collisions with electrons exist. A simple model for the prediction and thus labeling of these resonances is introduced.

2.1 Born-Oppenheimer approximation and potential energy surfaces

The most common ansatz for the description of the behaviour of molecular systems is the Born-Oppenheimer approximation [BO27]. The many-body problem is simplified by the assumption that the electrons react instantaneously to the movement of the much heavier nuclei. Therefore the electronic motion can be separated from the nuclear motion. The electronic motion is treated with static nuclei, i. e. the electronic Schrödinger equation is solved for a potential with fixed nuclear positions that enter the calculations only as parameters. The resulting Eigenvalues of the electronic energy depend on the nuclear configuration.

In a second step, the nuclear Schrödinger equation is solved for the potential energy surfaces (PES) formed for each electronic state by the sum of electronic Eigenenergy and the potential energy of the nuclear configuration. The solutions describe the nuclear motion. Minima in the PES describe equilibrium configurations.

The Born-Oppenheimer approximation yields good or reasonable results, if the PES of equal symmetry are well separated in energy. If the PES become almost or completely degenerate, i. e. if they cross at certain nuclear configurations, electronic and nuclear motion are coupled in

this situation and the approximation breaks down. In that case, the picture of the nuclear motion being governed by the PES of a single electronic state becomes invalid.

The PES of a molecule formed by n atoms are hypersurfaces in a $(3n-5)$ dimensional space ($3n-4$ for linear molecules). Thus, in the case of diatomic molecules like HD^+ , the PES becomes a potential curve, a function of the internuclear distance only.

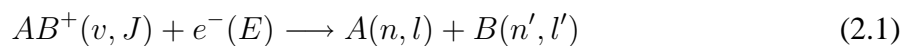
2.2 Molecule-electron reactions

A low-energy electron can interact with a molecular ion in several ways, leading to completely different types of final products. Elastic collisions leave the internal structure of the molecular ion completely unchanged. Inelastic collisions (IC) and *super-elastic collisions* (SEC) can change the rovibrational state of the molecular ion, while leaving the molecule intact. *Dissociative recombination* (DR) is the capture of an electron by a molecular ion with subsequent dissociation into neutral fragments. *Dissociative excitation* (DE) happens when the collision fragments the molecular ion into neutral and charged particles, while the electron escapes.

2.2.1 Dissociative recombination

Dissociative recombination occurs in plasmas and afterglows [IS88, DMCL76] and can be observed outside of laboratories in interstellar clouds (e. g. H_3^+ [HK73]) or in the atmosphere (e. g. O_2^+ [PHT⁺05]).

For a diatomic molecular ion with v vibrational quanta of excitation and J rotational quanta, the process can be written as



where E is the incident electron energy and n, n', l and l' are the principal and orbital angular momentum quantum numbers of the atomic final states. The reaction shows, that there are several parameters that can influence the process, and that there is also the possibility of multiple final states with different kinetic energy releases (KER). DR rate coefficient, KER and branching ratios of different final channels can be studied as function of electron energy and, to a degree, initial rovibrational excitation of the molecular ions. In addition to the above mentioned parameters, a possible dependence on the angle between molecular axis and electron velocity is of interest ([Gub83, Noved]).

The simplest model explaining the occurrence of the DR process is the *direct* process, where the electron is captured into a doubly excited neutral state AB^{**} , from which it dissociates into

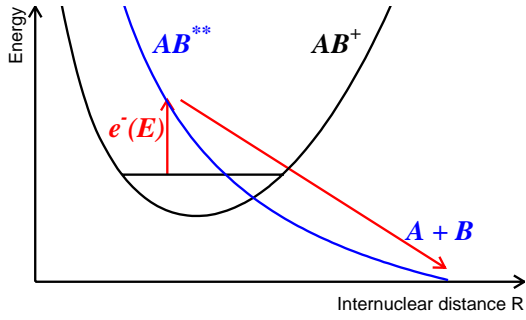
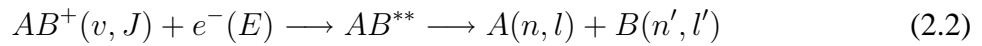


Fig. 2.1: Illustration of the direct DR process of a diatomic molecular ion AB^+ with an electron of energy E . The molecular ion potential energy surface (PES) is marked in black, the neutral dissociative PES in blue.

neutral fragments



This two-step process is illustrated in Fig. 2.1. The involved PES are those of the bound ionic state and of the repulsive state of AB^{**} . The electron capture is stabilized by rapid dissociation along the repulsive PES. The direct mechanism at low electron energies needs the existence of a suitable PES of a doubly excited state featuring a favourable curve crossing with the bound molecular state PES. H_2^+ and its isotopomers are examples for molecular ions in which such a curve crossing is found and where the direct mechanism is a working model [Lar97]. Such a curve crossing means, that the nuclear wave functions of the bound molecular ion state $\Psi_{AB^+}(R, v)$ and the neutral dissociative state $\Psi_{AB^{**}}(R, E_t)$ have a good overlap, if the energy of the bound level is close to the energy at which the curve crossing occurs. The overlap is called the Franck-Condon factor $f(v, E_t)$ of the two wave functions $\Psi_{AB^+}(R, v)$ and $\Psi_{AB^{**}}(R, E_t)$ and is defined as:

$$f(v, E_t) = \int \Psi_{AB^+}^*(R, v) \Psi_{AB^{**}}(R, E_t) dR \quad (2.3)$$

The direct DR cross section $\sigma_{DR,direct}$ depends strongly on the Franck-Condon factor. Under certain conditions, the direct process cross section can be written as [Giu89]:

$$\sigma_{DR,direct} = \frac{const. \cdot r}{k^2} f(v, E_t)^2 \cdot V_{el}^2 \cdot S \quad (2.4)$$

where r is the multiplicity ratio between final (neutral) and initial (molecular ion) electronic states and k is the collision wavenumber. These conditions are, that there is only one dissociative curve per symmetry, that the electronic coupling V_{el} between bound and dissociative state does not vary strongly in the overlap region of the two wave functions, and that the quantum defect $\mu(R)$ varies slowly with the internuclear distance [Giu89, Sch06]. The Franck-Condon factor governs the electron capture as the first step of the direct DR, while the second part is called the survival factor S describing the loss in the DR channel due to autoionization.

2 Electron-molecular ion reactions at small energies

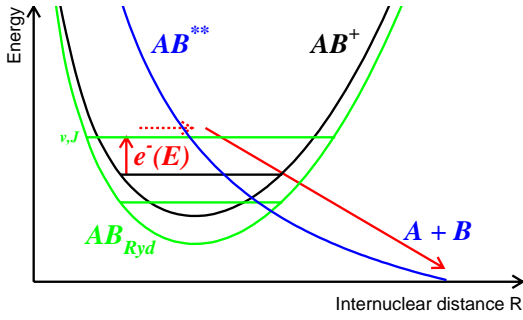
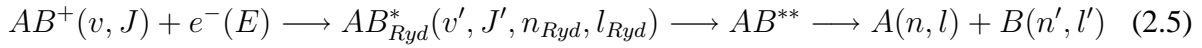


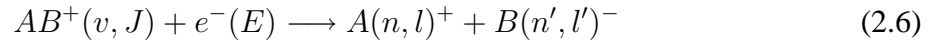
Fig. 2.2: Illustration of the indirect DR process of a diatomic molecular ion AB^+ with an electron of energy E . The molecular ion potential energy surface (PES) is marked in black, the neutral dissociative PES in blue and the Rydberg state in green. The upper green horizontal line marks the intermediate rovibrationally excited level in the Rydberg state.

In addition to the direct process also indirect mechanisms can contribute to DR. In systems like HeH^+ and H_3^+ suitable PES do not exist at low electron energies, yet they recombine efficiently [Lar97], due to non-adiabatic couplings. Moreover, indirect processes can be responsible for low energy resonances as was suggested in the case of H_2^+ [GBD83, SSC⁺97]. By coupling of electronic and vibrational motion, capture happens into vibrationally excited molecular Rydberg states, which then couple to a dissociative state (Fig. 2.2):



The Rydberg states are described by the quantum numbers v' and J' for vibrational and rotational excitation of the ionic core and the principal and orbital angular momentum quantum numbers n_{Ryd} and l_{Ryd} of the excited electron. Below each of the ionic PES lies a series of neutral Rydberg states converging towards the ionic state and each of these states includes basically the same vibrational and rotational levels as the ionic state. Total angular momentum conservation, considering both the continuum and the resonance state, then leads to selection rules for the formation of resonances of $|\Delta J| = |J' - J| \leq 2 \cdot l_{Ryd}$ [SSC⁺97].

If the doubly excited state AB^{**} PES asymptotically leads to an ion-pair instead of two neutrals, or if during dissociation it couples to a neutral state that does, then (resonant) ion-pair production can be observed



It was recently observed for HD^+ [LDZ⁺00] and a theoretical treatment of the process was published by Larson *et al.* [LO01]. Analysis of measurements of the ion-pair formation of H_3^+ and CF^+ at the TSR are on the way [Hofed].

2.2.2 More electron-molecular ion reactions

Inelastic and super-elastic collisions (IC and SEC, respectively) are non-destructive processes, that increase or decrease the internal excitation of the molecule. For our diatomic molecular ion

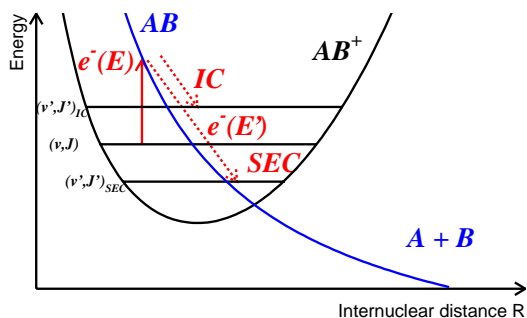


Fig. 2.3: Illustration of the inelastic collision (IC) and SEC process of a diatomic molecular ion AB^+ with an electron of energy E . The molecular ion potential energy surface (PES) is marked in black, the neutral dissociative PES in blue. The two dashed arrows indicate the energy of the electron for IC and SEC, respectively.

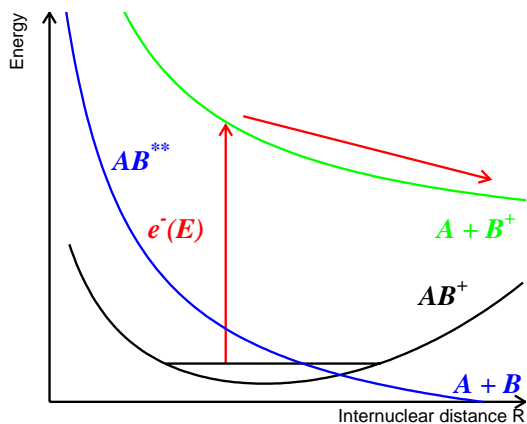
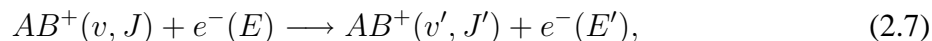


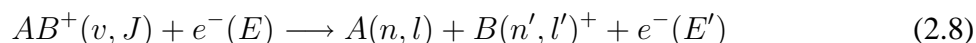
Fig. 2.4: Illustration of the DE process of a diatomic molecular ion AB^+ with an electron of energy E . The molecular ion potential energy surface (PES) is marked in black, the neutral dissociative PES in blue.

they are written as



where E' is the final electron energy and v' and J' are the rovibrational quantum numbers of the molecular ion after the collision. If $E > E'$, then we speak of an inelastic collision, while we call the process SEC, if $E < E'$ (Fig. 2.3). Vibrational SEC, i. e. reactions reducing the quantum number v , was observed in H_2^+ [TTK⁺99, KAB⁺00] and D_2^+ [Kro02] and it was also treated theoretically several times [NMF⁺03, ST93, NTN87].

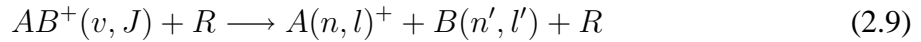
Electron-molecule collisions that lead to dissociation without capture of the electron (Fig. 2.4) are called dissociative excitation (DE). In the diatomic case, the products are one positively charged ion and one neutral



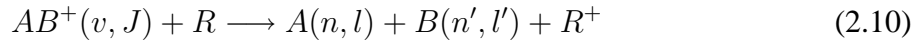
This process usually does not occur in collisions with electrons of very low energy, because the potential energy of the bound molecular ion is lower than the energy of the two free fragments.

2.3 Collisions of fast molecular ions with residual gas species

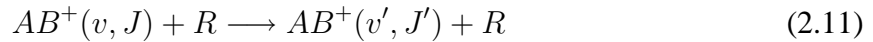
In storage ring experiments high-energy collisions in the MeV range between the stored molecular ion and the residual gas species occur everywhere in the ring. A very low residual gas pressure reduces the probability of these collisions to occur. They can, however, have an important influence on storage ring experiments. The process that is most important for molecular ion loss from a fast beam is dissociative excitation by a collision with a molecule or atom of the residual gas R , leading to breakup of the fast molecule into fragments like in the electron-induced DE (Eq. 2.8):



A process occurring with much lower probability is dissociative charge exchange (DC), in which the molecular ion captures an electron from a residual gas molecule in a MeV collision with subsequent dissociation to neutral fragments like in the electron-induced DR



Collisions between the fast molecular ion and the residual gas can be inelastic and non-destructive, too



These collisions permanently excite molecular ions rovibrationally thus disturbing the thermalization of stored ion samples. He_2^+ is an example for a molecular ion for which such collisions can be well observed (Sec. 4.5).

2.4 Franck-Condon suppressed direct DR in He_2^+

The He_2^+ molecular ion is a very interesting system to study the interactions with slow electrons. Unlike in the example PES in Fig. 2.1 there is no appropriate curve crossing to drive the direct DR process at low energies in the helium dimer ion. The lowest curve crossing between the molecular ion ground state PES and a neutral PES is found approximately at the $v=3$ vibrational level of the ion which is illustrated in Fig. 2.5. In addition the squares of the spatial wave functions of the molecular ion state $\Psi_{AB^+}(R, v)$ are shown for $v=0$ and $v=3$ (black lines) together with that of one of the neutral dissociative states $\Psi_{AB^{**}}(R, E_t)$ at the corresponding energies (green).

The wave function for He_2^+ in the vibrational ground state $v=0$ has very small overlap with the continuous neutral state in this case. Since the direct process DR cross section depends strongly

on the Franck-Condon factor (Eq. 2.4) between the spatial wave function of the molecular ion state $\Psi_{AB^+}(R, v)$ and the neutral state $\Psi_{AB^{**}}(R, E_t)$, this leads to the expectation that the direct process is only of little importance in the DR of ground state He_2^+ at small collision energies. With the vibrational excitation increasing to $v=3$, the overlap becomes much larger and the cross sections can be expected to be orders of magnitude higher. So for low vibrational levels and low electron energies one can speak of a Franck-Condon suppression of the DR process. Various studies of the Helium molecule yielded results that support the predictions of this simple model.

2.4.1 Previous studies of the DR of He_2^+

It is the dominant ion in helium plasmas of densities above 5 Torr at room temperature [DMCL76]. Several experiments have published absolute values of the DR rate coefficient α_{DR} , which is linked to the cross section σ_{DR} by $\alpha_{DR} = \sigma_{DR} \cdot v$ where v is the relative velocity of the reactants, here molecular ion and electron. Afterglow experiments by Johnson and Gerardo [JG72] report a DR rate coefficient of $1.1 \cdot 10^{-8} \text{ cm}^3 \text{ s}^{-1}$ at room temperature for pressures of 15 to 56 Torr. In a very sophisticated analysis of Helium afterglow experiments, Deloche et al. [DMCL76] found an upper limit of $5 \cdot 10^{-10} \text{ cm}^3 \text{ s}^{-1}$ at comparable temperatures and pressures ranging from 5 to 100 Torr. Ivanov et al. [IPS83, IS88] found a significant role of DR in the production of excited He atoms in $n=3$ or 4, suggesting a higher DR rate coefficient for

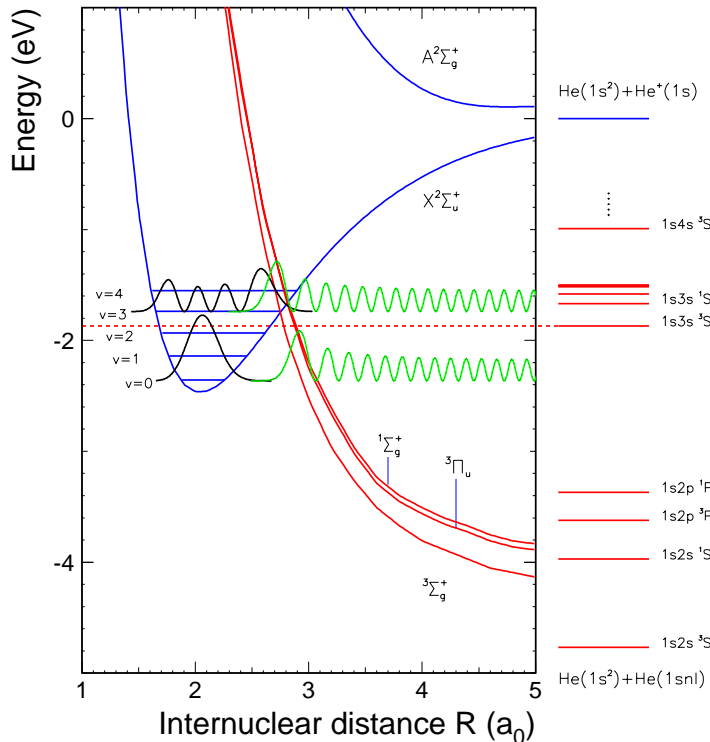


Fig. 2.5: The potential energy curves in the $\text{He}_2/\text{He}_2^+$ -system which are the most relevant in the low energy direct DR process. Blue: He_2^+ electronic ground state [CR95] and first dissociative ground state [AH91], with the lowest vibrational levels shown as horizontal lines. Red: The three lowest relevant dissociative neutral potential curves [COS99, Coh76]. The horizontal lines on the right mark the energies of the atomic limits. The dashed line marks the minimum energy to reach a $\text{He}(1s3nl)$ final state. The black lines show qualitatively the square of the wave function for vibrational levels $v=0$ and $v=3$, the green ones the square of the wave function of the continuum neutral state at the respective energies.

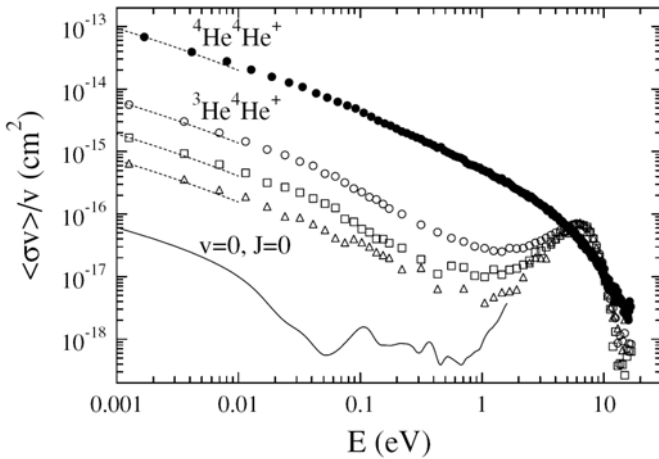


Fig. 2.6: The DR cross section of ${}^3\text{He}^+{}^4\text{He}$ (open markers) and ${}^4\text{He}^+{}^4\text{He}$ (filled) [UDS⁺05] as measured at ASTRID. The times after injection after which the cross sections were measured for ${}^3\text{He}^+{}^4\text{He}$ are: Circles: 4–6 s. Squares: 6–9.5 s. Triangles: 9.5–13.5 s. The full line is a calculation for $v=0, J=0$ for ${}^3\text{He}^+{}^4\text{He}$ [COS99].

vibrationally highly excited He_2^+ , as these atomic states were energetically not accessible from ground state molecules (Fig. 2.5). They already suggested to combine studies of dissociative recombination and of vibrational excitation of the molecular ion in the analysis [IPS83]. They cite a DR rate coefficient for excited $\text{He}_2^+(v \geq 3)$ of $\approx 10^{-6} \text{ cm}^3 \text{ s}^{-1}$ [IS88].

In recent years, merged beam experiments in storage rings were performed. The heteronuclear system ${}^3\text{He}^+{}^4\text{He}$ was in the focus of these studies, because its permanent dipole moment is responsible for a fast relaxation of vibrational excitation, reaching the ground state ($v=0$) within less than 2 seconds. Storage rings allow measurements for up to 100 s, well beyond this time. First storage ring results were published from an experiment carried out at the ASTRID storage ring of Aarhus, quoting an upper limit for the DR rate coefficient of $6 \cdot 10^{-10} \text{ cm}^3 \text{ s}^{-1}$ for 300 K electrons in the case of vibrationally relaxed ${}^3\text{He}^+{}^4\text{He}$ [UDS⁺05]. For ${}^4\text{He}_2^+$, they found a thermal DR rate coefficient of $1.23 \cdot 10^{-7} \text{ cm}^3 \text{ s}^{-1}$. Fig. 2.6 shows the measured DR cross section $\langle \sigma_{DR} v \rangle / v^1$ as function of energy for both isotopomers in the range of collision energies of 0–20 eV. The cross section for ${}^4\text{He}_2^+$ shows no structure up to 10 eV and no change with storage time. A value of $\sigma_{DR}(2 \text{ meV}) = 0.7 \cdot 10^{-13} \text{ cm}^2$ is found. The DR cross section of ${}^3\text{He}^+{}^4\text{He}$ features a strong decrease with time at low energies and a broad peak structure around 6.4 eV [UDS⁺05]. The cross section on the peak is read from the figure to be $\sigma_{DR}(6.4 \text{ eV}) = 0.7 \cdot 10^{-16} \text{ cm}^2$ and near zero energy a value of $\sigma_{DR}(1 \text{ meV}) = 6.5 \cdot 10^{-16} \text{ cm}^2$ is found after 9.5–13.5 s of storage in the ring.

The most recent storage ring experiments were carried out at the TSR in Heidelberg [PBA⁺05, BPA⁺ed], considering both of the above isotopomers. Results of these experiments will be discussed in Chapter 4 in detail.

1 Here v is the electron collision velocity.

2.4.2 The latest theoretical treatments of He_2^+ DR

The most recent theoretical works on the dissociative recombination of He_2^+ were published by Carata et al. [COS99] for electron energies of 0.1 meV to 2 eV and by Royal et al. [RO05] in the range of 1 to 15 eV. Both works focus on the heteronuclear species $^3\text{He}^4\text{He}^+$, since experimental results on this species are easier to compare to, because of the fast spontaneous relaxation of vibrational excitation to the ground state ($v=0$), but Carata also treated the homonuclear cases of $^3\text{He}_2^+$ and $^4\text{He}_2^+$ and Royal applied their formalism to the $^4\text{He}_2^+$ DR later, too.

The low energy study is a multichannel quantum defect theory (MQDT) calculation [COS99]. It makes a detailed study of the influence of vibrational and rotational excitation of the initial molecular ion on the DR cross section. Direct (Eq. 2.2) and indirect DR process (2.5) are included and the electronic coupling of the neutral Rydberg and the doubly excited states is treated with a short-range reaction matrix, a K-matrix, taking into account perturbations up to the second order. Vibrational interactions in the capture into the Rydberg states are included, while the effect of rotational interactions was considered to be very small therefore was neglected in this approach. Initial rotational excitation however is taken into account.

The total (direct+indirect) DR cross sections for $^3\text{He}^4\text{He}$ with vibrational excitation $v=0-4$ in the energy range of $E_d=10^{-4}-2$ eV is given for the rotational ground state $J=0$ as well as for rotationally excited ions with $v=0$ for energies up to 200 meV. At energies very close to 0 eV, there is more than one order of magnitude in the total DR cross section between the levels $v=0$ and $v=1$ and between $v=1$ and $v=2$, increasing with v . The increase in cross section between $v=2, 3$ and 4 is smaller than an order of magnitude per level.

In addition, direct and total DR cross sections are compared showing a considerable isotopic effect for the rovibrational ground state ($v=0, J=0$), with the lightest system $^3\text{He}_2^+$ recombining fastest. The ratio in the direct DR cross section of $^3\text{He}^4\text{He}^+$ and $^4\text{He}_2^+$ from that state is found to be between 2 and 3.5 for collision energies up to 2 eV, the lighter isotope featuring the higher cross section. For the ($v=4, J=0$) state, the isotopic effect on the cross section almost vanishes. For the rovibrational ground state a cross section $\sigma_{DR}(0.026 \text{ eV}) \approx 10^{-18} \text{ cm}^2$ for $^3\text{He}^4\text{He}^+$ is cited, corresponding to a rate coefficient $\alpha_{DR}(0.026 \text{ eV}) \approx 10^{-11} \text{ cm}^3 \text{ s}^{-1}$, an extremely low value compared to the typical values for small molecular ions, which have DR rate coefficients in the range of $\alpha_{DR}(E \approx 0 \text{ eV}) \approx 10^{-7} \text{ cm}^3 \text{ s}^{-1}$.

The high energy calculation is a time dependent wave packet calculation. It treats the collision energy range of $E=1-15$ eV where the cross section is dominated by resonances due to the Rydberg series converging towards the first excited, repulsive state of the molecular ion $^3\text{He}^4\text{He}^+$. The calculated DR cross section for the vibrational level $v=0$ shows one broad peak between 2 and 12 eV, with a maximum of $\sigma_{DR}=6.51 \cdot 10^{-17} \text{ cm}^2$ at 6.75 eV, or $\alpha_{DR}=1 \cdot 10^{-8} \text{ cm}^3 \text{ s}^{-1}$.

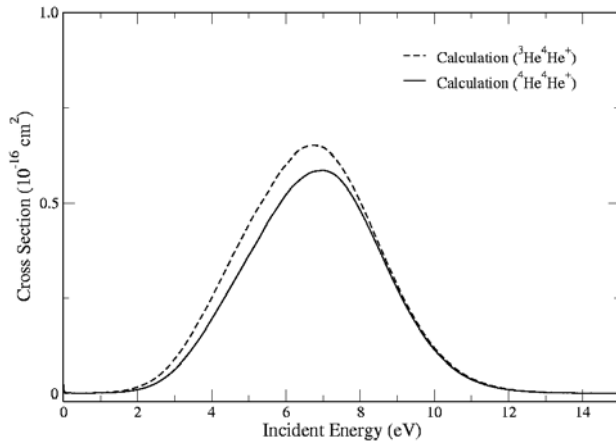


Fig. 2.7: The DR rate coefficient of ${}^3\text{He}^4\text{He}^+$ [RO05] and ${}^4\text{He}_2^+$ [OR06] as calculated by Royal and Orel using a time-dependent wave packet calculation with resonance parameters found with a complex Kohn variational method.

The shape and size of the peak agrees very well with the results of the ASTRID experiment (Fig. 2.6,[UDS⁺05]). Cross sections for the $v=1$ and 2 vibrational levels were also calculated, showing more and higher peaks at lower energies than the $v=0$ cross section.

The cross section for the homonuclear system ${}^4\text{He}_2^+$ was calculated later, too [OR06]. A comparison of the two resulting rate coefficients is shown in Fig. 2.7. The shape is almost the same, only the maximum is shifted to higher energies for ${}^4\text{He}_2^+$ to $E \approx 6.9$ eV and the peak height is about 10 % smaller than for ${}^3\text{He}^4\text{He}^+$.

2.4.3 Experimental goals

Because the DR rate coefficient of He_2^+ changes by orders of magnitude as the vibrational excitation increases, one should expect that for ${}^4\text{He}_2^+$ the fast recombining states disappear faster from the stored ion beam than the slow recombining states. Thus an evolution of the vibrational population with time is expected, resulting also in a time-dependence of the DR rate coefficient. Based on the rate coefficients predicted by Carata *et al.* [COS99] amounting to $\alpha_{DR}^{v=0} \approx 10^{-11} \text{cm}^3 \text{s}^{-1}$ at near zero electron energy and to a value 3–4 orders of magnitude larger for $\alpha_{DR}^{v=3}$, it might be possible to observe both effects in a storage ring experiment with long measurement times with a sufficiently strong electron beam (Sec. 3.3.1)². From the direct measurement of vibrational populations as function of time (Sec. 3.2) and a parallel measurement of the DR rate coefficient, the rate coefficients for individual vibrational levels can be extracted. In addition, the same data allows to search for SEC (Eq. 2.7).

² The reaction rate R for an ion with $\alpha_{DR} = 10^{-7} \text{cm}^3 \text{s}^{-1}$ at an electron density of $n_e = 10^7$ would be $R = \alpha \cdot n_e \cdot 1.5 \text{m} / 55.4 \text{m} = 0.027 \text{s}^{-1}$ at the TSR, so after 40 s only 1/e of the initial population would remain

With such a strong dependence of the DR rate coefficient of the initial vibrational level of the molecular ion, ⁴He₂⁺ is an ideal probe to investigate non-radiative excitation processes in storage ring experiments. Such processes are inelastic collisions with electrons (Eq. 2.7) and with residual gas (Eq. 2.11), which are studied in Secs. 4.4 and 4.5.

2.5 HD⁺, the indirect process and low energy rotational resonances

The H₂⁺ molecular ion is the benchmark molecule for many molecular physics applications. It is a system of only 3 particles and as such the simplest molecular ion, if one disregards exotic 'molecules' formed by leptons, such as the positronium ion. The homonuclear species H₂⁺ and D₂⁺ are a little simpler than the HD⁺ from the theoretical point of view, because of the additional symmetry due to the equal masses. But the heteronuclear HD⁺ has one immeasurable advantage in experiments: It has a permanent dipole moment and therefore is infrared active. By radiative interaction the internal excitation of a sample of HD⁺ molecules will obtain the temperature of the surrounding in a very short time: ~100 ms for the vibrations and ~5 s for rotations [AZF94]. At 300 K this corresponds to more than 99 % of the population in the vibrational ground state (v=0) and only a handful of rotational levels involved (≥ 95% in j=0–5). Comparisons between experiment and theory are strongly simplified by the restriction to a single vibrational state, with a degree of complexity still remaining regarding rotations.

2.5.1 Earlier experimental results on the low-energy DR of HD⁺

The dissociative recombination of HD⁺ was measured at several storage rings. A detailed comparison of measured high-resolution DR rate coefficients as function of the collision energy from ASTRID in Aarhus, CRYRING in Stockholm and TSR in Heidelberg showed very good agreement on the level of the electron beam temperature [ARD⁺03] – kT_{\perp} =22 meV, 2 meV and 4.5 meV, respectively. The measured cross sections are shown in Fig. 2.8.

The low-energy region was found to be rich of structures. Also, the absolute DR rate coefficient was measured and a value of $\alpha_{DR}(9.8 \text{ eV})=6.5(1.3)\cdot 10^{-9}\text{cm}^3\text{s}^{-1}$ was found in general agreement with each other. Another storage ring measurement of the energy dependent HD⁺ DR cross section was done at TARN II [TKK⁺95] with an electron beam with kT_{\perp} =4–7 meV. The cross section obtained in this experiment can be seen in Fig. 2.9.

In an earlier paper on the comparison of experiment at CRYRING and theory [SSS⁺95], it was found that the direct DR process (Eq. 2.2) can very well describe the observed cross section in the energy range of 5–12 eV, i. e. at the first broad structure observed in all shown cross sections (Figs. 2.8 and 2.9). In the calculations a broad band of Rydberg states to the first electronically

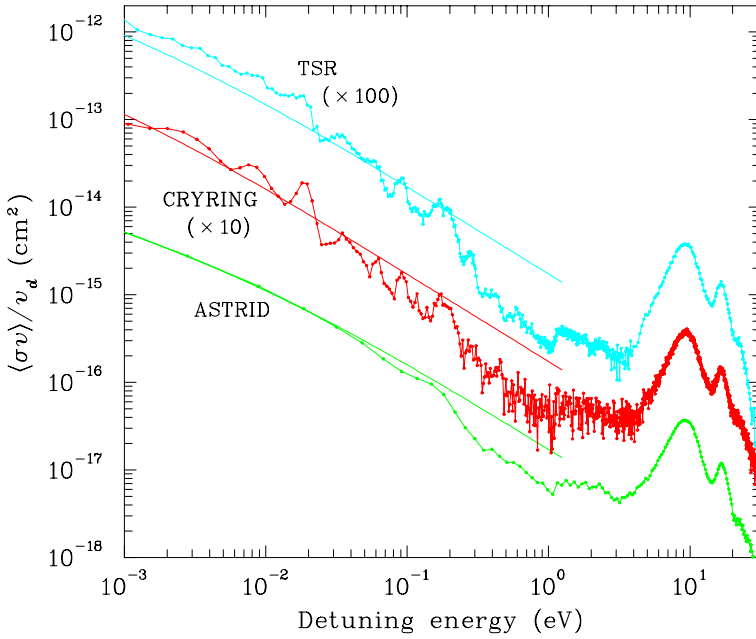


Fig. 2.8: Comparison of the measured absolute DR cross section of HD^+ from 3 different storage rings (green: ASTRID, red: CRYRING, light blue: TSR) taken from [ARD⁺03]. The cross sections from CRYRING and TSR were scaled by a factor of 10 or 100, respectively, for clarity. The smooth lines correspond to a model cross section $\sigma(E) = A/E$ folded with the electron temperature at ASTRID and fitted to the low energy part of the ASTRID data.

excited state of HD^+ was included. These states served as those doubly excited states that the initial capture happens into in the direct DR.

Also for low electron energies there is an appropriate curve crossing between the HD^+ electronic ground state and a neutral dissociative state between the $v=0$ and $v=1$ vibrational levels (Fig. 2.10) that could drive the direct DR process efficiently. But while the DR rate coefficient as a function of energy can be well explained by the direct process for HD^+ [SSS⁺95] at relatively high energies, the low energy region features a large number of resonances that need the indirect process to be explained.

One of the recent efforts from the theoretical sides was made by Takagi [Tak93] who originally treated the case of H_2^+ with Multichannel Quantum Defect Theory (MQDT) including rotational couplings. His approach was applied to the DR of HD^+ and published alongside with the experimental results from TARN II, showing good agreement [TKK⁺95]. In Fig. 2.9 the full line shows the calculated DR cross section for vibrational ground state ($v=0$) HD^+ at a rotational temperature of 800 K. A number of structures are assigned vibrational and principal quantum numbers v' and n_{Ryd} of the involved resonant Rydberg states in the indirect process.

Almost all structures that are assigned to a resonance are dips or local minima in the observed cross section. One could assume that dips due to resonances will only show up in the energy dependent rate coefficient, if they are at the same position for all initial rotational levels of HD^+ . They can also occur, if they arise from a single J -state that dominates the behaviour of the rotational-temperature-weighted cross section, either by being very strongly populated or by having a much higher cross section than other J -states in the energy region.

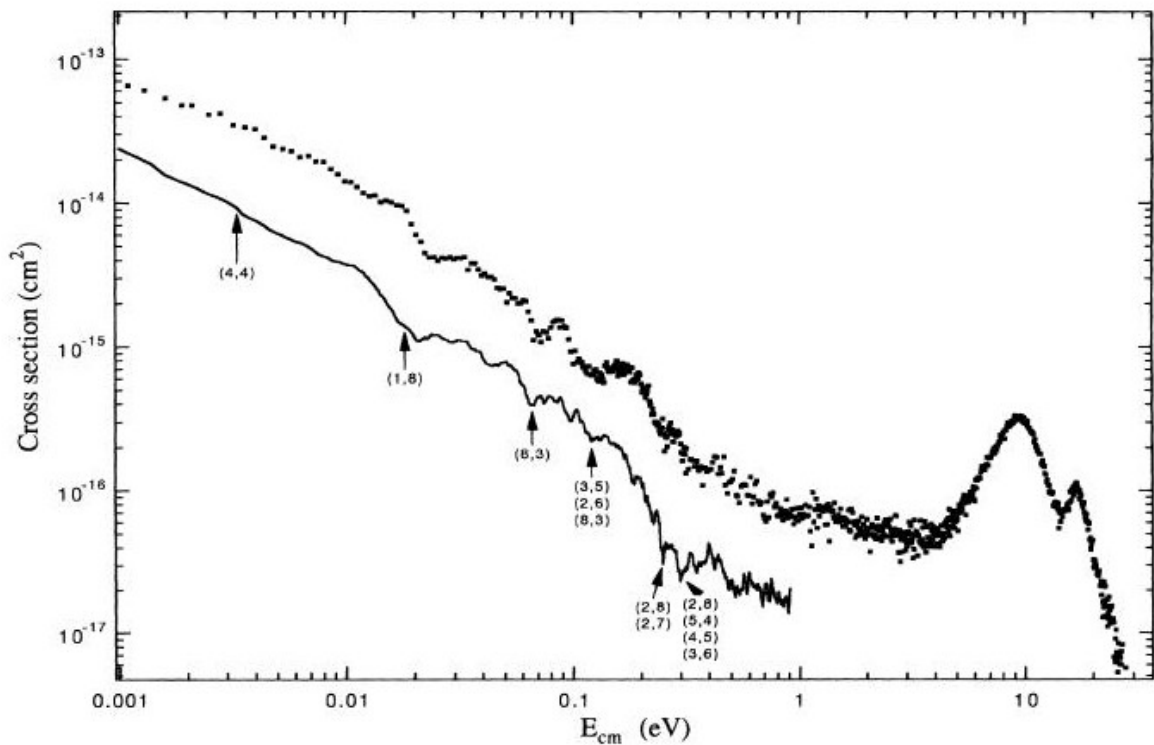


Fig. 2.9: Relative DR cross section of HD⁺ as function of energy in experiment at TARN II (dots) and theory by Takagi (line) [TKK⁺95]. The experimental cross section is arbitrarily scaled. The numbers in parentheses are supposed to give the (v' , n_{Ryd}) vibrational and Rydberg level of the intermediate state in the DR process. Δv and v' are the same since the initial vibrational level is the ground state $v=0$.

Single rotational states should not dominate the population of HD⁺ at the estimated rotational temperature of 800 K [TKK⁺95], the biggest contributions being around 15 %. If the J -dependent DR cross sections $\sigma_{DR,J}$ are of comparable size, only a 15 % effect should be expected. Thus, either single J -states may have cross sections much higher than all others in certain energy ranges, or several J -states with resonances at similar energies show a common cross section behaviour. This question will be addressed experimentally in Ch. 5. Unfortunately the involved initial rotational states at the resonances were not cited in addition to the vibrational and principal quantum number.

2.5.2 Other electron collisions studied with HD⁺

The resonant ion-pair formation $\text{HD}^+ + e^- \longrightarrow \text{H}^+ + \text{D}^-$ was treated theoretically with a time-dependent wave-packet method in a recent work [LO01] in an attempt to model experimental results obtained at the CRYRING storage ring [LDZ⁺00], yielding reasonable agreement. In the experiment, a lower threshold of $E=1.92$ eV for the collision energy was found for the occurrence

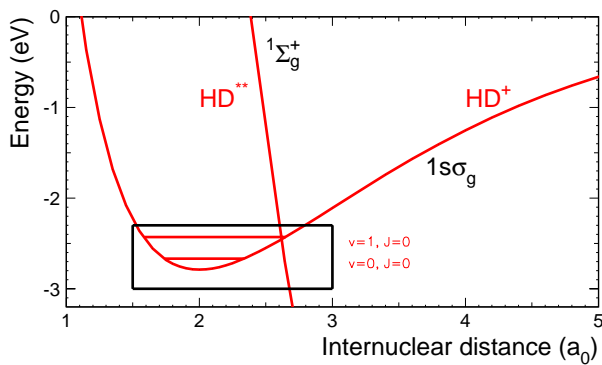


Fig. 2.10: The bound electronic ground state of HD^+ [ES99] and the neutral dissociative curve [Gub83] responsible for the direct process at low collision energies. The black box shows the range that is enlarged in Fig. 2.11.

of the ion-pair formation and rate coefficient of $\alpha(2eV) \approx 2.5 \cdot 10^{-11} \text{cm}^3 \text{s}^{-1}$ was observed and later also the channel leading to $H^- + D^+$ was measured with a similar result [NDH⁺02]. Recently ion-pair formation was also observed at the TSR making use of the negative and positive ion detectors situated downstream [Hofed].

Also super-elastic collisions have been studied, but mainly for the homonuclear species H_2^+ and D_2^+ , because it is hardly observable in HD^+ because of the short lifetimes of the vibrationally excited levels. Vibrational SEC was observed in experiments with H_2^+ at TARN II [TTK⁺99] and at the TSR an absolute rate coefficient of $\alpha_{SEC} = 1-4 \cdot 10^{-6} \text{cm}^3 \text{s}^{-1}$ was shown to be in agreement with the measured data [KAB⁺00]. Vibrational cooling of D_2^+ by the interaction with electrons was observed at CRYRING [LCD⁺94] in the DR rate coefficient as function of time from changes in the vibrational peak around $E_d = 10 \text{eV}$, but the effect was attributed to preferential depletion of highly excited states with higher DR rate coefficients rather than to SEC. In later measurements at the TSR the vibrational cooling was observed with DR fragment imaging at $E_d = 0 \text{eV}$ and the effect was explained by the presence of SEC [Kro02] with an absolute rate coefficient of $\alpha_{SEC} \sim 1 \cdot 10^{-7} \text{cm}^3 \text{s}^{-1}$, depending on the initial vibrational level.

A theoretical treatment of the vibrational deexcitation of H_2^+ based on the MQDT formalism [NMF⁺03] yielded a SEC rate coefficient which is about one order of magnitude lower than the experimental results. Previous theoretical models [ST93, NTN87] showed similar rate coefficients that are lower than the experimental values.

2.5.3 A simple model to predict the positions of resonances

Applying the model idea of the indirect DR process that was used in Sec. 2.2.1 one can try to predict electron energies at which low-energy resonances in the DR of HD^+ due to the indirect process can be expected. Below each ionic curve there is a series of molecular Rydberg states converging towards the ion curve. Such a Rydberg state can be interpreted as consisting of a weakly bound electron with a principal quantum number n_{Ryd} and angular momentum l_{Ryd} and

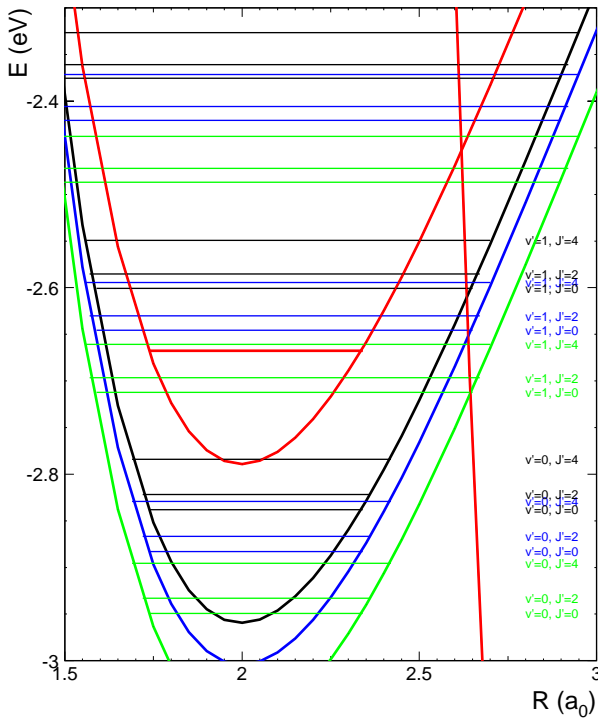
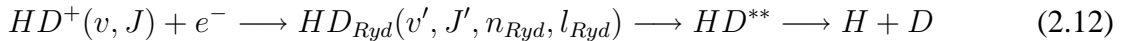


Fig. 2.11: A selection of potential energy curves with some rovibrational levels involved in the low energy DR of HD⁺ in the rovibrational ground state. Red: The bound electronic ground state of HD⁺ [ES99] with the rovibrational ground state $v=0, J=0$ and the neutral dissociative curve [Gub83] responsible for the direct process at low collision energies. Green: The molecular Rydberg state $n_{Ryd}=7$ of HD. Blue: The molecular Rydberg state $n_{Ryd}=8$ of HD. Black: The molecular Rydberg state $n_{Ryd}=9$ of HD. To each of the Rydberg states the $v'=0, 1$ and 2 vibrational levels with $J'=0, 2$ and 4 rotational quanta are drawn. More Rydberg states exist and also play a role. The Rydberg states are obtained by shifting the ion curve to lower energies by a distance given in [TT72]

an ionic core comparable to the molecular ion state the series converges to.

This also applies to the HD⁺ ground state (see Fig. 2.10), where the vibrationally and rotationally excited levels of the Rydberg states below this core are labeled by its corresponding quantum numbers v' and J' . Electron capture can happen into these states and then lead to dissociation in the indirect DR process



Some of the rovibrational levels in the Rydberg states with $n_{Ryd}=7, 8, 9$ are given in Fig. 2.11 in green, blue and black, respectively. They are shown for the molecular ion ground state $v=0, J=0$ that is given in red, along with the dissociative neutral PES. The range in internuclear distance and energy corresponds to that indicated by the black box in Fig. 2.10. For HD⁺, the most important partial wave is $l_{Ryd}=2$, so that $|\Delta J| \leq 4$ (see Sec. 2.2.1) and ΔJ even because of the symmetry [SSC⁺97].

Because of the large number of Rydberg levels this is clearly a selection only. However, the choice of states in this figure indicates that candidates leading to low-energy resonances with the allowed J' values and low v' are in fact the Rydberg levels $n_{Ryd}=7$ and 8. Since, to our knowledge, complete data on the ionization energies of all rovibrational levels in the HD Rydberg states is not available, the Rydberg state potential curves plotted here and used throughout are not measured, and calculated by simply shifting the ionic curve. For this purpose, the $1s\sigma_g$

curve of the ionic ground state calculated by Esry [ES99] was shifted downwards by the ionization energies of the Rydberg levels found with absorption spectroscopy of VUV light by Takezawa [TT72] to represent the Rydberg states PES. The rovibrational energies within the electronic states are also those of the molecular ion and are taken from [HYP74]. Using these data is a big simplification, especially for the Rydberg states with low principal quantum number, for which the shape of the potential will be significantly different. As the principal quantum number increases, the agreement, however, can be expected to improve.

Another problem is, that the Rydberg levels and their energies provided by Takezawa [TT72] refer to p-levels, while the important Rydberg levels in the DR are the s- and d-levels, because DR happens with free electrons in the s- and d-wave for HD^+ (see above). Spectroscopic data do not seem to be available for these symmetries. This could introduce a general shift on the order of 10 meV for higher Rydberg levels, because of the different quantum defects, but should be sufficient for the purpose of demonstration.

Even with the inclusion of only one rovibrational initial level, $J=0$, out of the six that are strongly populated (Sec. 2.5 and Fig. 5.9) and just three Rydberg states from an infinite number, we find nine collision energies in the range of 0–100 meV as possible resonance positions in Fig. 2.10. Including more Rydberg states and initial levels in this figure probably will not further the understanding of the mechanism and make results difficult to interpret. A different representation is likely to be more helpful.

In Fig. 2.12 the energy difference between the initial rovibrational level of the molecular ion in Fig. 2.10 and a level in the Rydberg states with a $\Delta J=0, 2$ or 4 is plotted. Vertical, dashed lines mark these energies. The position along the horizontal axis is the energy difference or the collision energy necessary to reach that level. It is assumed, that we have the $v=0, J=0$ rovibrational ground state as initial ion state, like in Fig. 2.10. The vertical lines end at a height corresponding to the levels in the Rydberg states they are associated to. Each height stands for a different pair of Δv and ΔJ compared to the initial state. The colours of the vertical lines shall indicate, which principal quantum number the Rydberg state has, e. g. the light blue represents Rydberg states with $n_{\text{Ryd}}=10-48$. The fact that the list of included Rydberg states stops at $n_{\text{Ryd}}=48$, is the reason for the 'empty' range to the Rydberg limits marked in red. There are more Rydberg series limits than the two visible ones, but not in the plotted range. A helpful systematic is given by the distances between the different rotational resonance positions within one Rydberg state n_{Ryd} , that are repeated in the other Rydberg states, too, e. g. the dark blue ($n_{\text{Ryd}}=8$) and the black lines ($n_{\text{Ryd}}=9$) of the $\Delta v=1$ class. A series with $\Delta v=0, \Delta J=0$ is forbidden, because the Rydberg state PES lie below the molecular ion state.

Considering also the other initial molecular ion states. Figs. 2.13 and 2.14 show results for

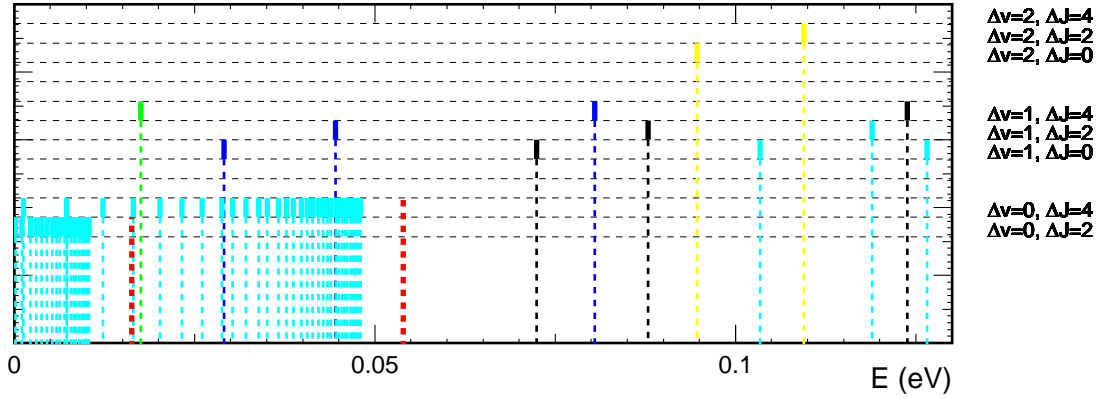


Fig. 2.12: The energies of possible rotational Rydberg resonances for HD⁺ with $v=0$, $J=0$ in the range of 0–130 meV collision energy. Included are all lines with $\Delta v=0,1,2$ for Rydberg levels $n_{\text{Ryd}}=2\text{--}48$. These positions are marked with vertical lines ending at a height depending on the values of Δv and ΔJ between initial state and Rydberg state. The horizontal dashed lines are meant to guide the eye along resonance candidate positions with the same Δv and ΔJ . The colour of the vertical lines is to distinguish between different principal quantum numbers n_{Ryd} of the neutral Rydberg state. Yellow: for $n_{\text{Ryd}}=2\text{--}6$. Green: for $n_{\text{Ryd}}=7$. Blue: for $n_{\text{Ryd}}=8$. Black: for $n_{\text{Ryd}}=9$. Light blue: $n_{\text{Ryd}}=10\text{--}48$. The dashed red lines indicate the positions of the limits of a Rydberg series with $\Delta v=0$.

$v=0$ and $J=0\text{--}6$. Very different resonance patterns seem to result from the different initial rovibrational states. However, one can identify some positions that occur in all figures at the same energy. For example, a dark blue line due to the $n_{\text{Ryd}}=8$ Rydberg state with a $\Delta v=1$, $\Delta J=0$ occurs for each of the initial states in the range of $E=25\text{--}30$ meV, and a black one corresponding to $n_{\text{Ryd}}=9$, $\Delta v=1$, $\Delta J=0$ shows up at $E=67\text{--}72$ meV in each of the figures. Both lines feature $\Delta J=0$ with energy differences introduced by a small v -dependence of the rotational constant B_v . This is due to the non-rigid character of the molecule, leading to different rotational energies $E_{\text{rot}} = B_v \cdot J \cdot (J + 1)$ with $B_0 > B_1$ or to a centrifugal distortion constant D_v correcting the energy by $\delta E_{\text{rot}} = -D_v \cdot J^2 \cdot (J + 1)^2$. Both effects yield lower energies for higher rotational states.

The fact that the resonance positions are nearly the same for all initial rotational states is important, as it can produce a structure in the energy rate coefficients occurring for each of these initial states at the same energy. The complete population of HD⁺ could contribute to this structure, which then should show up quite strongly in the experimental data. Fig. 2.15(a) shows only those states with the $\Delta v=1$ and $\Delta J=0$ in the energy range $E=0\text{--}130$ meV. There are four such Rydberg states, $n_{\text{Ryd}}=8\text{--}11$. For comparison, the HD⁺ DR rate coefficient scaled with \sqrt{E} is also plotted, as obtained earlier at CRYRING [ARD⁺03] (see Fig. 2.8). Structures in the exper-

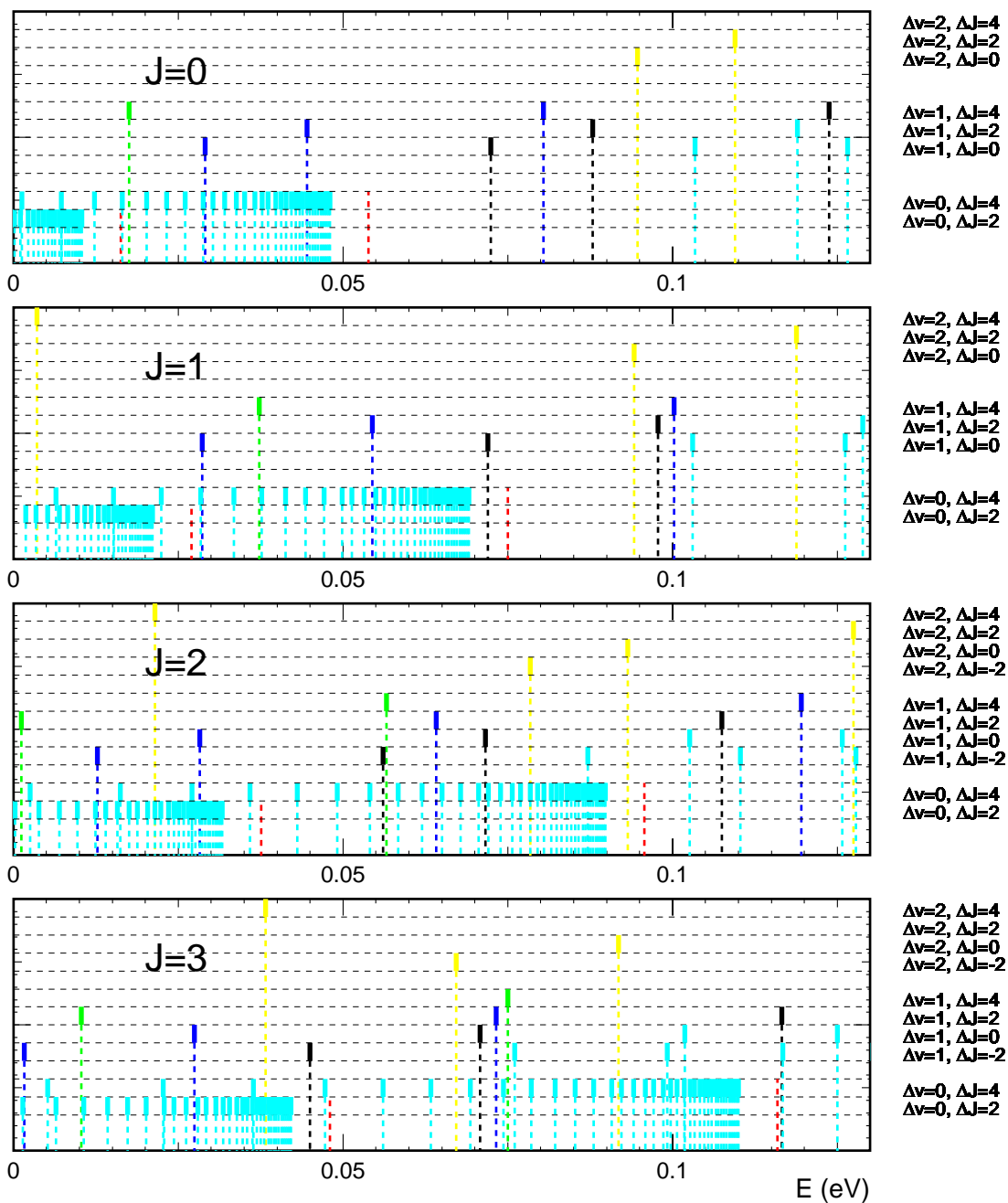


Fig. 2.13: The energies of possible rotational Rydberg resonances for HD^+ with $v=0, J=0$ in the range of 0–130 meV collision energy for HD^+ with $v=0, J=0$, with $v=0, J=1$, with $v=0, J=2$ and with $v=0, J=3$ for principal quantum numbers $n_{Ryd}=2-48$. For details see caption of Fig. 2.12

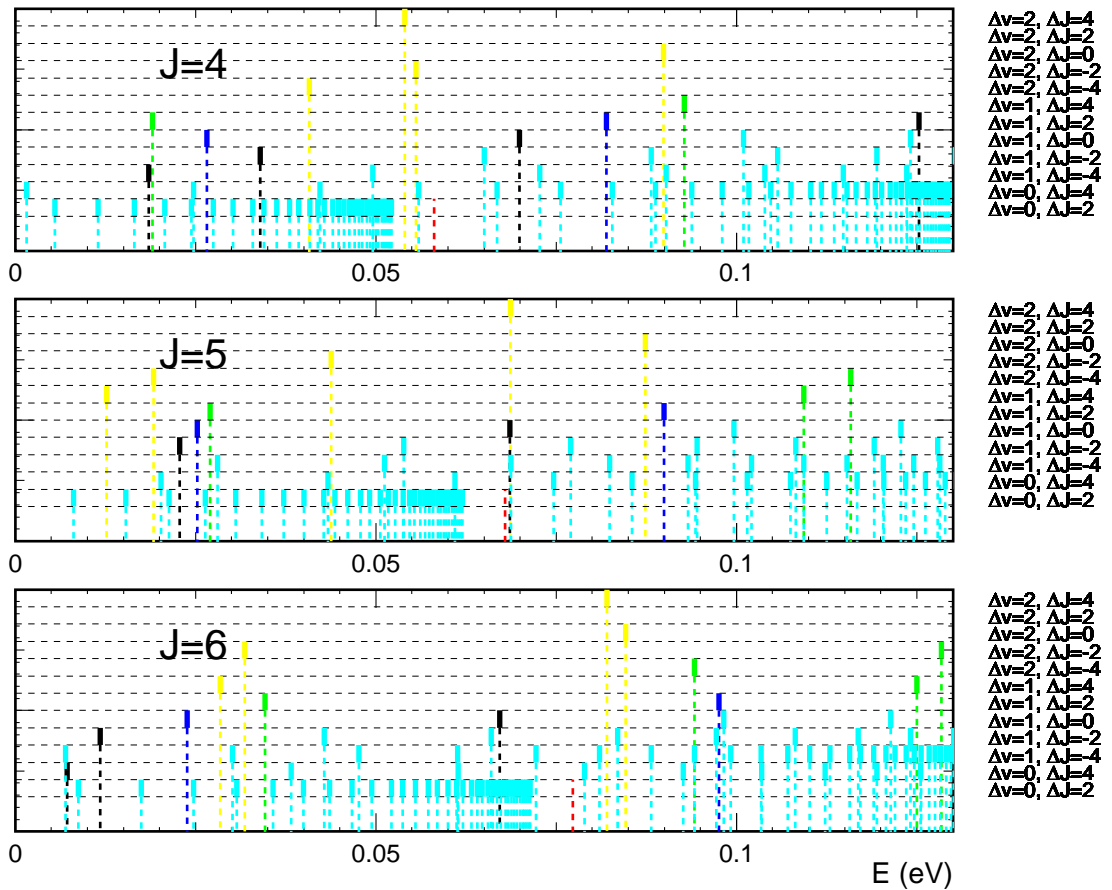


Fig. 2.14: The energies of possible rotational Rydberg resonances for HD⁺ with $v=0$, $J=0$ in the range of 0–130 meV collision energy for HD⁺ with $v=0$, $J=4$, with $v=0$, $J=5$ and with $v=0$, $J=6$ for principal quantum numbers $n_{Ryd}=2-48$. For details see caption of Fig. 2.12

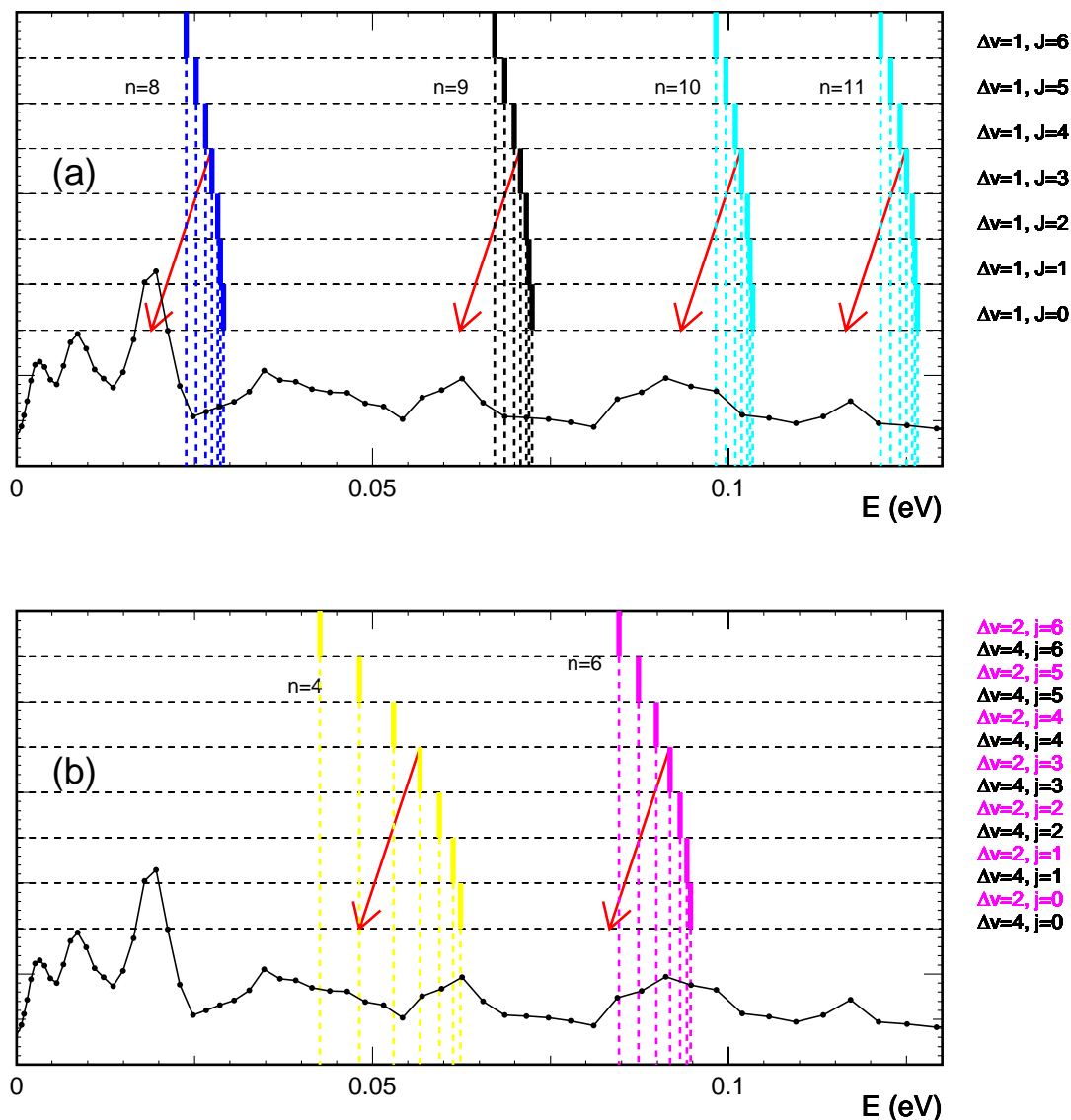


Fig. 2.15: Energies of selected possible low energy rotational Rydberg resonances in HD^+ compared to the scaled DR rate coefficient ($\alpha \cdot \sqrt{E}$) of HD^+ function of energy from CRYRING [ARD⁺03]. The red arrows are of equal length and direction. They indicate a shift by 8.5 meV, starting at the position of the $J=3$ levels. (a) Only model resonances with $\Delta v=1$ and $\Delta J=0$ are shown for initial HD^+ states $J=0-6$. (b) Only model resonances with $\Delta v=2$ and $\Delta J=0$ (purple) or $\Delta v=4$ and $\Delta J=0$ (yellow) are shown for initial HD^+ states $J=0-6$. There is only one Rydberg state contributing in this range to each of these Δv classes.

imental data do appear near the model resonance positions with a similar shift of approximately 8.5 meV to lower energies for all cases. This shift is well compatible with the uncertainty in the quantum defects (see above).

Also the $\Delta v=2$, $n_{Ryd}=6$, $\Delta J=0$ resonance group can be identified and possibly associated to a structure in the data after a shift of ~ 8.5 meV (Fig. 2.15(b)). The situation is less clear for the lower level $\Delta v=4$, $n_{Ryd}=4$. However, the l -dependence of the quantum defects should have much larger effects for this low level than for the high Rydberg levels considered earlier. Thus $\Delta J=0$ resonances with $\Delta v=1$ and $\Delta v=2$ seem to offer a partial explanation for the assignment of the DR spectrum.

In the resonance assignment by Takagi and Tanabe [TKK⁺95] in Fig. 2.9 only three of the six resonances discussed here are included, namely $n_{Ryd}=8$, $\Delta v=1$; $n_{Ryd}=6$, $\Delta v=2$; and $n_{Ryd}=4$, $\Delta v=4$ ($v=\Delta v$ for this case). The theoretical $n_{Ryd}=8$, $\Delta v=1$ resonance is placed at about 18 meV in good agreement with our model after the shift of 8.5 meV. Other resonance assignments in this work do not appear final. Moreover, the rotational assignments are not considered.

Hence, the fact that there is no complete labeling of the observable resonances in the experimental data on the DR of the simplest molecular ion calls for additional efforts to understand the processes involved. This could be a first step towards the capability to calculate cross sections for molecular ion dissociative recombination that agree with the experimental data on a level comparable to what is achieved in dielectronic recombination in atoms, where the same number of particles or even more are involved. Then it could also be possible to extract the rotational temperature of a stored ion sample from the DR rate coefficient as function of energy.

3. Experimental method

The experiments presented in this work were performed at the Test Storage Ring (TSR) [HBB⁺89] at the Max-Planck-Institut für Kernphysik in Heidelberg. An overview of the experimental setup from the ion production, acceleration and storage (Sec. 3.1) over electron cooling and the well known experimental devices to the recently installed electron target (Sec. 3.4.1) and associated detectors is given in the following sections along with a description of the experimental methods. The experiments with fast (MeV) molecular beams allow to observe reactions leading to break up with low (eV) energy releases with 4π solid angle on small (cm) detectors in large (m) distance.

3.1 Ion production, acceleration and storage

At the TSR several ion beam accelerators are available to provide a large variety of molecular and atomic ion beams of variable energies. A tandem Van-de-Graaff accelerator can be used in the production of heavy atomic ion beams like Fe^{13+} [SSM⁺06] and of molecular ions like CH_2^+ [LBK⁺04], but it was not used in the experiments that are subject of this work. Light molecular ions with a total mass of less than 9 atomic mass units (amu) like the HD^+ (Sec. 5) and He_2^+ (Sec. 4) are accelerated in a radio frequency quadrupole (RFQ) structure [Sch99] that can yield exit energies of 500 and 250 keV/amu depending on whether the full structure is used or only half of it. Eight seven-gap resonator structures can increase the ion energy further to up to 1.7 MeV/amu. Ions from both accelerators pass through an RF post accelerator unit that may increase the beam energy further, a feature not used for the experiments treated in this work. The beam energies for the HD^+ ions were 1.4 MeV and 5.3 MeV (~ 0.5 MeV/amu and 1.7 MeV/amu, respectively). For He_2^+ the beam energies were between ~ 0.5 MeV/amu and 1.0 MeV/amu.

The molecular ions for storage ring experiments can be produced in a wide variety of ion sources. HD^+ is a standard ion beam and for the present experiments it was produced in a CHORDIS (Cold HOt Reflex Discharge Ion Source) [KNT89] from which molecular ions can be extracted at high currents of up to $52\mu\text{A}$ [Rep02]. The production of He_2^+ was more difficult.

3 Experimental method

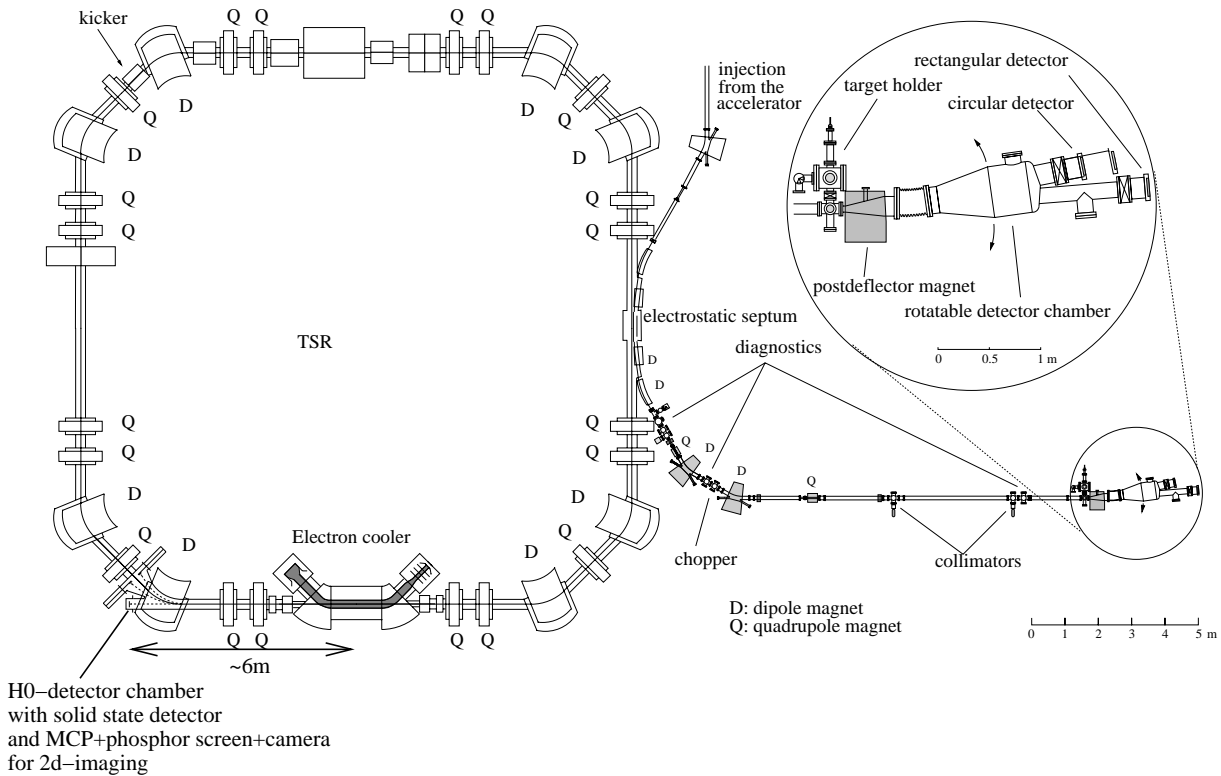


Fig. 3.1: TSR and CEI-experiment setup as it was used in the He_2^+ experiments using the electron cooler alone.

Different source types were tested, e. g. also the CHORDIS. A standard duoplasmatron ion source [Gre74] gave the best results and different geometries, pressures, and operating voltages and currents for the arc and magnet of the source were tested before a satisfying and stable molecular ion yield was achieved. Currents of 1.0-1.4 μA of $^4\text{He}_2^+$ could be extracted, when the source was driven with pure ^4He . Arc currents of 100–200 mA, arc voltages of 80–200 V and a source magnet current of approximately 1 A were typical settings. For an input of a mixture of ^3He and ^4He a maximum current of 300-500 nA of $^3\text{He}^4\text{He}^+$ was delivered, for total pressures of 0.4-1.1 mbar in the filament chamber and arc currents varying in the range of 0.08-0.33 A [PBA⁺05]¹. These settings for the duoplasmatron source were applied in the He_2^+ experiments.

After acceleration the molecular ion beam is transferred to the TSR and the ions enter at an electrostatic septum. Fig. 3.1 gives a schematic illustration of the storage ring. The 55.4 m circumference ring has an octagonal shape with a dipole magnet in each corner and 20 quadrupole magnets to steer and focus the beam. An electron cooler (Sec. 3.3.1) can reduce the phase space

¹ The article accidentally quotes mA instead of A

spread of the ions in the beam. Ion getter pumps and NEG pumps ensure the necessary vacuum quality of residual gas pressures in the order of 10^{-11} mbar. Typically, molecular ion beams can be stored for 100 s. This allows the preparation of ions in well defined states and the observation of time dependent processes, i. e. effects due to changes in the internal excitation of the stored molecules.

3.2 Vibrational excitation diagnostics

One form of the internal excitation of molecular ions that can be changed – usually reduced – during long beam storage times is vibrations. The Coulomb Explosion Imaging (CEI) technique is a powerful tool to monitor this [WAG⁺98]. It is used to directly examine the structure of small molecular ions. As opposed to spectroscopic methods, where the measurement of the structure is indirect via energy spacings between states and intensities of transitions, with CEI the structure can be observed almost directly. This diagnostic tool was used to determine the vibrational states populations of He_2^+ (Sec. 4.1) and we will give an introduction into the method (Sec. 3.2.1), before the experimental setup is discussed (Sec. 3.2.2).

3.2.1 Principles of foil-induced Coulomb Explosion Imaging

A molecule formed by two or more nuclei is destroyed by the instantaneous removal or stripping of the binding – and preferably all – electrons. Then the Coulomb forces, due to the positive charges of the nuclei, drive the explosion of the molecule. If the change from bound molecule to bare nuclei happens very fast compared to the nuclear motion, the stripping is a projection of the bound nuclear wave function onto the dissociative Coulomb potential. The final or asymptotic velocities of the outgoing fragments then reflect the initial geometry in the molecule.

The fast removal can be performed with an intense laser field or by shooting fast molecules through ultra thin foils. The latter procedure is called *foil-induced CEI*. Molecules with an energy of several hundred keV per nucleon are directed onto a target foil where the binding electrons are stripped within the first few atomic layers on a time scale of less than 10^{-16} s [ZGKV92], faster than the typical vibrational (10^{-14} s) and rotational (10^{-12} s) times. Most of the acceleration in the explosion happens unperturbed, after the fragments passed the foil until the final velocities are reached. A few meters of flight path allow the fragments to reach macroscopic distances that can be measured with a position and time sensitive detection system. From these distances the relative velocities can be extracted.

The asymptotic fragment velocities of one molecule are the image of one possible configuration of the molecule. In a typical CEI experiment, fragments of several 10^5 molecules are observed,

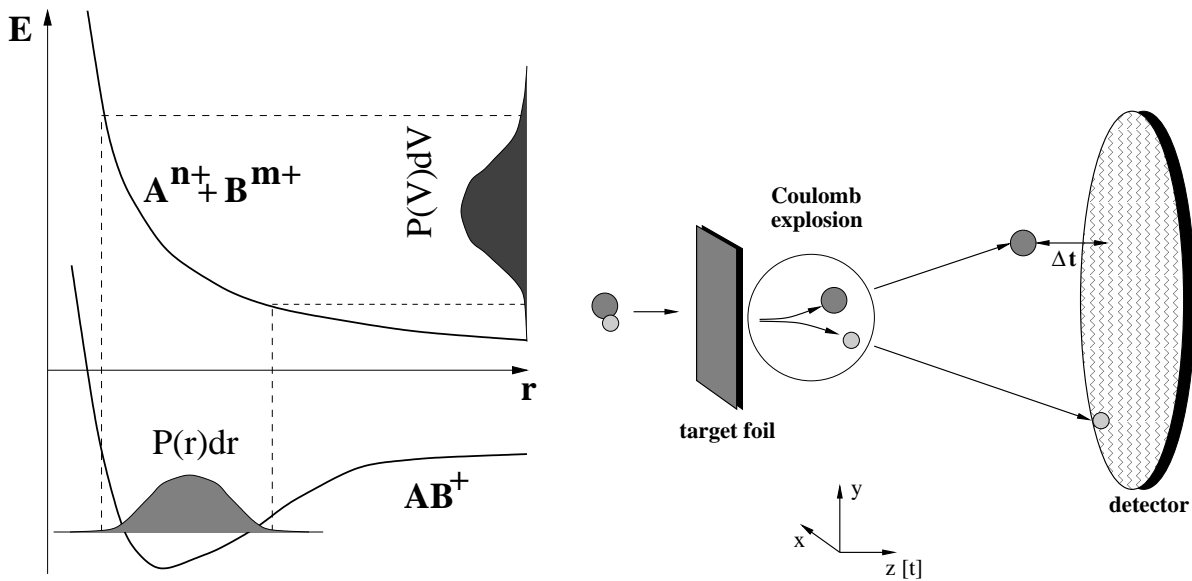


Fig. 3.2: Left: For a diatomic molecule, the internuclear distance r is the only inner coordinate in the bound molecule. With ideal CEI, the probability density $P(r)dr$ of the possible internuclear distances is projected onto a probability density of relative velocities $P(V)dV$. The projection is a transformation given by the Coulomb potential curve. Right: The principle of foil-induced CEI: High velocity (a few percent of the speed of light) molecular ions are directed onto a thin target foil, where the binding electrons are stripped in a fast process. The produced ions are driven apart by the Coulomb forces and are directed onto a time and position sensitive detector.

in order to obtain the image of the complete probability distribution of the initial state wave function of the molecule prior to the stripping.

Fig. 3.2 illustrates the idea of the projection and the experimental procedure for a diatomic molecule. In that case, there is only one internal or R-space coordinate, the internuclear distance. This corresponds to the magnitude of the relative velocity vector of the two nuclei after the break up in the V-space.

Since there are interactions between the nuclei and target atoms e. g. leading to random small angle scattering and polarization effects of the target, the internal structure cannot be derived from the measured velocities directly. Instead a forward simulation of the experiment is used to model the Coulomb explosion, target effects and detection system. With this a large sample of virtual molecules with a given distribution in R-space is transformed to a V-space density that is compared to the experimental data. Deviations of the simulated V-space density from the experimental one can be reduced by adjusting the input R-space density following an algorithm explained in [Wes99] and then redoing the simulation. This is repeated until the agreement between experiment and simulation is satisfactory. The finally used input R-space density is

assumed to describe the structure of the experimentally observed sample. The R-space density $P(r)$ that is found in this way can be described as a linear combination of the R-space densities $P_v(r)$ of the individual vibrational states of the molecular ion:

$$P(r) = \sum_v p_v P_v(r) \text{ with } \sum_v p_v = 1 \quad (3.1)$$

where p_v is the relative population of a given level v in the sample, thus revealing the vibrational excitation distribution.

3.2.2 The CEI Setup

The Coulomb Explosion Imaging (CEI) setup is linked to the storage ring TSR. It has been described in great detail in several previous publications and theses [WAG⁺98, Wes99]. The combination of storage ring and CEI setup offers the opportunity to study a sample of molecules continuously over a long period of time. As the molecular ions are generally created in hot environments, the ions are initially rovibrationally highly excited. The hot sample of molecular ions relax via spontaneous emission, if they are infrared active or via SEC (Eq. 2.7), if electron cooling is applied. Typical radiative lifetimes of vibrational states in such molecules are well below 1 s, so that it is possible to study the thermalization of the sample within the ion beam storage time. In many cases this is equivalent to reaching the vibrational ground state.

Since the CEI technique allows to test the internal structure of a molecular ion, one can monitor the changes of the internal structure in the ions of the sample as a function of time spent in the storage ring. The internal structure mainly reflects the vibrational excitation and possible changes in the configuration (like in DCO⁺ [Wes99]) in the case of the CEI setup at the TSR.

The CEI-beamline is connected to the TSR at the septum (Fig. 3.1), where the ions are transferred using slow extraction with a relatively low ion current [ABG⁺96, WAG⁺98]. An electrostatic chopper in the beamline ensures that the extracted beam is interrupted, whenever a particle hits the detector since the detection system of the CEI-experiment is designed for a single event processing, i. e., only the fragments of one molecule can be read out properly at a time.

The ion beam is focused by further magnetic beam optics and collimated using two sets of collimators 3 m apart that can reduce the beam divergence to 0.17 mrad and its diameter to 0.5 mm. Two chambers with target foils exist, one at 5 m, the other one at 3 m from the detectors. In these, diamond-like carbon foils (DLC) [LKS⁺00] of about 2 mm diameter are mounted on retractable grid holders. The foil thickness ranges from 0.7 to 1.5 $\mu\text{g cm}^{-2}$ or 35 to 75 Å. The molecular beam passes through a specific one of them, initiating the explosion.

Further downstream a post deflector magnet separates the fragments according to their mass-to-

3 Experimental method

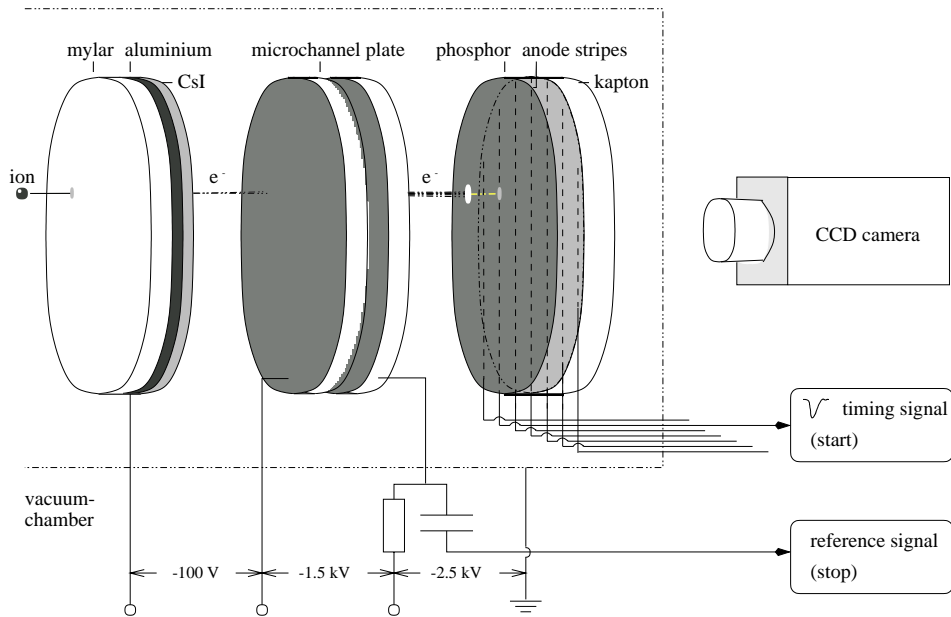


Fig. 3.3: Schematic illustration of the 3d-detector used in the CEI-experiments. The setup is explained in the text.

charge ratio. Two 3d-detectors are mounted in a detector chamber, with an angular separation of 120 mrad, measured from the post deflector. The whole chamber is rotatable about an axis at the magnet which allows – together with adjusting the strength of the deflecting field – to measure different fragment species on the two detectors simultaneously.

One of the detectors is circular with a diameter of 120 mm. The other one has rectangular shape being 93 mm wide and 75 mm high. Both detectors are similar in their design. Fig. 3.3 gives a schematic illustration of the structure of the circular detector. The incoming ion hits a mylar foil coated with CsI and Al working as an ion-electron conversion foil that creates about 10 to 100 electrons per hit. The efficiency of the following microchannel plate (MCP) is increased to almost 100 % in this way. The electron cloud from the MCP produces a light spot on a phosphor screen which is imaged by a 25 Hz CCD camera. This yields the impact position of the fragment with a resolution of up to 0.1 mm.

Timing information is generated by anode stripes behind the phosphor layer. There are 93 anode stripes at the rectangular detector and 64 at the circular one. They allow the detection of several particles on one detector, as long as they do not use the same anode stripes in the generation of timing information. Typical time resolution is in the order of 100 ps. The time and position information for each fragment of a single event are read out by a VME computer and stored together for further analysis.

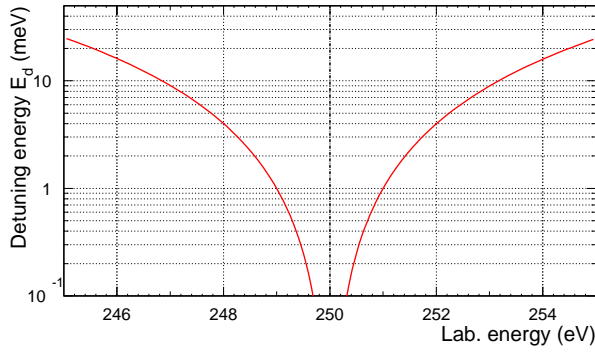


Fig. 3.4: An example for the detuning energy E_d (red line) as a function of the electron energy E_e in the laboratory frame. It is calculated for a velocity matching energy of 250 eV, which is indicated by the dashed line.

3.3 Standard collision experiments at the TSR

The standard experiments for electron-molecular ion collisions at the TSR use the electron cooler as phase space cooling device and as target that provides electrons for the collisions with the stored molecular ions.

3.3.1 Ion beam preparation and temperature of a merged electron beam

Apart from long storage times and 4π detection efficiency on a small solid angle in the laboratory frame, another advantage of a fast beam experiment is that very low relative energies in collision experiments can be realized. This is done by overlapping the ion beam with a co-propagating single-pass electron beam. The relative energy or detuning energy E_d between ions of mass m_i and energy E_i in the laboratory frame and electrons of energy E_e and mass m_e is given in non-relativistic approximation by

$$E_d = \frac{\mu}{m_e} \left(\sqrt{E_e} - \sqrt{\frac{m_e}{m_i} E_i} \right)^2 \quad (3.2)$$

where μ is the reduced mass of the electron-ion system. Fig. 3.4 illustrates the benefits of working with a fast beam when it comes to providing small relative energies. If the electron velocity matches the ion velocity at $E_e=250$ eV, i. e. if $E_d=0$ eV, a change of 1 eV in the lab corresponds to a detuning energy of $E_d=1$ meV in the center-of-mass system. In addition, the electron longitudinal temperature T_{\parallel} is reduced dramatically by the acceleration to high energies E_e . If the electrons are produced at a temperature T_C , the resulting T_{\parallel} is given by the relation:

$$k_B T_{\parallel} = \frac{(k_B T_C)^2}{2E_e} \quad (3.3)$$

if only kinematic effects are taken into account [Spr04], where $k_B=8.62 \cdot 10^{-5} \text{eVK}^{-1}$ is Boltzmann's constant.

In the TSR, the electron cooler is situated in one of the long straight sections (Fig. 3.1) and provides such an electron beam produced by a thermal cathode with $T_C=1300$ K. The longitudinal electron beam temperature at $E_e=250$ eV then can be as low as $kT_{\parallel}\approx 25$ μ eV according to Eq. 3.3. The transverse electron temperature T_{\perp} is cooled by adiabatic expansion in a decreasing magnetic field allowing to reach values of $kT_{\perp}\approx 10$ meV at densities of $n_e\sim 1\cdot 10^7$ cm^{-3} . The acceleration voltage for the electrons is variable and defines E_e and thus E_d . The electrons are bent into and out of the ion beam with toroid magnetic fields providing a section of parallel overlap with the ion beam of 1.5 m. The electron cooler is described in detail in [PSG⁺96].

At cooling energy, i. e. at $E_d=0$ eV, the single-pass electrons absorb kinetic energy from the ions present in the co-moving frame of the ion beam by elastic collisions. This absorbed energy reduces the ion momentum spread. By this phase space cooling the ion beam diameter can be reduced to 1 mm and the momentum spread $\frac{\Delta p}{p}$ to 10^{-4} .

3.3.2 Detectors at the TSR electron cooler

The electron cooler can also serve as a target for molecular ion-electron reactions. Neutral fragments emerging from reactions in the electron cooler exit the ring at the next downstream dipole magnet. About 6 m from the center of the cooler overlap region in a dedicated vacuum chamber are situated an energy sensitive surface barrier detector and behind it a microchannel plate (MCP) with a phosphor screen.

The surface barrier detector measures 7×4 cm^2 and can be moved along the vertical axis with a linear feed-through to completely retract it from the neutral fragment beam. It has a 100 % detection efficiency for MeV particles and can be used to determine absolute count rates. It is segmented into 7 vertical stripes which in principle could be read out individually, but this feature is not used.

Fragments from one dissociation event usually arrive within a few ns. The particles are stopped completely in the detector and create a signal that is approximately proportional to the total energy of the arriving neutral particles hitting within $\approx 1\mu\text{s}$ which limits useful measurement rates to the order of 10^4 Hz. A typical spectrum for a ${}^4\text{He}_2^+$ DR measurement is shown in Fig. 3.5. Three sharp peaks can be identified. Peak 1 with the lowest energy is caused by a single He-atom hitting the detector. The highest energy peak (peak 2) stems from both He-atoms hitting the detector. The smallest peak (peak 3) is due to 2 He-atoms hitting the detector, but one of them hitting a known area with less signal strength between two adjacent stripes. With this detector relative rate measurements as function of time and detuning energy are made. It was used in most of the DR measurements of He_2^+ presented in this work.

For 2d-imaging experiments a microchannel plate (MCP) in combination with a phosphor

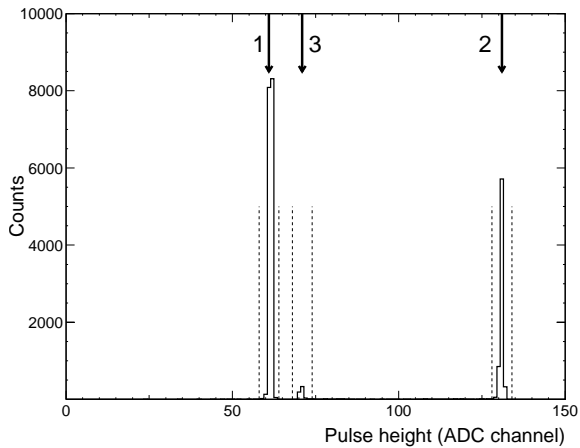


Fig. 3.5: Typical pulse height spectrum integrated for one measurement taken with the surface barrier detector downstream of the electron cooler for a ${}^4\text{He}_2^+$ beam at 8.3 MeV. The pulse height corresponds to the energy deposited by the impinging particles. The arrows and the numbers indicate the three peaks in the pulse height spectrum corresponding to (1) a single He, (2) two He and (3) two He, one of which hits a spot with reduced efficiency. The dashed lines mark windows for the identification of the peaks. The background in the adc channels is so small that it is not visible in this scale.

screen is situated at the end of the chamber in front of a window. A CCD camera outside of the chamber records the light spots on the phosphor screen corresponding to particles hitting the front side of the MCP. A photo multiplier switches off the phosphor screen voltage when it detects a light spot. This takes less than $10\mu\text{s}$ and prevents fragments of other events showing up on the same camera frame, so that each camera picture shows fragments of 0 or 1 event. The spot positions and intensities of each picture are put on disc for further analysis.

There is another detector between the first and second dipole magnet downstream of the electron cooler. This one is on a horizontal linear feed-through and can detect and count charged particles with a mass-to-charge ratio different from that of the stored ion beam. Such particles can be atomic ions that underwent recombination or charged molecular fragments, e. g. stemming from dissociative excitation (DE).

3.3.3 Energy dependent collision measurements with the electron cooler

When the electron beam of the electron cooler is used in an experiment as a target for electron-ion reactions like dissociative recombination, it provides electrons at variable detuning energies E_d . Measurements on the molecular DR rate coefficient using the electron cooler in this way generally work as follows: After the injection of the ions into the TSR the electron beam velocity is matched to the ion beam velocity during an appropriate time of phase space cooling which can range between 1 second for HD^+ and more than 10 seconds for heavy molecular ions like CF^+ . Then the electron lab energy E_e is varied in fast cycles, so that the detuning energy jumps between the cooling energy $E_d=0$ eV, the detuning energy E_d^{meas} at which the rate coefficient shall be measured during this injection and a reference energy E_d^{ref} . The count rate at E_d^{ref} is used for a relative normalization to the number of stored ions, because the applied molecular ion current is usually too low to be measured efficiently with the diagnostic tools at the TSR.

3 Experimental method

The dwell times spent on the individual steps of the cycles are chosen to balance the interests of perfect beam cooling and data taking efficiency at the energies E_d^{meas} and E_d^{ref} . The dwell time spent for cooling is T_c , T_r the time at reference energy and T_m the time at a measurement energy.

During each of these cycle steps the neutral particle events are recorded, together with a histogram of the detector pulse heights. As explained above the pulse height is a measure of the total energy or mass of the particles observed (Fig. 3.5). In the further analysis, the number of counts corresponding to a certain particle mass window in the pulse height spectrum are summed up during each of these cycles as indicated in Fig. 3.5. The observation of the full particle mass is interpreted as a DR or DC event (Eqs. 2.1 and 2.10), while the observation of a fraction of it is referred to as a DE event (Eqs. 2.8 and 2.9). A relative DR rate coefficient α_{DR} is obtained by dividing the DR count rates R_{DR}^{meas} at the measurement energy E_d^{meas} by the ion current normalization, e. g. the DR count rate R_{DR}^{ref} at E_d^{ref} . The result is normalized to the electron density in the electron cooler during the individual steps.

If the purpose of the measurement is to acquire the DR rate coefficient α_{DR} as function of detuning energy E_d , E_d^{meas} is varied from injection to injection until the desired energy range is covered. If necessary, i. e. if dissociative charge exchange is a strong process (Eq. 2.10), a background has to be subtracted from the obtained rate coefficient. The measured rate coefficient contains counts of fragmentation events stemming from the toroidal regions of the electron cooler, where the electron beam is bent into and out of the ion beam [LWH⁺96]. In that part the angle between electron beam and ion beam and the change of the space charge yield a collision energy different from E_d in the parallel overlap region. The effect is corrected for in an iterative procedure [LWH⁺96].

The thus observed DR rate coefficient $\tilde{\alpha}_{DR}$ is the total DR rate coefficient of all DR processes, i. e. it is the sum over all possible atomic final states nn' and the average over all rovibrational initial states of the molecular ion with weights p_{vJ} according to their occurrence in the ion beam:

$$\tilde{\alpha}_{DR}(E_d, t) = \sum_{vJnn'} p_{vJ}(t) \alpha_{DR}^{vJnn'}(E_d) \quad (3.4)$$

where $\alpha_{DR}^{vJnn'}$ denotes the DR rate coefficients for specific initial and final states and $\sum p_{vJ}(t)=1$. In the standard rate measurements at the TSR, the final states cannot be distinguished. For that one needs fragment imaging that allows to extract the kinetic energy released.

3.4 A new arrangement for high resolution collision experiments

In fast beam electron-ion collision experiments, where the ion beam velocity can be very well defined by electron cooling, the temperature of the electron beam becomes the limiting factor for the energy resolution that can be achieved in measurements of the rate coefficient. Reducing further the electron temperature of $kT_{\perp}=4.5$ meV [ARD⁺03] that is currently available at the TSR would open up the exploration of an additional low energy range and to resolving structures of much smaller widths.

This became possible with the installation of an ultra-cold electron beam device, the electron target (Sec. 3.4.1), as part of the TSR. It can provide an electron beam from a 80 K photocathode. At the same time a new neutral fragment beamline (Sec. 3.4.2) and detector station and several new detectors for rate and imaging experiments were put into operation (Sec. 3.4.3). The new data acquisition system for rate measurements is described in Sec. 3.4.4.

Measurements on a molecular system that greatly profits from the improved energy resolution, HD⁺ with its low-energy rotational resonances, are discussed later in this work (Ch. 5).

3.4.1 The ultra-cold electron beam device

In 2004 a second electron cooler device was introduced into the ring and put into operation. This *electron target* got its name due to its primary purpose of serving as target in high resolution measurements. A detailed description can be found in [Spr04, SLO⁺04].

The electron target is positioned in the straight section of the TSR opposite of the injection as can be seen in Fig. 3.6. It can be moved out of the ring on rails to make room for the laser cooling section which also uses this part of the ring for experiments.

The electron beam can be produced from a thermal cathode or from a liquid nitrogen (LN) cooled GaAs-photocathode [OWS⁺04]. In combination with the adiabatic magnetic expansion and slow (adiabatic) acceleration, the latter allows to achieve an energy resolution in electron-ion collision rate measurements corresponding to an electron energy distribution with $kT_{\perp}=0.6$ meV and $kT_{\parallel}=0.025$ meV (Sec. 5). The superior resolution is paid for with much lower electron density in the order of $n_e \approx 1 \cdot 10^6$ cm⁻³. With the thermal cathode much higher densities of $n_e \geq 2 \cdot 10^7$ cm⁻³ are available.

In contrast to the electron cooler the electron target is oriented horizontally so that the electron beam is bent into the ring from the inside and not from the top. The electron beam bending radius is 600 mm as compared to 800 mm in the electron cooler, in order to decrease effects of electron-ion interactions at other values of E_d than those in the central overlap section. According to a simulation of the magnetic fields in the electron target, the length of the overlap section

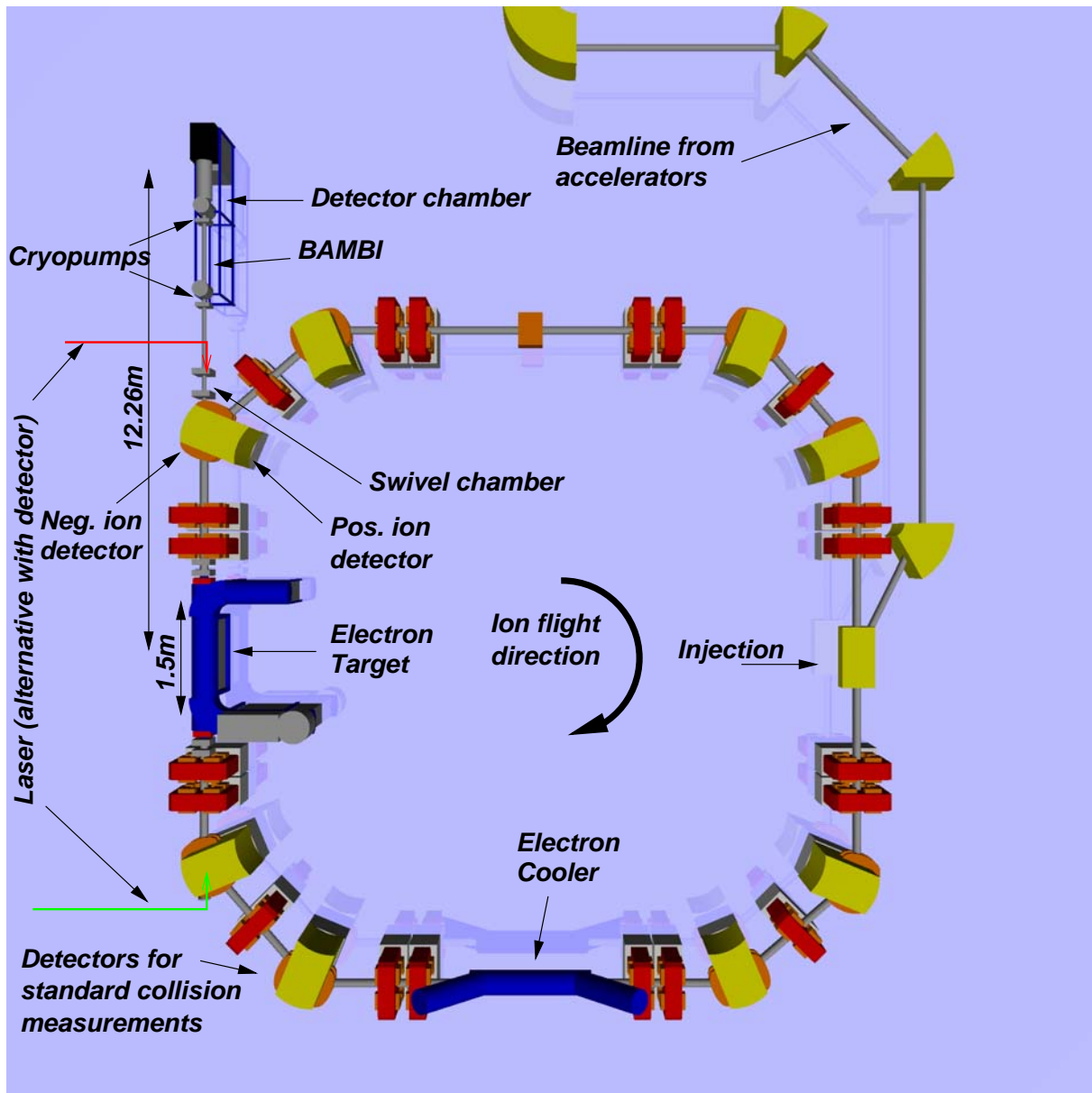


Fig. 3.6: View of the TSR including the new parts taken into operation in 2004, the electron target and the beamline for advanced molecular breakup imaging (BAMBI). The CEI-section is not shown here, because it was deconstructed during the time the measurements with the electron target were performed. The distance from the center of the electron target to the 3d-imaging detector is 12.24(2) m.

is ≈ 1.5 m, varying by 2–3 cm depending on the expansion ratio of the electron beam.

3.4.2 A beamline for advanced molecular breakup imaging (BAMBI)

In order to use the electron beam at the new electron beam device as a target in collision experiments, also new detectors are necessary. Detectors for positive and negative ions were installed to measure at the dipole chamber downstream from the electron target. The positive ion detector is especially used for dielectronic recombination measurements of atomic ions and the main purpose of the negative ion detector is to look for ion pair production in the DR process [Wis02]. A dedicated neutral fragments beamline, BAMBI, was built and equipped with a solid state detector for rate measurements and an innovative 3D-fragment imaging detector adding to the tools for experimental studies. The beamline is about 12 m long as measured from the center of the electron target. This long distance has 2 major advantages:

First, the flight path for the neutral fragments is doubled as compared to the imaging setup in the electron cooler, allowing for twice the particle distances to be reached on the detector. This allows to study in detail the low kinetic energy released region, which is limited to particle distances bigger than the spot sizes. The long distance to the detector yields generally a better relative resolution in the measurement of the projected distances, and it also reduces the effect that the cooler length has on the measured spectrum of projected distances.

Second, the long distance from detector chamber to storage ring allows that the chamber is opened and closed for modifications and maintenance easily. Differential pumping ensures sufficient vacuum conditions close to the TSR. Thus also non-bakeable materials can be used in the detector chamber and generally facilitate the handling.

The beamline consists of a swivel chamber placed directly following the dipole magnet, a removable section of 1.05 m, a straight section of 2.45 m and the detector chamber. The minimum diameter along the direction of flight is 10 cm. The 4 parts can be separated from the TSR and from each other by manual or pneumatic valves. Two titan sublimation pumps and an ion getter pump in the swivel chamber and two cryopumps along the beamline pump the setup. A Leybold RPK 1300 cryopump is placed at about half way along the beamline at the top of a 20 cm cross tube. The second cryopump is a Leybold RPK 800 which pumps the detector chamber. In operation, this system yields pressures of $1\text{--}2 \cdot 10^{-10}$ mbar in the swivel chamber and $2\text{--}3 \cdot 10^{-9}$ mbar in the detector chamber. The pressure in the detector chamber can be reached within 1 day after closing it without baking being necessary, which greatly improves the flexibility of the device.

The swivel chamber has one end fixed to the dipole chamber at the ring, separated from it by a manual valve. The movable side has two ends: One is a CF100 flange with a window and the other is a CF100 bellow separated from the swivel chamber by another manual flange. The

swivel chamber allows to change between two different types of experiments along this side of the ring: For laser experiments, such as the recent test of the validity of time dilation in special relativity [SKE⁺03, Rei05], laser beams co- and counter-propagating the ion beam are sent through the TSR opposite of the injection where the electron target usually is installed. The section was a permanent installation of the ring before the electron target was completed. For these laser experiments the electron target is replaced by the laser cooling section that contains large windows allowing to collect fluorescence light from excited atoms with photo multipliers. The lasers interact with the stored ions in the laser cooling section and enter and exit the ring through a window at the dipole magnet preceding the section and the window in the swivel chamber that is rotated in the appropriate way. The removable part of BAMBI is then taken out to give room for a tower with optical equipment like mirrors and wave plates.

For electron-ion collision experiments the laser cooling section is replaced by the electron target. At the same time, the swivel chamber is rotated and the beamline is completed by inserting and baking the removable part. The setup is illustrated in Fig. 3.6. The detector chamber is thus connected to the TSR.

3.4.3 New fragment detector station

The detector chamber contains two detectors and several feed-throughs for a shutter, a tagged α -source and holders for several grids. Fig. 3.7 shows a vertical cut through the chamber along the beam axis.

Beginning with the last device along the neutral fragment flight path there is a 78 mm diameter two layer MCP with phosphor screen (Hamamatsu F2226-24P) for 3d imaging in front of a CF100 flange with a window. The total distance from the center of the target to the MCP front plate is 12.24(2) m. The typical operating voltages of the detector are: front plate of MCP on ground, 2.0–2.5 kV and 1.6–2.0 kV. The phosphor screen is made of P47 with a fluorescence half life of about 50 ns. Two CCD cameras, one with an optical shutter closing ≈ 20 ns after the impinging of a particle on the MCP, allow to acquire 3d data of dissociation events. Two dimensions are retrieved from the positions of the light spots on the phosphor screen. The timing information is reconstructed from the different light intensities of the spots as they are seen with the normal CCD camera and the fast closing one. Because of the short fluorescence life time, a time difference of 1 ns leads to a significant change. The principles of the technique are explained in [SUP⁺00] and the setup at BAMBI is described in [Nov04] in great detail together with tests and results on the imaging of HD⁺ DR.

An aluminium plate with 1 mm diameter holes on a grid with 10 mm separation in horizontal and vertical directions is mounted on a rotatable feed-through. It can be moved into a position

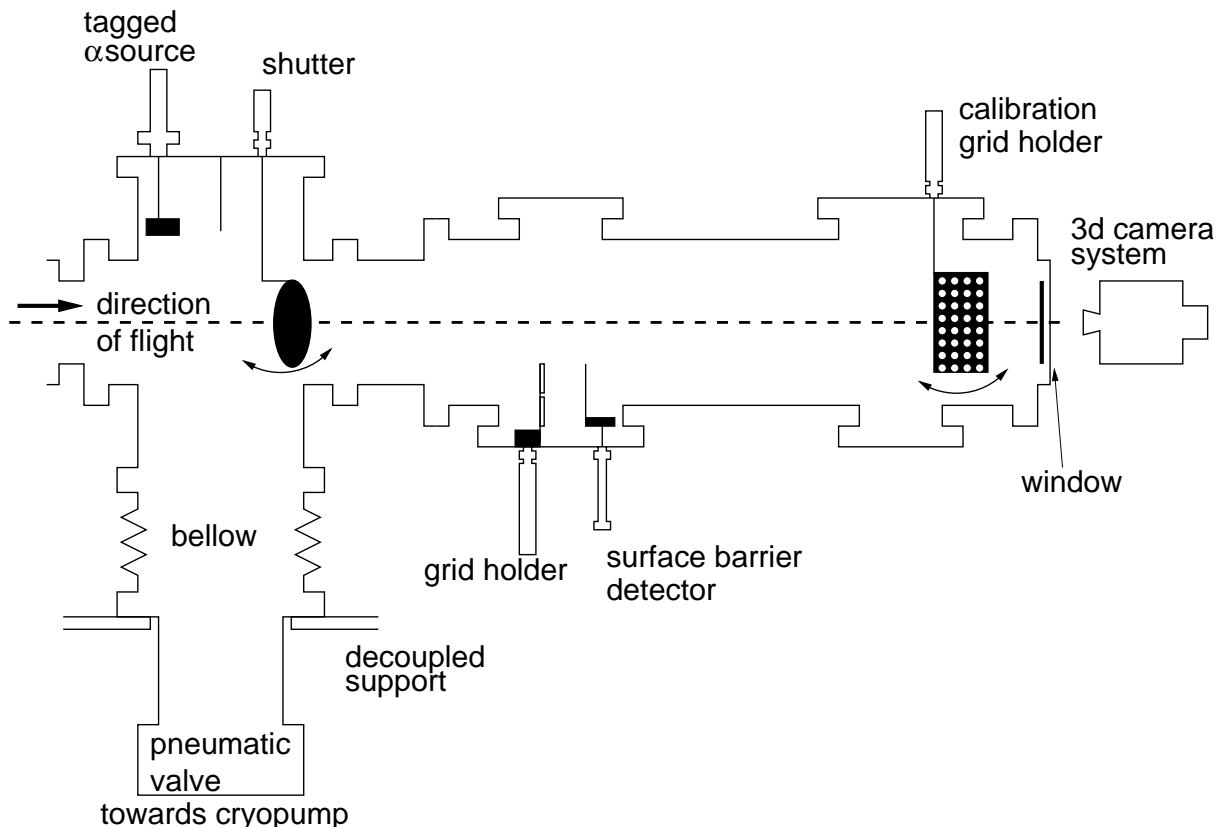


Fig. 3.7: The BAMBI detector chamber seen from the side. It contains a retractable collimated ^{210}Po α -source, a shutter, a holder for two grids or collimators and a retractable surface barrier detector. Furthermore it contains an MCP-phosphor screen and a grid for its spatial calibration. The dashed line indicates the center of the neutral particle flight path.

about 5 mm in front of the MCP to be used for pixel-to-mm calibrations of camera pictures of the detector.

The second detector in the chamber is mounted on a linear feed-through on a CF150 blind flange in order to be moved vertically into the neutral fragment beam. The energy sensitive surface barrier detector (Micron Semiconductor Ltd., MSX25–300) is placed at a distance of approximately 11.75 m from the center of the electron target. Its active area is $50 \times 50 \text{ mm}^2$, but it is slightly reduced by an aperture of $48 \times 48 \text{ mm}^2$ to suppress particles hitting the edges of the active area where they could produce signals comparable to those responsible for peak 3 in Fig. 3.5. The usual operation voltage is 36 V. This detector is used for DR rate measurements.

On the same flange just in front of the detector there is another linear feed through. It supports a frame that can contain foils of different transmission needed for the determination of branching ratios. Instead of the foils it can also hold collimation grids or blinds or other devices to be put in front of the detectors. The frame allows a size of $50 \times 50 \text{ mm}^2$ for the inserted pieces.

In order to protect the detectors from the neutral particle beam when necessary, a shutter is installed on a rotatable feed-through. It is mounted in a rather big chamber of 20 cm diameter in the vertical direction, so that it does not prevent efficient pumping by reducing the open cross section of the beam pipe. The actual shutter is a 8-cm diameter aluminium disc. Its movement is controlled pneumatically and there is a position readback.

On the same flange another linear feed-through is installed that holds a monoenergetic collimated ^{210}Po α -source used to test and calibrate the detectors. The collimation still allows the emitted α -particles to hit everywhere on the MCP at the end of the detector chamber, if the source is moved to the center of the beamline. There is a thin DLC foil in front of the source so that emitted α -particles lose some energy and create electrons that are accelerated towards a small MCP which thus yields a signal indicating the passage of an α -particle. When not in use the source is retracted behind an aluminium shield to block radiation from hitting the detectors. The setup and applications of the α -source are described in [Nov04].

3.4.4 The new data acquisition system

Together with the electron target and the new rate detectors, a new system for the control of the experimental procedure and the data acquisition was developed especially for the rate measurements. The MiLeDAQ (Michael Lestinsky Data Acquisition) software [Lesed] is very versatile. It controls almost all parameters of the experiment: injection of the ions, extraction of the electron beams in electron target and cooler and the acceleration voltages, the opening and closing of the shutter. Simultaneously it reads out and stores the data acquired in ASCII format. It also is used in atomic ion dielectric recombination experiments.

This new system was configured for the present measurements, setting up in particular the parameter file 'exp_molec.h' and the program file 'molec.c'. They are compiled at the start of each measurement. The parameter file is written at the beginning of the raw data file.

A typical rate measurement begins with the program making sure that the shutter should be closed at the injection. When this is assured, an injection is asked for and the program waits for the signal that the injection happened. The times of asking for and receiving of the injection signal are documented in the raw data file. The first seconds after the injection are spent with phase space cooling during which the electron target voltage is set to have $E_d=0$ eV. The phase is divided into a variable number of steps. During each of these and any later steps, the pulse height of each detector signal is recorded by an ADC and written to file. Up to 8 ADC can be read out in parallel. The total time since the injection, the duration of the step, the acceleration voltage and electron current of electron target and cooler are recorded by a multiscaler with 32 channels that is read out at the end of each step.

After the phase space cooling a measurement scheme follows. It is similar to the schemes for measurements with the electron cooler (Sec. 3.3.3). For a specified number of times (cycles) the electron target voltage is varied rapidly (~ 50 ms) between the measurement voltage, the reference voltage and the cooling voltage. The times spent for measurement, reference and cooling can be chosen individually. The start and end of each of the cycles and steps is marked together with a timestamp relative to the reception of the injection signal. After each jump in voltage the program waits for a short time (~ 5 ms), before new data is taken so that the target voltage can reach the new value. During the readout phases the ADC and scaler are locked to prevent any signals from being counted.

After the desired number of cycles is completed, an independent scheme is followed to measure the energy range around $E_d=0$ eV in a short sweep. This is necessary, if the electron cooler and electron target are used in parallel to identify the exact voltage where the electron beam velocities are equal and to detect possible drifts between the two acceleration voltages (Sec. 5.1). At the end of the measurement of an injection, the shutter is closed, if this is specified by the settings. During the next injection, another measurement voltage will be used. The measurement voltages are increased linearly in the laboratory frame.

During the measurement the target or the cooler can be switched off for a certain time and the shutter can be opened, closed and reopened. The program checks at the end of each step, if it is time to do one of the above actions. The time of switching on or off the target is written to the data file, as well as the times when the shutter starts to move and finishes its movement.

With its capacity of handling 8 ADC, the system can be extended to measure with several detectors at the same time, e. g. the surface barrier detector at BAMBI, the negative ion detector in the dipole chamber and the surface barrier detector at the electron cooler neutral fragment chamber (Sec. 3.3.2). Pairs of these detectors have been used in parallel in recent experiments. The raw data files are currently read by a C-program 'md2h.c' (MiLeDAQ to hbook) that converts the raw data into histograms of ADC spectra, detector counts for certain masses (like in Fig. 3.5) as a function of time after injection or of the voltage at the measurement step for each of the 3 cycle steps separately, etc. The histograms are collected in hbook-files readable with the CERN analysis program PAW [paw]. A transfer to the Root analysis program [roo] which is also by CERN is planned for the near future.

4. Franck-Condon suppressed dissociative recombination in He_2^+

The effects of internal excitation on the DR of He_2^+ were studied with the two isotopomers $^3\text{He}^4\text{He}^+$ and $^4\text{He}_2^+$. With the CEI technique (Sec. 3.2) the vibrational populations were measured after different times of storage and electron interactions (Sec. 4.1). A method to measure an absolute DR rate coefficient is discussed and applied (Sec. 4.2), to obtain an absolute scale for the results of the further measurements. The influence of collisions with 0 eV-electrons, with eV-electrons and with residual gas species on the internal excitation was studied. The strong dependence of the DR rate coefficient on the internal excitation (Sec. 2.4) was used as a very sensitive tool to measure this. The energy dependence of the DR rate coefficient was measured for several time intervals for $^4\text{He}_2^+$ and is compared to a DR spectrum of cold $^3\text{He}^4\text{He}^+$ (Sec. 4.6). Most of the results on $^3\text{He}^4\text{He}^+$ presented here were published in [PBA⁺05].

Tab. 4.1: Table of experimental conditions in the He_2^+ measurements presented in this chapter. n_e is the electron density at the electron cooler at cooling energy and E_i is the ion beam energy.

Species	Method	E_i [MeV]	n_e [10^6 cm^{-3}]	E_d^{ref} [eV]
$^3\text{He}^4\text{He}^+$	DR	7.28	12	7.3
	CEI	7.28	12	–
$^4\text{He}_2^+$	DR	8.32	11	23.5
	DR	3.83	5.3	7.3
	CEI	8.32	11	–
	DR	6.41	8.8	7.4

4.1 Vibrational excitation as a function of time in He_2^+ – CEI results

At the TSR the CEI method (Sec. 3.2) was used for both $^3\text{He}^4\text{He}^+$ and $^4\text{He}_2^+$ to gain information on the vibrational population of the molecular ions in the stored beam. In the case of the infrared

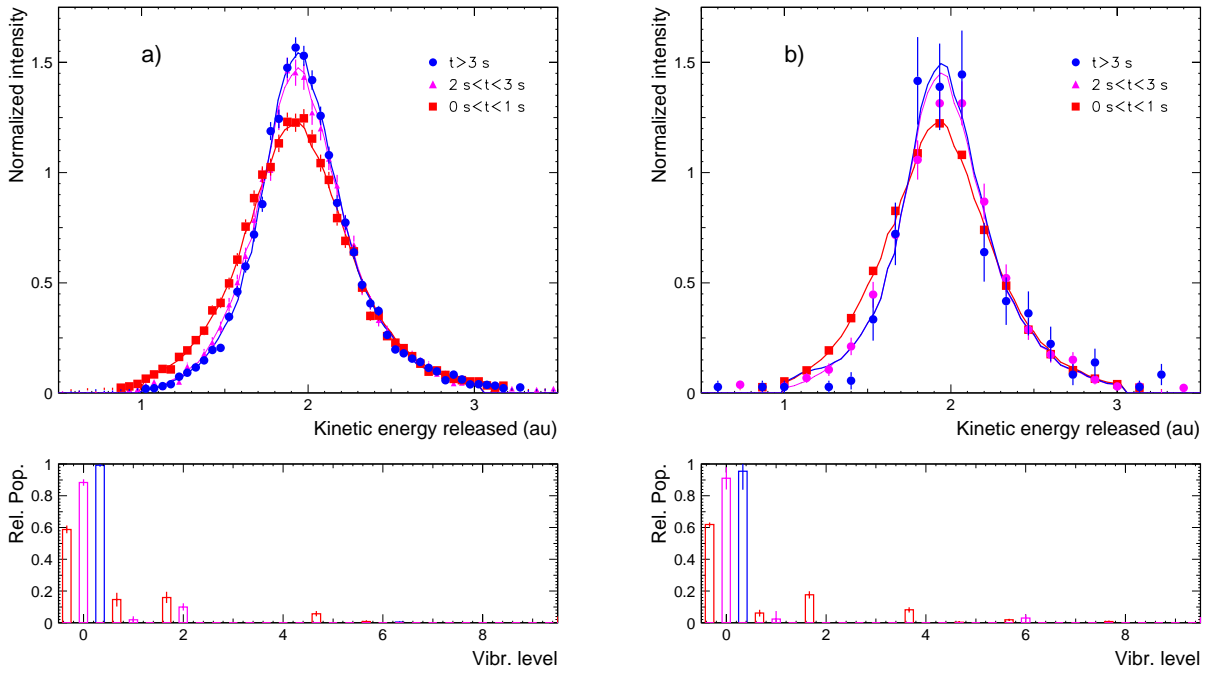


Fig. 4.1: Upper row: Normalized distribution of kinetic energy releases after foil induced Coulomb explosion of ${}^3\text{He}{}^4\text{He}^+$ ions extracted from the stored ion beam during distinct time intervals after injection as shown in the figures. The markers are experimental data, the lines of the same colour represent the least-squares fits to the measured distributions. Lower row: The vibrational level populations as were found in the least-squares fits, given in the colour corresponding to that of the underlying data set. a) Without electron cooling. b) With electron cooling.

active ${}^3\text{He}{}^4\text{He}^+$ this was mainly done to verify, that relaxation to the vibrational ground state ($v=0$) occurred within a certain time after the injection. In contrast, for ${}^4\text{He}_2^+$ the distribution of the vibrational population was followed as a function of time under various experimental conditions, and actively used in the evaluation and interpretation of the DR experiments.

4.1.1 The infrared-active, heteronuclear ${}^3\text{He}{}^4\text{He}^+$

The CEI measurements of ${}^3\text{He}{}^4\text{He}^+$ were carried out at an ion velocity of $E_i=7.28$ MeV. The ions were injected into the storage ring and then extracted slowly over several seconds. In a first measurement, no electron cooling was applied, i. e. the stored molecules were allowed to thermalize. Ions were extracted for storage times of 0 to 10 s. The distribution of the measured kinetic energy released for several storage time intervals is plotted in Fig. 4.1 a) along with the results of least-squares fits used to determine the underlying vibrational population [PBA⁺05]. Directly after the injection considerable vibrational excitation is found (red data set): The vibrational ground state makes up only 58.8(2.5) % of the total population during the first second

after injection. About 30 % are formed by the sum of the vibrational level population of $v=1$ and $v=2$. The remaining 10 % of the total molecular ion population occupy states of higher vibrational excitation. 2 seconds later (2–3 s after injection), the ground state population increases to 88(2) % (purple), and for the molecules extracted after more than 3 seconds of storage (in blue), the contribution of other states is down to 0.8(0.9) %. Within the accuracy of the CEI technique, this corresponds to the vibrational population expected for a thermalized sample at 300 K, where the population of $v=0$ is ≥ 99.9 %.

In a second experiment the $^3\text{He}^4\text{He}^+$ molecules were allowed to interact with velocity matched electrons of a density of $n_e=1.2 \cdot 10^7 \text{ cm}^{-3}$ in the electron cooler starting from the injection. The electron cooling changed the orbit of the ion beam in a way that extraction to the CEI beamline became nearly impossible for long storage times and data was taken from 0 to 4 seconds after injection and is shown in Fig 4.1 b).

The least-squares fit to determine the vibrational distribution during the first second (red) yields results very similar to those for the data set without electrons. The vibrational ground state population is found to be 61.9(1.3) % in this period. For intermediate storage times of 2–3 s, it increases to 91(7) % and for storage times longer than 3 s the relative population of the vibrational ground state is 95(11) %. Because of the change of the ion orbit in the TSR due to the electron cooling, the amount of data taken later than 2 s after injection is rather small. There are considerably less events available which is expressed by the smaller number of bins in Fig 4.1 b) and the larger error bars in the determination of the vibrational population.

At the level of the CEI accuracy, the time dependence of the vibrational population distribution is the same with and without electron cooling for $^3\text{He}^4\text{He}^+$, and essentially a pure $v=0$ population is found in both cases. This knowledge is necessary for the interpretation of the results of dissociative recombination measurements. It confirms that the presence of low-energy electrons in interaction with the molecular ions does not significantly influence the relative population of the vibrational levels by DR and inelastic collisions (Sec. 2.2).

The results show that the evolution of the vibrational population of the stored $^3\text{He}^4\text{He}^+$ ion sample is governed by the spontaneous relaxation via radiation. The radiative lifetimes of vibrational levels of this molecule were found to be between 0.2 and 1.0 s [UDS⁺05].

4.1.2 The homonuclear $^4\text{He}_2^+$

The heavy homonuclear Helium dimer ion is infrared-inactive, i. e. the vibrational population distribution does not change by spontaneous emission of radiation. Therefore collision processes alone are responsible for the evolution of the vibrational population.

The molecular ions were injected into the storage ring at an ion beam energy of $E_i=8.32 \text{ MeV}$

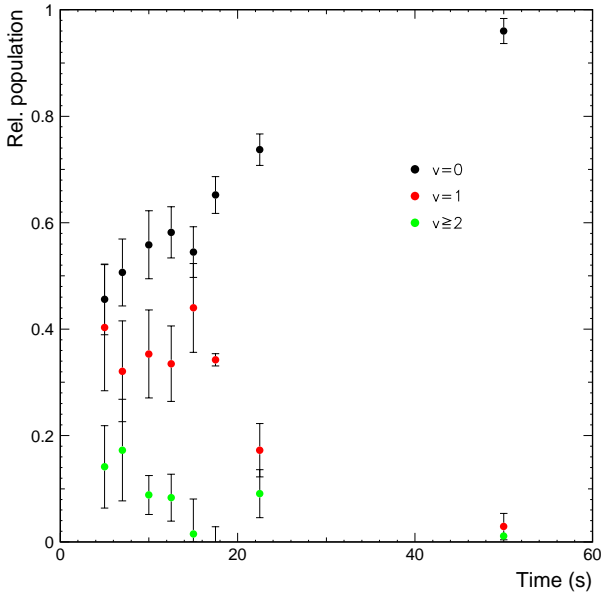


Fig. 4.2: The relative vibrational populations of $v=0$, $v=1$ and all states with $v \geq 2$ of stored ${}^4\text{He}_2^+$ as measured with the CEI technique at ($E_i=8.32$ MeV) plotted as a function of the time of electron cooling prior to extraction. The electron beam was switched off with beginning of the extraction.

which yields the same beam velocity as for the ${}^3\text{He}{}^4\text{He}^+$ (Sec. 4.1.1). The ion beam was cooled by an electron beam of $n_e=1.1 \cdot 10^7 \text{ cm}^{-3}$ in the electron target for a certain, variable time between 5 and 50 s, after which the electron beam was switched off. Then ions were extracted from the storage ring to the CEI setup for 7 s and the vibrational distribution determined.

In Fig. 4.2 the vibrational population distribution is plotted as a function of storage time with electron cooling. The populations were measured for 5, 7, 10, 12.5, 15, 17.5, 22.5 and 50 s of electron cooling.

One finds that with time the vibrational excitation of the sample is continuously reduced. After 5 s, the ground state population is 46(7) % of the total molecular ions and it increases to 96.0(2.4) % after 50 s of electron cooling in the TSR. Less than 20 % of the ions were found in vibrational levels with $v \geq 2$ after 5 s and this contribution vanished within ~ 20 s of electron cooling and the beam consisted almost completely of molecules in the two lowest vibrational states. Separating this fraction of higher excited vibrational levels further, e. g. by single level would not make sense because of the already small overall fraction they form. After 50 s, almost all vibrational excitation in the sample has disappeared. The time it takes for the changes of the vibrational population to happen is much longer than the time in ${}^3\text{He}{}^4\text{He}^+$, for which complete vibrational relaxation happens within 3 s (Sec. 4.1.1).

In order to test, whether collisions with residual gas ions influence the vibrational excitation of the ${}^4\text{He}_2^+$ molecules significantly, the vibrational population was monitored as a function of time in the following experiment: The ion beam was electron cooled beginning from the injection into the TSR. After 22.5 s, the electron beam was switched off and molecules were extracted for as long as 37.5 s. The results are shown in Fig. 4.3. The data is split into 3 subsets

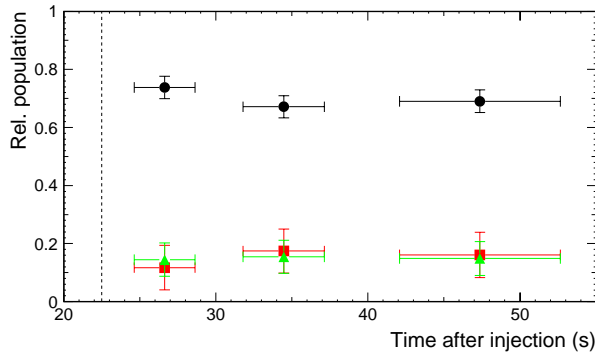


Fig. 4.3: The relative vibrational populations of $v=0$ (black), $v=1$ (red) and all states with $v \geq 2$ (green) of stored ${}^4\text{He}_2^+$ as measured with the CEI technique are plotted vs. time of storage. The electron beam was switched off after 22.5 s. The total data is split into 3 subsets according to the time after injection the events were measured. The times indicate the average time of the events in the subset, with the errorbars being the rms on the time distribution. The dashed line indicates the time when the electron cooling ends.

of approximately equal size, divided according to the time when the event was recorded. The average times after injection in the three subsets are 26.6, 34.5 and 47.4 s.

There is a small decrease of the population of the vibrational ground state corresponding to an increase of vibrational excitation due to collisions with the residual gas. An upper limit for the vibrational excitation process cross section can be estimated from this decrease through

$$\sigma_{EX}^g = \frac{\ln(p_0(t_2)) - \ln(p_0(t_1))}{(t_2 - t_1)n_g v_i}, \quad (4.1)$$

where $p_0(t)$ is the population of the vibrational ground state at time t . Using $n_g = 2.7 \cdot 10^6 \text{ cm}^{-3}$ at a pressure of $P = 1 \cdot 10^{-10}$ mbar and $T = 293$ K, and an ion beam velocity $v_i = 1.41 \cdot 10^9 \text{ cm s}^{-1}$ (corresponding to $E_i = 8.32$ MeV), a value of $\sigma_{EX}^g = 1.7 \cdot 10^{-18} \text{ cm}^2$ is obtained as upper limit for the cross section for excitation through collisions with the residual gas from $t_1 = 26.6$ s and $t_2 = 47.4$ s.

In all, it can be concluded that there is only slow reexcitation of vibrational levels by residual gas collisions and that the data in Fig. 4.2 is not strongly biased by this effect.

4.2 Absolute DR rate coefficients at high electron energy

The usual measurement procedure at the TSR for DR rate coefficients of energy yields rates relative to the rate at a reference energy E_d^{ref} , as was explained in Sec. 3.3.3. To obtain an absolute rate coefficient as function of energy, the absolute DR rate coefficient at E_d^{ref} has to be measured, which is a difficult task. The simplest way is to normalize the count rates to the ion current. But unlike with atomic ions, standard molecular ion beams are generally too weak to allow their measurement during storage with the techniques present at the TSR. And even if stronger beams can be delivered, the ion current usually has to be kept rather low – in the range of 10–100 nA [ARD⁺03] – because else the neutral fragment rates from DR and DE would

be so high that they could damage the solid state detector. Therefore other ways need to be followed, like in the case of the He₂⁺.

4.2.1 A method for an absolute normalization without measuring the ion current

One method, which will be used here, is to measure the molecular ion beam decay under two conditions and deducing the absolute rate coefficient from the change in the lifetimes. Such a method of comparing lifetimes has been used in previous storage ring experiments to measure the absolute DR rate coefficient of LiH⁺ [KLG⁺01] without going into details about the method and another one was described in very much detail when it was applied to ³He⁴He⁺ [PBA⁺05]. Also studies on the SEC of H₂⁺ were done based on the observation of the beam lifetimes [TTK⁺99].

We want to introduce an experimentally very simple method to obtain absolute rate coefficients here, which became possible at the TSR because of the existence of both electron cooler and electron target. A very obvious choice of two conditions, under which one can compare the beam lifetimes, are one without the electron beam and one with the beam thus inducing DR reactions. This can be done by switching on or off the electron beam in the electron target during a measurement after a given time while constantly phase space cooling the ion beam with the electron cooler. As long as all rate coefficients are constant, the ratio of the number of ions reacting and the number of ions stored in the ring is a constant. The number of stored ions $N_{i,off}$ changes according to

$$\dot{N}_{i,off} = -N_{i,off} \cdot [k_{DE,g} + k_{DR,g} + \eta_c (k_{DE,c} + k_{DR,c})] \quad (4.2)$$

while the electron target is off, with $k_{DE,g}$ and $k_{DR,g}$ the rate constants for residual gas induced DE or DC (Eqs. 2.9 and 2.10), respectively. The subscript DR is used instead of DC, because the resulting fragments are the same for the two, allowing for a simpler notation. It should be clear, that DR,g stands for dissociative charge exchange. $k_{DE,c}$ and $k_{DR,c}$ are the rate constants for the processes occurring due to the electron beam in the electron cooler and $\eta_c = l_c/L$ the ratio of cooler length l_c and storage ring circumference L .

When in addition the second electron beam at the electron target is on and the detuning energy is set to $E_d = E_d^{ref}$ the differential equation Eq. 4.2 changes to

$$\dot{N}_{i,on} = -N_{i,on} \cdot [k_{DE,g} + k_{DR,g} + \eta_c (k_{DE,c} + k_{DR,c}) + \eta_t (k_{DE,e}^{ref} + k_{DR,e}^{ref})] \quad (4.3)$$

where $\eta_t = l_t/L$ with l_t the overlap length between electron beam and ion beam in the electron target and $k_{DE,e}^{ref}$ and $k_{DR,e}^{ref}$ are the rate constants for the processes occurring due to the electron beam in the electron target. The process of electron induced ion-pair production (Eq. 2.6) is

neglected in this model, its rate coefficient is assumed to be smaller by orders of magnitude than that for DR at the relevant energies.

Equations 4.2 and 4.3 represent differential equations with solutions of the form

$$N_{i,on/off}(t) = N_{i,on/off}(0) \cdot \exp\left(-\frac{t}{\tau_{on/off}}\right) \quad (4.4)$$

where

$$\begin{aligned} \tau_{off} &= \left[k_{DE,g} + k_{DR,g} + \eta_c (k_{DE,c} + k_{DR,c}) \right]^{-1} \\ \tau_{on} &= \left[k_{DE,g} + k_{DR,g} + \eta_c (k_{DE,c} + k_{DR,c}) + \eta_t (k_{DE,e}^{ref} + k_{DR,e}^{ref}) \right]^{-1} \end{aligned}$$

are the ion beam lifetimes. The change in the lifetimes is induced by electrons being in the electron target at $E_d = E_d^{ref}$ as one can see:

$$\begin{aligned} \tau_{on}^{-1} - \tau_{off}^{-1} &= \eta_t (k_{DE,e}^{ref} + k_{DR,e}^{ref}) \\ &= \eta_t \left[k_{DE,e}^{ref} + n_e^{ref} \alpha_{DR,e}^{c+tor}(E_d^{ref}) \right] \end{aligned}$$

where $\alpha_{DR,e}^{c+tor}(E_d^{ref})$ is the observed DR rate coefficient at $E_d = E_d^{ref}$ averaging over the central and toroidal regions of the electron target (Sec. 3.3.3) and n_e^{ref} the electron density. If the ion beam velocity is high enough compared to the kinetic energy released, it can be reasonably assumed that all neutral fragments from dissociations in the electron target hit the detector – that includes the events occurring due to worsening of the vacuum in the electron target section. Then one finds

$$\begin{aligned} \tau_{on}^{-1} - \tau_{off}^{-1} &= \eta_t \left[k_{DE,e}^{ref} + n_e^{ref} \alpha_{DR,e}^{c+tor}(E_d^{ref}) \right] \\ &= \frac{R_{DE,e}^{ref}(t) + R_{DR,e}^{ref}(t)}{N_{i,on}(t)} \end{aligned}$$

with $R_{DE,e}^{ref}(t)$ and $R_{DR,e}^{ref}(t)$ being the electron beam induced part of the count rates on the detector for DE and DR, respectively:

$$R_{DE,e}^{ref} = N_{i,on}(t) \cdot \eta_t k_{DE,e}^{ref} \quad (4.5)$$

$$R_{DR,e}^{ref} = N_{i,on}(t) \cdot \eta_t k_{DR,e}^{ref} = N_{i,on}(t) \cdot \eta_t n_e^{ref} \alpha_{DR,e}^{c+tor}(E_d^{ref}) \quad (4.6)$$

Making use of these identities yields

$$\begin{aligned} \tau_{on}^{-1} - \tau_{off}^{-1} &= \frac{R_{DE,e}^{ref}(t) + R_{DR,e}^{ref}(t)}{N_{i,on}(t)} \\ &= \left[\frac{R_{DE,e}^{ref}(t)}{R_{DR,e}^{ref}(t)} + 1 \right] \frac{R_{DR,e}^{ref}(t)}{N_{i,on}(t)} \\ &= \left[\frac{R_{DE,e}^{ref}(t)}{R_{DR,e}^{ref}(t)} + 1 \right] \eta_t n_e^{ref} \alpha_{DR,e}^{c+tor}(E_d^{ref}) \end{aligned}$$

which is solved for $\alpha_{DR,e}^{c+tor}(E_d^{ref})$ in the form of

$$\alpha_{DR,e}^{c+tor}(E_d^{ref}) = \frac{\tau_{on}^{-1} - \tau_{off}^{-1}}{\eta_t n_e^{ref}} \left[1 + \frac{R_{DE,e}^{ref}(t)}{R_{DR,e}^{ref}(t)} \right]^{-1} \quad (4.7)$$

$$= \frac{\tau_{on}^{-1} - \tau_{off}^{-1}}{\eta_t n_e^{ref}} \left[1 + \frac{R_{DE,e+g}^{ref}(t) - R_{DE,g}(t)}{R_{DE,e+g}^{ref}(t)} \frac{R_{DE,e+g}^{ref}(t)}{R_{DR,e+g}^{ref}(t) - R_{DR,g}(t)} \right]^{-1} \quad (4.8)$$

with $R_{DE,g}(t)$, $R_{DE,e+g}^{ref}(t)$, $R_{DR,g}(t)$, $R_{DR,e+g}^{ref}(t)$ being the rates on the detector for DE and DR being induced by the residual gas only or the total count rate when the electron target beam is switched on, respectively.

$$R_{DE,g}(t) = N_{i,off}(t) \cdot \rho_{DE} \cdot k_{DE,g} \quad (4.9)$$

$$R_{DE,e+g}^{ref}(t) = N_{i,on}(t) \cdot [\rho_{DE} \cdot k_{DE,g} + \eta_t \cdot k_{DE,e}^{ref}] \quad (4.10)$$

$$R_{DR,g}(t) = N_{i,off}(t) \cdot \rho_{DR} \cdot k_{DR,g} \quad (4.11)$$

$$R_{DR,e+g}^{ref}(t) = N_{i,on}(t) \cdot [\rho_{DR} \cdot k_{DR,g} + \eta_t \cdot k_{DR,e}^{ref}], \quad (4.12)$$

where ρ_{DE} and ρ_{DR} are the constant fractions of the residual gas induced DE and DR (exactly DC) events, respectively, that hit the detector – events occurring e. g. in the dipole sections of the storage ring don not hit the detector. The only time when all these rates (Eqs. 4.9–4.12) can be measured at the same time is $t = t_0$ when the electron beam of the target is switched. This yields the final result of

$$\alpha_{DR,e}^{c+tor}(E_d^{ref}) = \frac{\tau_{on}^{-1} - \tau_{off}^{-1}}{\eta_t n_e^{ref}} \left[1 + \frac{R_{DE,e+g}^{ref}(t_0) - R_{DE,g}(t_0)}{R_{DE,e+g}^{ref}(t_0)} \frac{R_{DE,e+g}^{ref}(t_0)}{R_{DR,e+g}^{ref}(t_0) - R_{DR,g}(t_0)} \right]^{-1} \quad (4.13)$$

All the count rates and ratios can be taken in one single measurement, making this a very convenient method for the measurement of the absolute rate coefficient. The conditions are summarized below for convenience:

- All fragments that are created due to the electron beam being switched on have to hit the detector - independent of if they are due to processes involving electrons or due to collisions with ions trapped by the ion beam. The ion beam velocity has to be high enough compared to the kinetic energy released in the fragmentation. This also means that channels like the ion-pair formation have to be negligible or need to be measured in addition.
- The rate coefficients of all processes have to be constant as a function of the measurement time, i. e. it has to be taken care of rovibrational excitation and deexcitation during the

measurement. This includes not only the processes in the electron target, but also those in the electron cooler.

One has to be aware that the absolute rate coefficient obtained in this manner still includes the effects caused by the toroids (Sec. 3.3.3,[LWH⁺96]), so it is necessary to also make a measurement of the relative rate coefficient as a function of energy at the same magnetic expansion ratio of the electron target beam to extract the real rate coefficient.

4.2.2 Absolute rate coefficients of both He₂⁺ species

The absolute rate coefficient of both ³He⁴He⁺ and ⁴He₂⁺ was measured using the above described procedure allowing a direct comparison of the absolute rate coefficients of the two species. The beam energies for the experiment were $E_i=7.28$ MeV for ³He⁴He⁺ and $E_i=6.41$ MeV for ⁴He₂⁺. This means the beams had the same rigidity which simplified the experiment in the way, that the storage ring magnetic fields remained untouched when the measurement was changed from one ion beam to the other. The electron cooler was switched on all the time and the electron density was $n_{e,c}=1.2\cdot 10^7$ cm⁻³ in the measurement of ³He⁴He⁺ and $n_{e,c}=8.8\cdot 10^6$ cm⁻³ for ⁴He₂⁺.

Beginning with the injection, both electron cooler and electron target were switched on and set to cooling ($E_d=0$ eV). This electron cooling phase lasted 30 s, then the electron target was switched off and the neutral particle rates originating from residual gas collisions in the electron target section at the surface barrier detector at BAMBI were recorded. After 15 s, the electron beam in the target was switched back on, now at $E_d^{ref}=7.4$ eV and the neutral count rates were measured for further 20 s. The electron density in the electron target at E_d^{ref} was $n_e^{ref}=1.2\cdot 10^7$ cm⁻³ in the measurement of ³He⁴He⁺ and varied between $n_e^{ref}=1.1\cdot 10^7$ cm⁻³ and $5.5\cdot 10^6$ cm⁻³ when the rate coefficient of ⁴He₂⁺ was measured.

The initial 30 s electron cooling allowed to remove most of the rovibrational excitation from the molecular ion beam. This suppressed the influence of a vibrational state dependence of the rate coefficients, especially in the case of the ⁴He₂⁺ for which the CEI results showed that it is produced with considerable vibrational excitation (Sec. 4.1.2) which disappears after a few tens of seconds of electron collisions with $E_d=0$ eV in the electron cooler. The initial intense cooling and the continuous electron beam at $E_d=0$ eV in the electron cooler were supposed to ensure that the rate constants responsible for the beamloss (Sec. 4.2.1) were constant during the rate measurements after 30 s.

The diameter of the neutral fragment beam was calculated to be less than 40 mm at the detector for a kinetic energy release of 15 eV in both experiments, considerably smaller than the diameter of the solid state detector. With the imaging system (Sec. 3.4.3) it was checked that all neutral

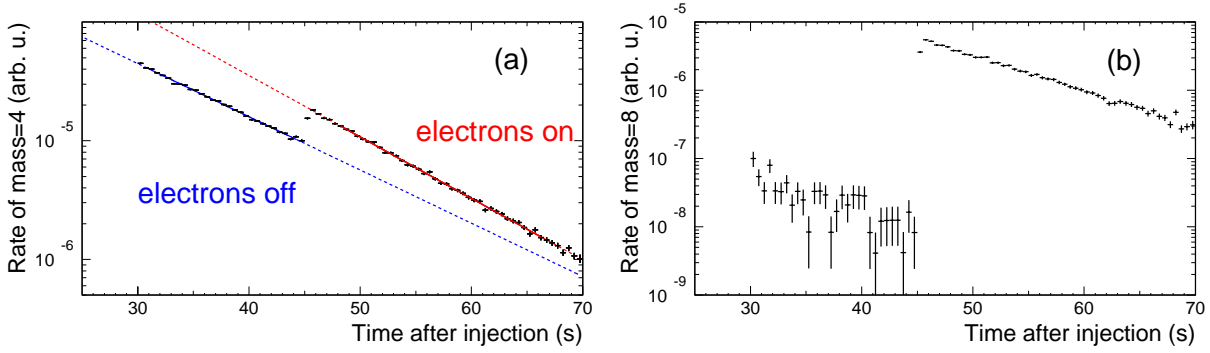


Fig. 4.4: Total count rate of (a) mass=4 (He) and (b) mass=8 ($2\cdot\text{He}$) at the neutral fragment detector as a function of storage time, represented by the black dots. The electron beam is off for $30 \text{ s} \leq T < 45 \text{ s}$. For storage time $T > 45 \text{ s}$ the electron detuning energy $E_d^{ref} = 7.4 \text{ eV}$. Blue: Exponential fit to the data with electrons off. Red: Exponential fit to the data with electrons on. The extracted beam lifetimes are $\tau_{off} = 9.68(6) \text{ s}$ and $\tau_{on} = 8.38(6) \text{ s}$.

fragments from the DR at E_d^{ref} hit the detector. The diameter for the ${}^4\text{He}_2^+$ DR at 7.5 eV was found to be less than 30 mm.

The overlap length in the electron target is $l_t = 1.485 \text{ m}$ for ${}^4\text{He}_2^+$ and $l_t = 1.505 \text{ m}$ for ${}^3\text{He}{}^4\text{He}^+$ so that in Eq. 4.13 we find $\eta_t = l_t/L = 0.027$ as overlap ratio between electron beam and ion beam in the electron target¹ and the storage ring circumference $L = 55.4 \text{ m}$. In the case of ${}^3\text{He}{}^4\text{He}^+$ the rate R_{DE} denotes the sum of the rates observed going to the two final channels ${}^3\text{He} + {}^4\text{He}^+$ and ${}^3\text{He}^+ + {}^4\text{He}$. It should be noted that for the observed rates the term 'induced by electrons' not only refers to processes involving electrons directly (Eqs. 2.8 and 2.1), but also to collisions with residual gas ions (Eqs. 2.9 and 2.10) that are trapped by the electron beam, that forms an EBIT (electron beam ion trap) and considerably increases the residual gas pressure in that electron target section.

Fig. 4.4 shows the measured count rates of full mass ($m=8$) (b) and half mass ($m=4$) (a) in one of the measurements with ${}^4\text{He}_2^+$ at an electron density in the target of $n_e^{ref} = 1.1 \cdot 10^7 \text{ cm}^{-3}$. The ion beam lifetimes with and without the electron beam in the electron target are extracted from the single He rate in Fig. 4.4(a). One can also extract the ratio of the residual gas DE to the DE that is induced by the presence of the electron beam in the target. This is done from the values of the exponential fits at the time of the switching on of the electron beam. In Fig. 4.4(b) one can see that the DR rate that is induced by residual gas collisions is about 0.5 % of the DR rate due to the electrons and thus is negligible in this measurement. The DR rate coefficient at E_d^{ref} is constant at the late storage times of $T \geq 45 \text{ s}$ as is indicated by Fig. 4.5.

Averaging over the values extracted for the absolute DR rate coefficient in this way

¹ The exact overlap length depends on the expansion ratio employed in the electron target

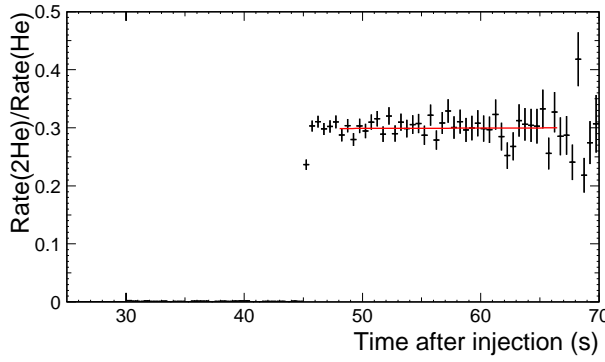


Fig. 4.5: The ratio of double He rate to single He rate that are shown in Fig. 4.4. It is constant as a function of time while the electron beam in the electron target is on – the slope of a first order polynomial fit yields $6(59) \cdot 10^{-5} \text{ s}^{-1}$.

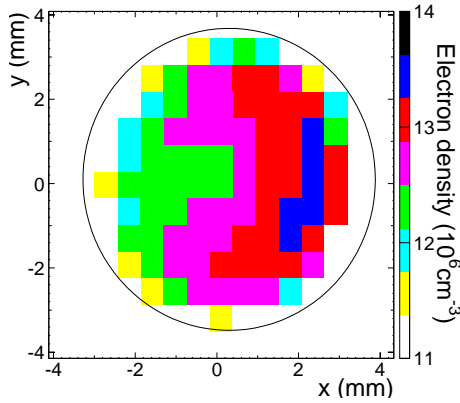


Fig. 4.6: The measured electron beam profile between measurements of the absolute rate coefficient of ${}^4\text{He}_2^+$ at $E_d=0 \text{ eV}$ ($E_e=436 \text{ V}$). The electron density as function of the position is given according to the colour code on the right, ranging between 11 and $14 \cdot 10^6 \text{ cm}^{-3}$. The circle marks the expected beam size according to the expansion factor (20) and the cathode diameter. In the calculation of the density, no correction for the space charge density is taken into account. There is an uncertainty of estimated 5 % on the size in x - and y -direction, the absolute position is arbitrary.

from several measurements one finds $\alpha_{DR}^{c+tor}(7.4\text{eV})=2.0(1) \cdot 10^{-8} \text{ cm}^3 \text{ s}^{-1}$ for ${}^4\text{He}_2^+$ and $\alpha_{DR}^{c+tor}(7.4\text{eV})=2.4(1) \cdot 10^{-8} \text{ cm}^3 \text{ s}^{-1}$ for ${}^3\text{He}^4\text{He}^+$ where the error bars are the standard deviation of the measured values. The statistical errors based on the determination of the ion beam lifetime differences τ_{on} and τ_{off} are of the same relative size ($\sim 5 \%$).

The largest systematic uncertainty enters through the electron density in the electron target n_e , since the electron beam profile is not perfectly homogeneous [Spr04]. A beam profile measured between the absolute rate measurements with ${}^4\text{He}_2^+$ is shown in Fig. 4.6. The electron density in the center of the beam is $n_e=1.25 \cdot 10^7 \text{ cm}^{-3}$ at $E_d=0 \text{ eV}$. In the calculation of the absolute rate coefficient, a homogeneous beam with a diameter of 7.16 mm was assumed corresponding to the cathode size and the expansion factor of 20. This yielded $n_e=1.266 \cdot 10^7 \text{ cm}^{-3}$ at $E_d=0 \text{ eV}$, which means the central value and the average value agree very well. There is an inhomogeneity of about 10 %, from the peak (blue, measured maximum $1.345 \cdot 10^7 \text{ cm}^{-3}$) to the 'platform level' (green, $1.21 \cdot 10^7 \text{ cm}^{-3}$). In addition, an uncertainty in the electron beam size of estimated $\sim 7 \%$ is introduced, since not the detector for the electron beam was moved, but the electron beam, using steering magnets, and the uncertainty is due to the calibration of these magnets.

Another important quantity entering the calculation is the overlap length l_t between electron beam and ion beam. The value applied in the calculation is extracted from simulations of the

magnetic fields in the electron target. Because of this and because of a possible parallel shift of the ion beam within the electron beam away from the center, an uncertainty of ~ 5 cm, or 3 % is assumed. Adding these contributions up, the total systematic uncertainties can be estimated to be below 20 %.

As indicated by the superscript ^{*c+tor*} the rate coefficients given above still average over the rate coefficients of collisions occurring in the central region and in the toroid region (Sec. 3.3.3) where the collision energy is higher. The correction for this is very small (~ 2 %). So we find

$$\begin{aligned}\alpha_{DR}^c(7.4\text{eV}) &= 2.0(1)(4) \cdot 10^{-8} \text{cm}^3 \text{s}^{-1} \text{ for } {}^4\text{He}_2^+ \text{ and} \\ \alpha_{DR}^c(7.4\text{eV}) &= 2.4(1)(5) \cdot 10^{-8} \text{cm}^3 \text{s}^{-1} \text{ for } {}^3\text{He}^4\text{He}^+.\end{aligned}$$

In an earlier experiment at the TSR and with a somewhat different ansatz the toroid corrected absolute rate coefficient of ${}^3\text{He}^4\text{He}^+$ was found to be $\alpha_{DR}^c(7.3\text{eV}) = 2.8(4) \cdot 10^{-8} \text{cm}^3 \text{s}^{-1}$ [PBA⁺05] making use only of the electron cooler.

The absolute rate coefficients obtained by this method rely on the two assumptions discussed in Sec. 4.2.1. If the measured rate coefficients from the TSR are wrong, consequently one of the above assumptions has to be wrong, too. The assumption of constant, i. e. time independent, rate constants for the involved processes in Eq. 4.3 was tested with several experiments. It was feared that the electrons at $E_d = 7.4$ eV in the electron target could excite efficiently vibrations in the He₂⁺ ions via inelastic collisions (Eq. 2.7) once the target is switched on. The excited He₂⁺ would then undergo DR at $E_d = 0$ eV in the electron cooler with a very high rate coefficient – orders of magnitude higher so that even a minute part of the ions could be enough to have a significant effect on the ion beam lifetime. In this experiment it was possible to have the ion beam in the electron cooler section pointing towards the downstream neutral fragment detector (Sec. 3.3.2) for rate measurements and to ensure that all neutral fragments arising from the electron cooler beam can be detected. The rate of DR events, i. e. full mass of beam particles (see Fig. 3.5), hitting the detector indeed increases when the electron target is switched on with $E_d = 7.4$ eV, but only very little. It makes about 2–3 % of the change in the count rate at the neutral fragment detectors at BAMBI downstream of the electron target. This is the order of magnitude of the correction it can introduce on the absolute rate coefficient. The DE rate constant downstream of the electron target does not change when the electron target is switched on. Also measurements without the electron cooler beam were performed and yielded the same results for the absolute DR rate coefficient at $E_d = 7.4$ eV. The excitation by the electron collisions therefore affects the measured DR rate to be too high by about 3 %. A violation of the other assumption means the existence of additional loss processes which are not accounted for, e. g. the ion–pair formation at $E_d = 7.4$ eV. To have a significant effect, the rate coefficient for this would need to be of the same order of magnitude as for the DR rate coefficient. This

could be tested in future experiments. In addition, the method should be applied to a molecule with a well known absolute rate coefficient like HD^+ to test it.

For ${}^3\text{He}^4\text{He}^+$, the absolute normalization of $\alpha_{DR}(7.3\text{eV})=2.8\cdot 10^{-8}\text{cm}^3\text{s}^{-1}$ [PBA⁺05] will be used in the following sections in this work. For ${}^4\text{He}_2^+$ the value obtained, $\alpha_{DR}(7.4\text{eV})=2.0\cdot 10^{-8}\text{cm}^3\text{s}^{-1}$ is applied. The uncertainty of the overall absolute rate coefficients is not included in any error bars.

4.2.3 Comparison to other experiments and to theory

Another storage ring experiment that was performed at ASTRID cites an absolute rate coefficient for the DR of ${}^3\text{He}^4\text{He}^+$ of $\alpha_{DR}(6.4\text{eV})=1.1\cdot 10^{-8}\text{cm}^3\text{s}^{-1}$ [UDS⁺05] with a 50% error due to the multi-step calibration of the ion current. An absolute rate coefficient was measured also for the homonuclear molecule, but the molecules were probably vibrationally highly excited and the shape of the measured rate coefficient as function of energy is not comparable to the ones presented in this work (Sec. 4.6). The value found there is $\alpha_{DR}(7.3\text{eV})\approx 0.5\cdot 10^{-8}\text{cm}^3\text{s}^{-1}$ [UDS⁺05] for the DR of ${}^4\text{He}_2^+$. A theoretical time dependent calculation yields a rate coefficient of $\alpha_{DR}(6.75\text{eV})=1.0\cdot 10^{-8}\text{cm}^3\text{s}^{-1}$ [RO05] for the heteronuclear system and the same model yields $\alpha_{DR}(6.75\text{eV})=0.9\cdot 10^{-8}\text{cm}^3\text{s}^{-1}$ [OR06] for ${}^4\text{He}_2^+$.

This means there is a very good reproduction of the ratio between the rate coefficients of the two systems, but the absolute value is different by a factor of about 2.5. However, the measurements of the absolute rate coefficient of ${}^3\text{He}^4\text{He}^+$ DR is consistent within the measurements at the TSR for different methods using the electron target or the electron cooler, respectively.

4.3 Rovibrational cooling by electron collisions

4.3.1 Time dependence of the DR rate coefficient of ${}^4\text{He}_2^+$

The observations of the evolution of the vibrational populations (Sec. 4.1.2) of stored ${}^4\text{He}_2^+$ showed that electron collisions with $E_d=0\text{eV}$ have a strong influence on the vibrational excitation in the molecular ion beam by removing all vibrational levels other than the vibrational ground state from the population (Fig. 4.2). Without electron cooling almost no change in the vibrational population is observed (Fig. 4.3).

There are two types of electron collision processes that can be responsible for this deexcitation. The first one is the DR itself. If vibrationally excited ions recombine faster than the vibrational ground state ions, one will eventually find a population that is dominated by the slowest-recombining state. This effect can be called 'recombination-driven depletion' and is a

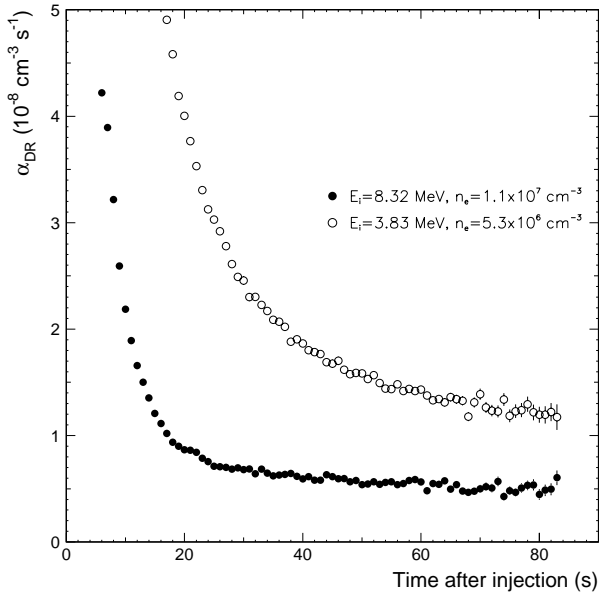


Fig. 4.7: The DR rate coefficient of ${}^4\text{He}_2^+$ $\alpha_{DR}(0 \text{ eV})$ as a function of time for 2 different electron densities n_e and beam energies E_i . The full circles represent the results for $E_i=8.32 \text{ MeV}$, $E_d^{ref}=23.5 \text{ eV}$ and $n_e=1.1 \cdot 10^7 \text{ cm}^{-3}$, the open circles for $E_i=3.83 \text{ MeV}$, $E_d^{ref}=7.3 \text{ eV}$ and $n_e=5.3 \cdot 10^6 \text{ cm}^{-3}$.

destructive mechanism. Evidence for this was observed in storage ring measurements of D_2H^+ [LKL⁺03] at the TSR. Super-elastic collisions (Eq. 2.7) with the low energy electrons represent the second process which can remove vibrational excitation from the molecular ions, in this case without destroying them. The relative size of the respective rate coefficients has to tell about the importance of the processes for the observed vibrational deexcitation.

Knowing about the probably strong dependence of the low energy DR rate coefficient on the vibrational level for the He_2^+ system (Sec. 4) and taking into account Eq. 3.4 one can expect also a strong time dependence of the DR rate coefficient in experiments with intense electron cooling due to the induced change of the internal excitation. The results of such measurements where the DR rate coefficient $\tilde{\alpha}_{DR}(0 \text{ eV}, t)$ is studied as a function of storage time are shown in Fig. 4.7 for two different settings, which differ in electron density, beam velocity and the value of the reference energy, E_d^{ref} . In both cases, the measurements were performed when the electron beam was most of the time at cooling energy, namely with dwell times given by $T_c:T_r:T_m=5:1:0$. The rate coefficient is partly corrected for the contribution from the toroid section in the sense that a constant value was subtracted for all times. The correction was obtained from measurements of the rate coefficient as a function of energy for long storage times for the corresponding conditions (Fig. 4.13). In order to be exact, such a measurement would be needed for all storage times. The applied correction slightly underestimates the real effect. The absolute normalization of the rate coefficient in Fig. 4.7 is done via the absolute rate coefficient obtained in Sec. 4.2.2 and the same measurements as function of energy.

In both measurements, $\tilde{\alpha}_{DR}(0 \text{ eV})$ decreases rapidly with time, the decrease being much faster for the high energy case, where the high electron density is applied as well. In both cases,

the DR-signal declines for the full measuring time, showing that the rovibrational population evolves on a time scale of 50–100 s even with the high electron density. This agrees with the results about the vibrational population evolution obtained with the CEI (Fig. 4.2).

4.3.2 Vibrational state dependent DR rate coefficients $\alpha_{DR}^v(0\text{eV})$ and SEC in ${}^4\text{He}_2^+$

There are theoretical predictions [COS99] that the DR rate coefficient $\tilde{\alpha}_{DR}^{vJ}$ increases by a factor of less than two, if the rotational excitation increases from $J=0$ to $J=9$ within the $v=0$ vibrational level for the direct process while it increases by about an order of magnitude when the vibrational excitation increases from $v=0$ to $v=1$. Assuming that thus the influence of rotational excitation on the DR rate coefficient is considerably smaller than the influence of the vibrational excitation Eq. 3.4 can be simplified to

$$\tilde{\alpha}_{DR}(E_d, t) = \sum_v p_v(t) \tilde{\alpha}_{DR}^v(E_d) \quad (4.14)$$

where $\tilde{\alpha}_{DR}^v$ is the DR rate coefficient for the vibrational level v averaged over the distribution of rotational levels. Combining the knowledge about the absolute DR rate coefficient (Sec. 4.2.2), the evolution of the DR rate $\tilde{\alpha}_{DR}(0\text{ eV}, t)$ (Fig. 4.7) and the vibrational population at several storage times (Fig. 4.2) one can try to extract the DR rate coefficients of the individual vibrational levels, i. e. in our case, $\tilde{\alpha}_{DR}^{v=0}(0\text{ eV})$, $\tilde{\alpha}_{DR}^{v=1}(0\text{ eV})$ and $\tilde{\alpha}_{DR}^{v \geq 2}(0\text{ eV})$. A set of 8 linear equations based on Eq. 4.14 can be formed for the specific storage times t_i , where $i = 1 \dots 8$, at which the vibrational populations $p_v(t)$ were measured independently by CEI. The vibrational level dependent rate coefficient $\tilde{\alpha}_{DR}^v(E_d)$ can then be determined by solving the set of equations. There is one difference between the CEI experiment and the DR measurement: The electron cooling in the CEI experiment is on all the time ($T_c:T_r:T_m=1:0:0$), while for the DR measurements, $T_c:T_r:T_m=5:1:0$ was used. Therefore, the effective electron cooling time at $E_d=E_d^c$ needs to be adjusted, since this dominates the evolution of the vibrational population distribution of the stored ${}^4\text{He}_2^+$ ions as shown in Sec. 4.1.2. In order to compensate for the difference in the cooling duty cycles, results from the CEI experiments after times t_{CEI} of electron cooling are matched with DR rate coefficients after time $t_{DR}=(t_{CEI}-5\text{ s}) \cdot 1.2+5\text{ s}$. In Fig. 4.11 it is shown that the time spent on E_d^{ref} has only little effect on the rovibrational beam composition through SEC, DR induced depletion or inelastic collisions, so these times are neglected. A least-squares fit is used to solve the set of equations. It yields rate coefficients α_{DR} for $v=0,1$ and ≥ 2 which are given in Table 4.2. It shows that the DR rate coefficient in ${}^4\text{He}_2^+$ indeed depends strongly on the vibrational level. For the ground state we find a low rate coefficient of $\alpha_{DR}(0\text{ eV})=3.4(2.0) \cdot 10^{-9}\text{ cm}^3\text{ s}^{-1}$. The rate coefficient of the $v=1$ level is not very well defined, its best value is $\alpha_{DR}(0\text{ eV})=3.2 \cdot 10^{-9}\text{ cm}^3\text{ s}^{-1}$ and an upper limit is $\alpha_{DR}(0\text{ eV}) \leq 2.1 \cdot 10^{-8}\text{ cm}^3\text{ s}^{-1}$.

Tab. 4.2: DR rate coefficients for different vibrational levels in ${}^4\text{He}_2^+$ found in a least-squares fit (see text). The values are averaged over rotational populations which probably changed during the DR rate measurements. Fig. 4.7 sets a limit of $\tilde{\alpha}_{DR}^{v=0} \leq 5 \cdot 10^{-9} \text{ cm}^3 \text{ s}^{-1}$.

vibr. state	$\tilde{\alpha}_{DR} [10^{-9} \text{ cm}^3 \text{ s}^{-1}]$
0	$3.4^{+2.0}_{-2.0}$
1	$3.2^{+17.8}_{-3.2}$
≥ 2	202^{+153}_{-62}

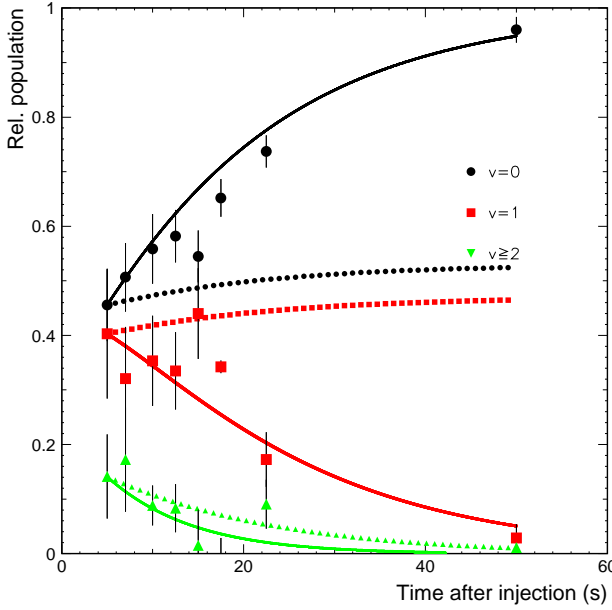


Fig. 4.8: Evolution of the distribution of the vibrational states as measured with the CEI technique as function of the time of electron cooling (Fig. 4.2). The relative populations of $v=0$ (circles), $v=1$ (squares) and the sum of all other contributions, $v \geq 2$ (triangles) are shown. The broken lines represent the evolution of the vibrational population based on a model assuming only the DR reaction (Eq. 2.1) to be active applying the rate coefficients presented in Tab. 4.2. The full lines represent a model including also SEC (Eq. 2.7) with a rate coefficient of $\alpha_{SEC} = 1.8 \cdot 10^{-7} \text{ cm}^3 \text{ s}^{-1}$.

The higher vibrational levels ($v \geq 2$) recombine about 60 times faster than the ground state – values between 25 and 250 are allowed by the statistical errors. One has to keep in mind that the found rate coefficients are averaging over a rotational distribution within the vibrational level, which may change over the time of 50 s of the underlying measurements. In Sec. 4.3.3 we will show evidence for slow changes in the rotational populations during long electron cooling in ${}^3\text{He}^4\text{He}^+$.

With the obtained initial state specific DR rate coefficient α_{DR}^v one can try to determine whether the vibrational deexcitation is mainly a result of a recombination rate driven depletion of the fast recombining excited states or if super-elastic collisions need to be included to account for the observed evolution of the vibrational population. To this end a simple model was developed to describe the time-dependence of the vibrational population distribution of the ${}^4\text{He}_2^+$ ions that are subject to DR and SEC reactions.

If one assumes that the vibrational population is depleted only through the occurrence of DR, then the time dependence of the number of molecular ions in a given vibrational state N_v is

described by the following differential equation:

$$\dot{N}_v = -\tilde{\alpha}_{DR}^v(0 \text{ eV}) \cdot \eta \cdot n_e \cdot N_v \quad (4.15)$$

where n_e is the electron density at $E_d=0$ eV and $\eta=l/L$ with l being the electron cooler length, L the TSR circumference.

In order to compare this time dependence to our measured data, we used the time dependence of the vibrational population observed with CEI as shown in Fig. 4.2. Applying $n_e=1.1 \cdot 10^7 \text{ cm}^{-3}$ like it was used in the experiment, the evolution of the vibrational populations can be modeled, starting with the vibrational distribution measured after 5 s. The $\tilde{\alpha}_{DR}^v$ that are given in Table 4.2 are used as the DR rate coefficients. The evolution of the vibrational population that is calculated in this model is given by the broken curves in Fig. 4.8. Clearly this simplified model fails to explain the observed evolution: After 50 s, the model predicts approximately equal amounts of molecular ions in $v=0$ and $v=1$ while the experimental results showed that the excited states had almost completely vanished. This is no surprise given the DR rate coefficient found for the $v=1$ state. Under these conditions, the average reaction rate is approximately $n_e \cdot l/L \cdot \alpha_{DR}^{v=1}(0 \text{ eV}) \approx 1/1000 \text{ s}^{-1}$, i. e. the average time until a reaction is about 1000 seconds for ions in $v=1$.

A much faster process is needed to explain the observed evolution. In order to expand the model given by Eq. 4.15 so that it includes SEC processes an additional term needs to be added to the right hand side of the equation. This term describes the transfer of molecular ions from one vibrational state to another. For simplification, we assume that the vibrational excitation changes stepwise in the SEC processes – for an ion initially in the $v \geq 2$ -fraction of the beam it yields an ion in the $v=1$ level, and an ion with $v=1$ is moved into the vibrational ground state. With these assumptions, Eq. 4.15 is transformed to:

$$\dot{N}_v = -\tilde{\alpha}_{DR}^v(0 \text{ eV}) \cdot \eta \cdot n_e \cdot N_v - \alpha_{SEC} \cdot \eta \cdot n_e \cdot N_v + \alpha_{SEC} \cdot \eta \cdot n_e \cdot N_{v+1} \quad (4.16)$$

In the above equation, it is also assumed that all SEC rate coefficients α_{SEC} are independent of the vibrational state, which is clearly an over-simplification. Nevertheless, with a choice of $\alpha_{SEC}=1.8 \cdot 10^{-7} \text{ cm}^3 \text{ s}^{-1}$ one can obtain a good representation of the vibrational state evolution which is shown by the full curves in Fig. 4.8. This high SEC rate coefficient for the $v=1$ level compared to the low DR rate coefficient can be understood, if the vibronic couplings within the bound electronic state [NTN87, Sch06] are much stronger than the electronic couplings expressed by the Franck-Condon overlap driving direct process DR. The vibronic couplings depend on non-constant quantum defects. It means that the vibrational SEC happens mainly via non-adiabatic couplings, comparable to the DR of H_3^+ .

The observed strong decrease of the DR rate coefficient of $^4\text{He}_2^+$ as a function of the electron cooling time therefore is the result of the immense dependence of the DR rate coefficient on the initial vibrational state (Tab. 4.2) in combination with the strong time dependence of the vibrational population distribution caused by SEC reactions with a rate coefficient in the order of $\alpha_{SEC}=1.8\cdot 10^{-7}\text{cm}^3\text{s}^{-1}$. The SEC process is especially needed to explain the evolution of the ratio of population between the $v=0$ and $v=1$ vibrational levels, that were found to recombine very slowly at $\alpha_{DR}^{v=0}\leq 5\cdot 10^{-9}\text{cm}^3\text{s}^{-1}$ and $\alpha_{DR}^{v=1}\leq 2.1\cdot 10^{-8}\text{cm}^3\text{s}^{-1}$. These values are only upper limits, the precise determination of a rate coefficient for the slow recombining states is very difficult with this method because it is not obvious which proportion of the total DR signal stems from which vibrational level. Even a small fraction ($\sim 1\%$) of highly excited He_2^+ ions remaining in the stored ion beam can increase the observed DR rate coefficient by 60 % or more based on the values found here. The identification of the initial vibrational level can be done by 2d-imaging measurements of the DR process, but such imaging data was not yet available for the $^4\text{He}^+$ DR.

The DR rate coefficient that was calculated by Carata [COS99] for the ($v=0, J=0$) level of $^3\text{He}^4\text{He}^+$ is $\alpha_{DR}(0.026\text{ eV})\approx 10^{-11}\text{cm}^3\text{s}^{-1}$ and the rate coefficient for $^4\text{He}_2^+$ is at least a factor of two lower than that, as can be read of Figs. 10 and 11 in that work. The rate coefficient observed for the $^3\text{He}^4\text{He}^+$ DR of the vibrational ground state at the TSR [PBA⁺05] is $\alpha_{DR}^{v=0}=7.3(2.1)\cdot 10^{-10}\text{cm}^3\text{s}^{-1}$. Here the DR imaging technique (Sec. 3.3.2) was used to identify the initial vibrational states in the observed DR events.

4.3.3 Time dependent DR rate coefficient of $^3\text{He}^4\text{He}^+$ at 0 eV – rotational SEC

The DR rate coefficient at $E_d=0$ eV as a function of time for $^3\text{He}^4\text{He}^+$ was measured with $E_i=7.28$ MeV and for both $n_e=1.2\cdot 10^7\text{cm}^{-3}$ (Fig. 4.9, [PBA⁺05]). The rate coefficient decreases very fast, until an asymptotic value is reached after approximately 20 s (black circles). The evolution of the DR rate coefficient up to a time of 20 s after the injection cannot be based on changes in the vibrational populations. Radiative deexcitation as the fastest process influencing the vibrational population defines the time scale of this to be in the order of 1 s, which was also observed in the CEI measurements (Sec. 4.1.1). So the evolution of the DR rate coefficient observed over the 20 s is due to changes in the rotational excitation.

The time scale is probably shorter than it would be, if radiative deexcitation would govern this effect. The radiative lifetime of rotational levels in the vibrational ground state are 10 s and above for $J\leq 10$ [PBA⁺05]. To test this, the ion beam was phase space cooled for 5 s under the same conditions as in the black curve. Then the electron beam was switched off for a variable time and switched back on after 10, 20, 35 or 45 s and the DR rate coefficient was measured

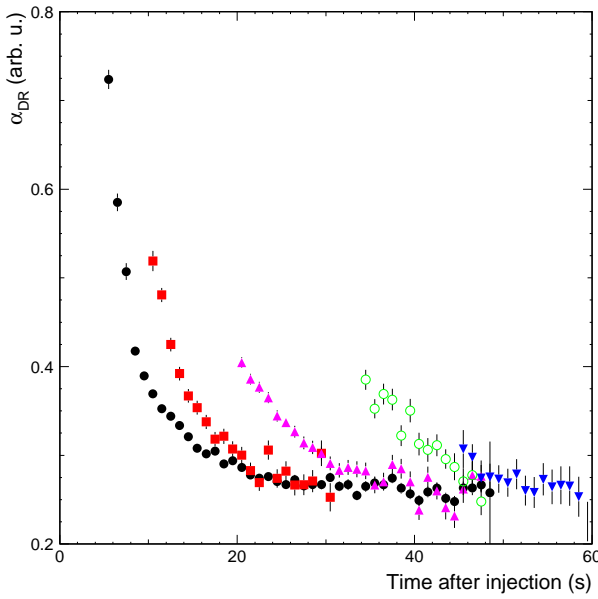


Fig. 4.9: The relative DR rate coefficient of ${}^3\text{He}^4\text{He}^+$ $\alpha_{DR}(0 \text{ eV})$ as a function of time for $E_i=7.28 \text{ MeV}$ and $n_e=1.2 \cdot 10^7 \text{ cm}^{-3}$ [PBA⁺05]. The electron beam was switched off for a variable time after 5 s of phase space cooling. The black circles show the rate coefficient with constant electron beam. Red squares: switch electrons on after 10 s. Purple triangles: after 20 s. Green open circles: after 35 s. Blue triangles: after 45 s.

again at 0 eV. The results are shown with coloured markers in Fig. 4.9. The DR rate coefficients measured immediately after switching back on the electron beam decreases from 10 s to 45 s time of switch-on, beyond the time of 20 s. However, it is significantly higher than the rate coefficient with constant electron beam.

It was demonstrated by detailed modeling of all processes [PBA⁺05] that this temporal evolution of the DR rate coefficient can be explained well by assuming a constant rotational SEC cross section in the order of 10^{-12} cm^2 . Other models, assuming excitation of vibrational levels by inelastic collisions in which radiative deexcitation of rotational levels works faster yield much higher populations of vibrationally excited levels than were observed in the experiments [PBA⁺05].

4.4 Rovibrational excitation by electron collisions

Electron-molecular ion collisions do not only induce deexcitation, but they can also internally excite the molecular collision partner through inelastic collision (Eq. 2.7), if the incoming electron has sufficient energy. This might have an important effect, since the additional collision energies in the toroidal sections are above the levels of the rotational and vibrational spacings, reaching energies of several eV, so that even if the detuning energy between electron and ion beam is set to $E_d=0 \text{ eV}$, electrons with sufficient energy are available for such a process. In addition, the time that is spent with the electron beam set to $E_d=E_d^{ref}$ yields a large amount of electrons with sufficient energy.

An experiment designed to search for this effect was performed at an ion beam energy of

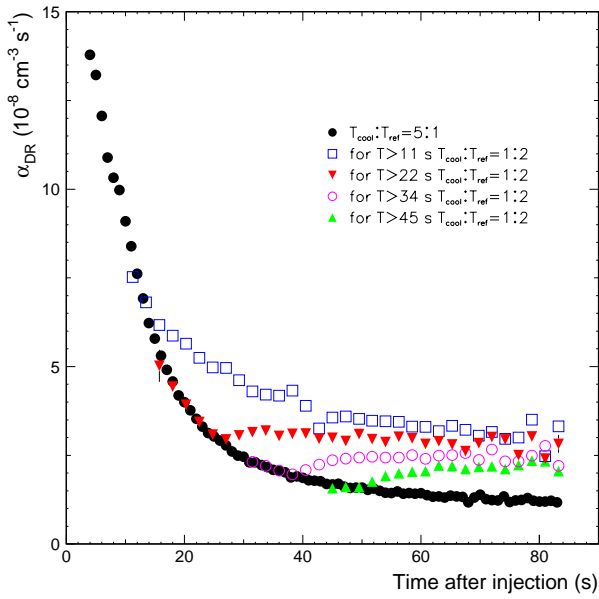


Fig. 4.10: Electron induced variation of the absolute DR rate coefficient at $E_d=0$ eV as a function of storage time. Filled circles: constant dwell time ratio of $T_c:T_r:T_m=5:1:0$. Others: the dwell time ratio is initially set to $T_c:T_r:T_m=5:1:0$ and then changed to $T_c:T_r:T_m=1:2:0$ after a given time (see legend). All measurements were made at $E_i=3.83$ MeV and $n_e=5.3 \cdot 10^6 \text{ cm}^{-3}$ at cooling energy.

$E_i=3.83$ MeV and $n_e=5.3 \cdot 10^6 \text{ cm}^{-3}$ at cooling energy like in the observation of $\tilde{\alpha}_{DR}(0 \text{ eV}, t)$ in Fig. 4.7 represented by the open circles. And like in that measurement, the ratio of dwell times on the cooling and reference energy initially was set to $T_c:T_r:T_m=5:1:0$ in the new measurement. After a storage time of 11, 22, 34 or 45 seconds, respectively, the dwell time ratio was changed abruptly to $T_c:T_r:T_m=1:2:0$, increasing very much the time at the reference energy and reducing at the same time the effect of vibrational cooling via SEC that was found in the previous section.

Fig. 4.10 shows the results of such measurements. The filled black circles show the data with constant $T_c:T_r:T_m=5:1:0$ over the full measurement time (the same as in Fig. 4.7). In the cases when the dwell time ratio is changed after a certain time, $\tilde{\alpha}_{DR}(0 \text{ eV}, t)$ shows a different behaviour and approaches a higher, asymptotic level that appears to be independent of the time at which the dwell time ratio was changed.

The fact that a steady state DR rate coefficient depends on the dwell time ratio $T_c:T_r:T_m$ shows directly, that some process works against the deexcitation via SEC, in the sense that this process moves molecular ions to states that recombine faster which in the $^4\text{He}_2^+$ system are higher vibrational states. In order to see, if there really is an electron-induced mechanism, or if the excitation is caused by collisions with residual gas atoms and the reduction of SEC at $E_d=0$ eV due to the smaller dwell time ratio at the cooling energy, a variation of above experiment was done:

At an ion beam energy $E_i=8.32$ MeV the ion beam was cooled for 54 seconds applying $T_c:T_r:T_m=1:0:0$, then the dwell time ratio was changed to $T_c:T_r:T_m=1:1:4$ with $E_d^m=0-32$ eV. In this experiment, the measurement dwell time T_m can also be considered as an excitation

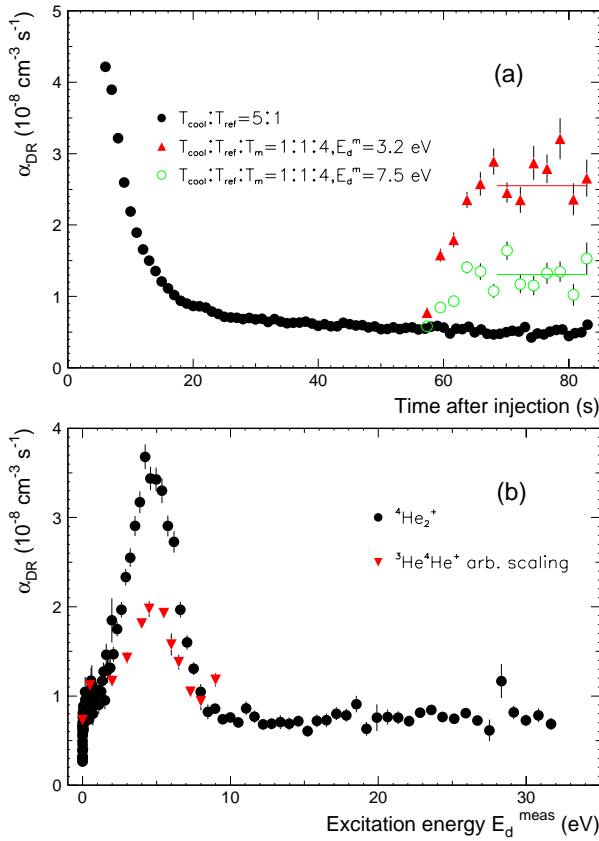


Fig. 4.11: Electron induced variation of the absolute DR rate coefficient at $E_d=0 \text{ eV}$ as a function of storage time and detuning energy of the exciting electrons. All measurements were made at $E_i=8.32 \text{ MeV}$ and $n_e=1.1 \cdot 10^7 \text{ cm}^{-3}$ at cooling energy, $E_d^{\text{ref}}=23.5 \text{ eV}$.

(a) Electron induced variation of the absolute DR rate coefficient at $E_d=0 \text{ eV}$ as a function of storage time for 2 representative excitation energies E_d^{meas} . Filled circles: constant dwell time ratio of $T_c:T_r:T_m=5:1:0$ (Fig. 4.7). Others: the dwell time ratio is initially set to $T_c:T_r:T_m=1:0:0$ and then changed to $T_c:T_r:T_m=1:1:4$ after 54 s. The lines show the average $\alpha_{DR}(0 \text{ eV})$ between 65 and 85 s.

(b) Excitation of DR rate at $E_d=0 \text{ eV}$ as function of excitation energy E_d^{meas} . Circles: For ${}^4\text{He}_2^+$, average DR rate over 65 to 85 s obtained as for figure (a) Triangles: Excitation profile of ${}^3\text{He}^4\text{He}^+$ [PBA⁺05], scaled to comparable height at 8 eV.

time at the energy E_d^m . The long time of cooling before changing the dwell time ratio allows to start with a ${}^4\text{He}_2^+$ beam that is vibrationally very well cooled (Fig. 4.2) and thus its DR rate coefficient at $E_d=0 \text{ eV}$ very sensitive to changes in the internal excitation.

Fig. 4.11(a) shows the DR rate coefficient $\tilde{\alpha}_{DR}(0 \text{ eV}, t)$ as function of time. Two different excitation energies, namely $E_d^{\text{meas}}=3.2$ and 7.5 eV are shown. Beginning with the excitation at 54 s after injection a distinct rise to a new constant level is observed, clearly depending on the value of E_d^{meas} . At all excitation energy values, an asymptotic level was reached at 68 s after injection. For comparison the filled circles show the result with a constant $T_c:T_r:T_m=5:1:0$ as in Fig. 4.7.

Fig. 4.11(b) shows the value of the asymptotic levels reached after excitation in this way as a function of E_d^{meas} in the measured range of 0–32 eV. A broad structure is found in the range from 0 to 8 eV, peaking at $E_d^{\text{meas}} \approx 4.5 \text{ eV}$. The maximum value is approximately $3.5 \cdot 10^{-8} \text{ cm}^3 \text{ s}^{-1}$, about 7 times the minimum value at constant intense cooling. For excitation energies above 8 eV, no further structure is observed, and the rate coefficient $\tilde{\alpha}_{DR}(0 \text{ eV})$ that is reached is only slightly above the value at intense cooling ($5 \cdot 10^{-9} \text{ cm}^3 \text{ s}^{-1}$) independent of the excitation energy. From this we conclude, that electrons with kinetic energies of few eV are able to excite stored

$^4\text{He}_2^+$ molecular ions in a time scale of about 10 s. For comparison, data previously obtained for $^3\text{He}^4\text{He}^+$ applying a different method [PBA⁺05] is also shown. This method is based on the observation, that only DR from vibrationally excited He_2^+ with $v \geq 3$ can access the fragment final states with one ground state atom and one atom in a state with principal quantum number $n=3$ (Fig. 2.5). With 2d-imaging, it is possible to determine the fraction of DR events stemming from molecules in vibrational levels above and below $v=3$. This data in Fig. 4.11(b) is scaled to a comparable level at excitation energies outside of the peak. Because of the different methods and the radiative deexcitation in the heteronuclear system, a comparison even on a relative strength of the excitation process in the two systems is not possible.

4.5 Rovibrational excitation by residual gas collisions

Destructive collisions between the stored ion beam and the residual gas in the TSR are observed on the neutral fragment detectors as shown in Figs. 4.4 (a) and (b) in the phases without electron beam. These processes are residual gas induced dissociative excitation (Eq. 2.9) and dissociative charge exchange (Eq. 2.10). Residual gas DE is expected to be independent of the internal excitation of the molecular ion, and DC appeared to be of very low rate, much lower than electron-induced DR, so that it cannot have a visible effect on the population distribution of rovibrationally excited states. Non-destructive reactions occurring in the collision of the MeV molecular ions with the residual gas species can lead to excitation or deexcitation (Eq. 2.11) of the stored ions, however.

The observation of the vibrational level populations with the CEI technique while the stored molecules were not electron cooled (Fig. 4.3) showed only very slow reexcitation. But because of the strong dependence of the DR rate coefficient of the $^4\text{He}_2^+$ on the vibrational excitation at small collision energy, a DR measurement under similar conditions is much more sensitive. One should keep in mind, that there is no radiative excitation or deexcitation in this homonuclear system, so without electrons present, collisions with the residual gas are the only processes that can influence the internal excitation of the stored molecular ions.

To investigate the effect of collisions with the residual gas, a $^4\text{He}_2^+$ beam at $E_i=8.32$ MeV was first electron cooled ($T_c:T_r:T_m=5:1:0$) for 22.5 s, i. e. there were the same conditions as represented by the lower curve in Fig. 4.7. Then the electron beam was switched off completely for a certain, variable time. After that time the electron beam was switched back on, and the DR rate coefficient was measured with $T_c:T_r:T_m=5:1:0$. The observed DR rate coefficients are plotted in Fig. 4.12 with the coloured markers. The black curve in the figure is the same as in Fig. 4.3 and, for times smaller than 22.5 s, it shows $\tilde{\alpha}_{DR}(0 \text{ eV})$ in this measurement. From

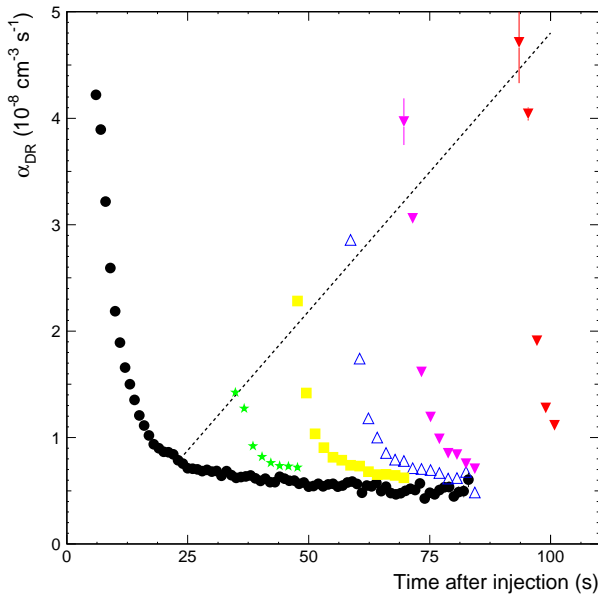


Fig. 4.12: The effect of ion-residual gas collisions on the DR rate coefficient of the stored ${}^4\text{He}_2^+$ ions. After 22.5 s of electron cooling, the beam was switched off ($E_i=8.32$ MeV). The filled circles show $\tilde{\alpha}_{DR}(0$ eV) for continuous electron cooling ($T_c:T_r:T_m=5:1:0$) (as in Fig. 4.7), while the other markers present $\tilde{\alpha}_{DR}(0$ eV) after switching off the electron beam for 11, 22.5, 34, 45 or 67.5 s and then switching it back on. The dashed line starting at 22.5 seconds is meant to guide the eye along the onset points for the individual measurements. The data compares to the vibrational populations given in Fig. 4.3.

the injection, the rate coefficient decreases strongly until the electron beam is switched off and no DR can be observed. When the electron beam is switched back on 11 s later, the DR rate coefficient is measured to have increased by almost a factor of 2 (green stars). Once the electron beam is on, $\tilde{\alpha}_{DR}(0$ eV) decreases very fast again until it reaches the same asymptotic value as the curve with constant electron beam. After 45 s of pause in the electron cooling, $\tilde{\alpha}_{DR}(0$ eV) is about equal to the initial rate coefficient after 5 s. In good approximation, the increase of the DR rate coefficient is proportional to the time spent without electron cooling for times without electron cooling less than 70 s. This is illustrated by the dashed line that follows the onset points of the measured DR rate coefficients after the 'switch-off' time. The fact that there is no sign of an asymptotic value being reached shows that not a large part of the stored ions gets excited, in agreement with the findings of the direct observation of the vibrational level populations in Fig. 4.3. It also underlines again the very strong dependence of $\tilde{\alpha}_{DR}(0$ eV) on the vibrational excitation present.

A similar result was found also in the ${}^3\text{He}{}^4\text{He}^+$, where the excitation or rather the maintained population of excited vibrational levels was observed using 2d-imaging [PBA⁺05], in the same way as described for the excitation by electron collisions in Sec. 4.4. There it was concluded, that collisions with residual gas are the most important factor responsible for a population of excited vibrational levels ($v \geq 3$) that is higher than the thermal distribution.

So in both He_2^+ systems the influence of the residual gas collisions on the vibrational excitation was observed.

4.6 Energy dependent DR rate coefficients of He_2^+

The energy dependence of the DR rate coefficient was measured with the electron cooler with the method described in Sec. 3.3.3 for $^4\text{He}_2^+$ and $^3\text{He}^4\text{He}^+$ under various experimental conditions. The conditions that varied were storage time t , electron density n_e , ion beam energy E_i and reference energy E_d^{ref} . Having found a strong time dependence of $\alpha_{DR}(0 \text{ eV})$ for both species of He_2^+ under investigation, we expect to find it in the rate coefficient as a function of energy, too.

4.6.1 Time dependence of $\alpha_{DR}(E_d)$ in $^4\text{He}_2^+$

In a DR measurement of $^4\text{He}_2^+$ at $E_i=3.83 \text{ MeV}$ and an electron density $n_e=5.3 \cdot 10^6 \text{ cm}^{-3}$ the rate coefficient as function of energy was obtained after different times of intense electron cooling with $T_c:T_r:T_m=1:0:0$. After the cooling the relative rate coefficient was measured using $T_c:T_r:T_m=1:1:4$. In Fig. 4.13. the DR cross section (for easier comparison with the previous data obtained at ASTRID (Fig. 2.6)) and the DR rate coefficient after 4 different times of electron cooling are shown. In addition, $\alpha_{DR}(E_d)$ as it was measured with $n_e=1.1 \cdot 10^7 \text{ cm}^{-3}$ at $E_i=8.32 \text{ MeV}$ after 58.5 s is plotted. This set was subject to the strongest electron cooling. At all times, $\alpha_{DR}(E_d)$ decreases when E_d is increased from 0 eV to 0.7–1.0 eV where there is a minimum. No structure is visible in this range. $\alpha_{DR}(E_d)$ increases again when the detuning energy is increased until a peak at about 7 eV is reached. From there the rate coefficient drops again to almost zero at $E_d \approx 15 \text{ eV}$, before more structures appear up to 35 eV, which is better visible in Fig. 4.14(b).

In Fig. 4.13 one finds a strong time dependence, with a decrease of the observed rate coefficient with time of electron cooling. The lower the detuning energy is, the stronger is the reduction. For detuning energies that are higher than the energy of the peak at 7 eV, no change with time is observed. By far the lowest rate coefficient in the low energy region was measured with the high electron density ($n_e=1.1 \cdot 10^7 \text{ cm}^{-3}$) after long electron cooling. This agrees with the finding in Fig. 4.7 that $\alpha_{DR}(0 \text{ eV})$ was measured to be considerably lower with more intense electron cooling.

Finding such a strong time dependence in the DR of $^4\text{He}^+$ is in contrast to the experimental results at ASTRID [UDS⁺05], where no time dependence at all was observed. Also the shape of the cross section (Fig. 2.6 vs. Fig. 4.13) is very different. There is no structure visible in the DR cross section for $E_d=0-7 \text{ eV}$ in the ASTRID data. In the TSR data, one can see that this structure becomes more and more distinct with time. From that one can assume that it is washed out in the early phases of the measurement at the TSR, when the ion sample is still

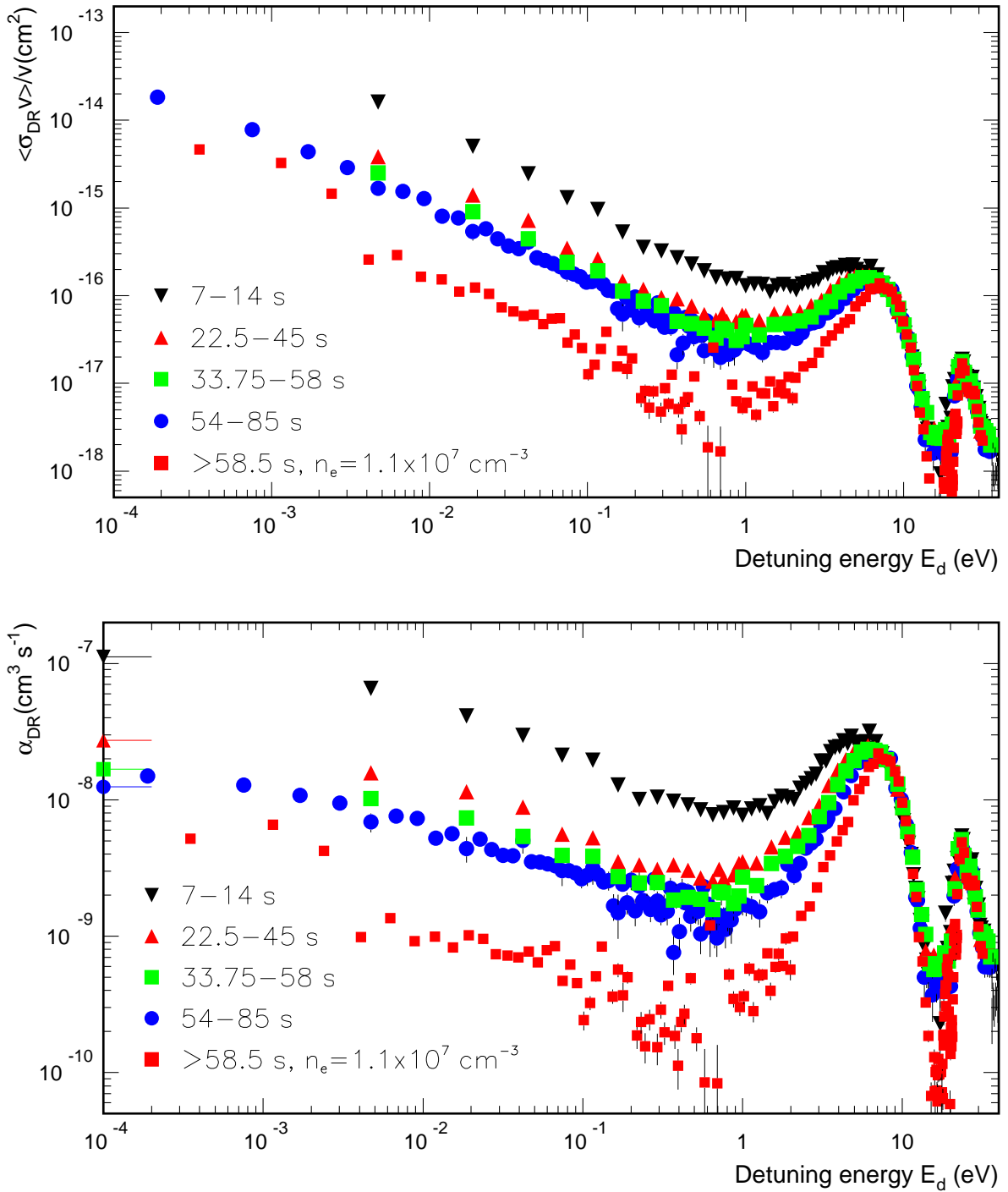


Fig. 4.13: The absolute DR rate coefficient of ${}^4\text{He}_2^+$ as function of energy that was measured at the TSR after various times of electron cooling with $n_e = 5.3 \cdot 10^6 \text{ cm}^{-3}$ at $E_i = 3.83 \text{ MeV}$ and for $n_e = 1.1 \cdot 10^7 \text{ cm}^{-3}$ at $E_i = 8.32 \text{ MeV}$.

partly vibrationally excited, and it becomes visible when the vibrational cooling to the $v=0$ level proceeds. Calculations by Royal *et al.* [RO05] of the DR cross section for vibrationally excited levels of He_2^+ show peaks at lower energies than for the ground state, i. e. far below 7 eV, supporting this view.

So the comparison of the results from TSR and ASTRID can be well interpreted, if one assumes that the $^4\text{He}_2^+$ ions in the ASTRID experiment carried considerable vibrational excitation. We know that collisions with residual gas can efficiently excite vibrations in $^4\text{He}_2^+$ (Sec. 4.4) and Urbain reports a relatively high residual gas pressure in the ASTRID storage ring leading to a very short beam life time of 2.5 s comparing to 10 to 15 s at the TSR. In addition the electron temperature of the ASTRID electron beam was higher ($k_B T_{\perp}=22$ meV compared to 10 meV at the TSR electron cooler), possibly reducing the efficiency of vibrational SEC that was found to be responsible for the deexcitation in the TSR measurements (Sec. 4.3.2). The electron density was comparable with $n_e=7.9\cdot 10^6\text{cm}^{-3}$ at ASTRID and $n_e=5.5\cdot 10^6\text{cm}^{-3}$ or $n_e=1.1\cdot 10^7\text{cm}^{-3}$ at the TSR. So it is likely that the combined effects of more residual gas collisions and less SEC yielded a stored ion sample with more vibrational excitation at ASTRID.

4.6.2 High energy structures in the DR rate coefficient of He_2^+

The measured shape of the DR cross section of $^4\text{He}_2^+$ (Fig. 4.13) is similar to that of $^3\text{He}^4\text{He}^+$ from the ASTRID measurement (Fig. 2.6). How similar the rate coefficients of the two isotopomers are can be seen in Fig. 4.14. The absolute DR rate coefficients as function of energy that were measured for vibrationally cold samples at the TSR are compared over the range of $E_d=1\text{--}40$ eV. The absolute normalization of the $^4\text{He}_2^+$ DR rate coefficient was obtained in Sec. 4.2.2.

For $^4\text{He}_2^+$ the broad peak around 7.5 eV is extended by approximately 0.5–1 eV to lower energies for less electron cooling compared to the data for more intense electron cooling. This probably indicates that there was some vibrational excitation left in the ion sample for the set with less electron cooling. The peak is about 10 % higher and sharper for $^3\text{He}^4\text{He}^+$ and the maximum is between the maxima of the two sets of the homonuclear species. Compared to the calculations by Royal *et al.* [RO05] the agreement in shape, position and height ratio between the isotopomers is good, but the absolute value deviates by about a factor 2.5.

The peak at 7.5 eV is due to capture into doubly excited states converging to the first excited electronic state of the molecular ion [RO05]. The structures between $E_d=15$ and 40 eV agree extremely well in the three data sets presented, even in absolute value. At least four individual peaks can be identified in this range, at $E_d=19$, 21, 23.5 and 27.5 eV. Two of the peaks are wide, the one at $E_d=23.5$ eV and the one at $E_d=27.5$ eV, while the other two are very narrow,

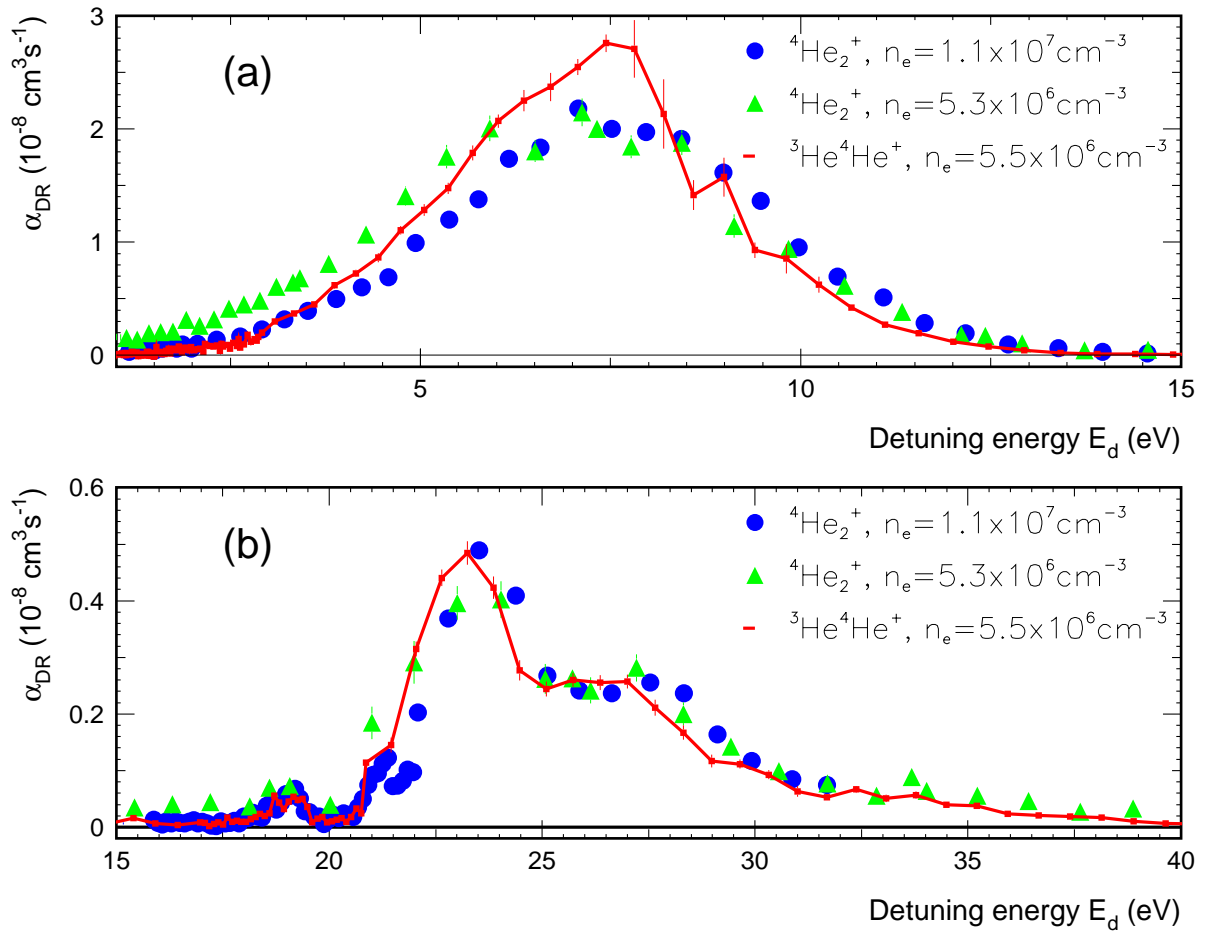


Fig. 4.14: The absolute DR rate coefficient of ${}^3\text{He}^4\text{He}^+$ and ${}^4\text{He}_2^+$ as function of energy that was measured at the TSR after long electron cooling. Red line: ${}^3\text{He}^4\text{He}^+$ with $n_e=5.5 \cdot 10^6 \text{ cm}^{-3}$ at $E_i=7.28 \text{ MeV}$ after 35 s [PBA⁺05]. Blue circles: ${}^4\text{He}_2^+$ with $n_e=1.1 \cdot 10^7 \text{ cm}^{-3}$ at $E_i=8.32 \text{ MeV}$ after 58.5 s. Green triangles: ${}^4\text{He}_2^+$ with $n_e=5.3 \cdot 10^6 \text{ cm}^{-3}$ at $E_i=3.83 \text{ MeV}$ after 54 s. (a) In the range of $E_d=1\text{--}15 \text{ eV}$. (b) In the range of $E_d=15\text{--}40 \text{ eV}$.

about 1 eV in widths. These are approximately the energies that separate the electronic ground state of He_2^+ from several high lying ion states that in turn have series of neutral Rydberg states below them. Fig. 4.15 shows the resonance energies measured from the electronic ground state and a couple of the ionic and neutral states in this high-energy range. No calculations on the DR rate coefficient of He_2^+ at these energies are available to compare to. It seems interesting to find out which atomic limits are reached in the DR at these energies. Energetically, the $\text{He}(1s2l)+\text{He}(1s2l)$ could be reached.

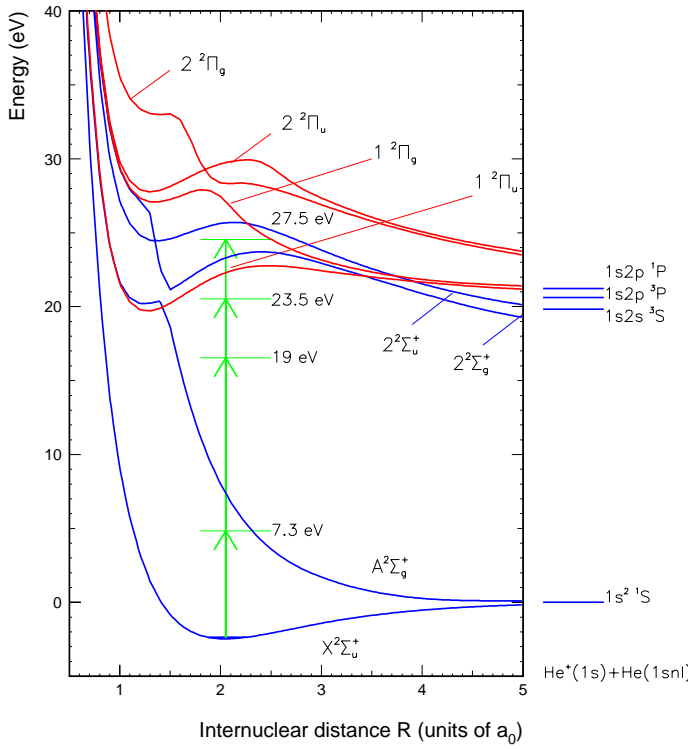


Fig. 4.15: Potential energy curves in the $\text{He}_2/\text{He}_2^+$ -system. Blue: He_2^+ electronic ground state and the lowest excited electronic states [CR95, AH91] with the lowest vibrational levels shown as horizontal lines. Red: Some neutral potential curves [AH91] in the range of about 20 to 30 eV above the ground state of He_2^+ . The horizontal lines on the right mark the energies of the atomic limits of the ionic states. The green arrows indicate energies above the ground state of He_2^+ , where structures in the DR were observed.

4.7 Summary

A strong time dependence of the DR rate coefficient at 0 eV (Secs. 4.3.1 and 4.3.3) and of the vibrational populations (Sec. 4.1) was observed in both species, $^3\text{He}^4\text{He}^+$ and $^4\text{He}_2^+$, but on different time scales. The difference in the time scales is a result of the different processes dominating the evolution of the vibrational populations: Very fast radiative deexcitation in $^3\text{He}^4\text{He}^+$ within 2 s compared to electron interactions, which occur in both, taking tens of seconds. In both cases, the finally reached vibrational distribution was dominated by the ground state $v=0$. The absolute DR rate coefficients were obtained for heteronuclear and homonuclear species with the same method, amounting to $2.4(5)\cdot 10^{-8}$ and $2.0(4)\cdot 10^{-8}\text{cm}^3\text{s}^{-1}$, respectively, at a collision energy of $E_d=7.4$ eV (Sec. 4.2). The value observed for $^3\text{He}^4\text{He}^+$ is in agreement with the previously measured value of $2.8(4)\cdot 10^{-8}\text{cm}^3\text{s}^{-1}$ and considerably higher than the results from another storage ring [UDS⁺05] and of the theoretical model [RO05].

Absolute rate coefficients at 0 eV were obtained for the vibrational ground state ($\alpha_{DR}^{v=0}(0\text{ eV})=3(2)\cdot 10^{-9}\text{cm}^3\text{s}^{-1}$) of $^4\text{He}_2^+$ and for the $v=1$ state ($\alpha_{DR}^{v=1}(0\text{ eV})\leq 2.1\cdot 10^{-8}\text{cm}^3\text{s}^{-1}$). For levels with $v\geq 2$ a rate coefficient of $\alpha_{DR}^{v\geq 2}(0\text{ eV})=2.0_{-0.6}^{+1.5}\cdot 10^{-7}\text{cm}^3\text{s}^{-1}$ was obtained as an average value for these states in Sec. 4.3.2. Applying these rate coefficients to a simple model calculation and comparing with the time dependence of the vibrational population (Sec. 4.1.2) a vibrational SEC rate coefficient $\alpha_{SEC}^{v=1}=1.8\cdot 10^{-7}\text{cm}^3\text{s}^{-1}$ of the $v=1$ state was needed to explain

the observed data.

Inelastic collisions with electrons of a few eV were shown to excite He_2^+ vibrationally (Sec. 4.4). A distinct energy dependence was observed, with a maximum at approximately $E_d=4.5$ eV, similar for both isotopomers. This peak lies lower than the maximum rate coefficient observed for the DR, which is at about 7.3 eV. Rovibrational excitation by residual gas collisions was also observed (Sec. 4.5), thanks to the high sensitivity of the DR rate coefficient for vibrational excitation.

The energy dependent DR rate coefficient of $^4\text{He}_2^+$ was measured after several times of electron cooling, showing a strong time dependence (Sec. 4.6.1). Comparison of cold $^4\text{He}_2^+$ with $^3\text{He}^4\text{He}^+$ data [PBA⁺05] shows almost identical structures in the region of $E_d=1-40$ eV (Sec. 4.6.2). This means the very different DR cross sections measured at ASTRID ([UDS⁺05] and Fig. 2.6) for $^4\text{He}_2^+$ and $^3\text{He}^4\text{He}^+$ can be explained, if one assumes that the $^4\text{He}_2^+$ was measured at a very high vibrational temperature. The peaks at 7.5 eV measured at the TSR agree in shape with the $^3\text{He}^4\text{He}^+$ measurements at ASTRID and with calculations by Royal and Orel [RO05, OR06], but the absolute scale is different (see above). Further structures in the range of $E_d=19-30$ eV were found and neutral and ionic states connected to atomic limits with two excited He-atoms or excited He-atom + He-ion were shown to be accessible in this energy region. Here calculations from the theoretical side are needed for comparison.

5. Rotational resonances in the recombination of HD^+

This chapter addresses the results of high energy resolution DR rate coefficient measurements using the electron target (Sec. 3.4.1). The electron beams were provided by the thermal cathode and by the ultra-cold photocathode, respectively. The main experimental conditions are summarized in Tab. 5.1.

In this chapter, we will describe the advantages of using two electron cooling devices at the same time and discuss the improvements in energy resolution made possible by the new setup by comparing to previous DR rate coefficient measurements. The high energy resolution triggers the search for time dependence in the rate coefficient. The results of a MQDT calculation is compared to the experimental results as a whole and on the level of single rotational initial states.

	E_i [MeV]	$n_{e,t}$ [10^6cm^{-3}]	kT_{\perp} [meV]	kT_{\parallel} [μeV]	$n_{e,c}$ [10^6cm^{-3}]
thermal cathode	1.4	2.85	2.8	45	5.5
photocathode	5.3	0.32	0.6	25	18

Tab. 5.1: Table of experimental conditions in the HD^+ measurements with the electron target: Ion beam energy, electron density of the electron target beam, transversal and longitudinal temperature of the electron beams and electron density in the electron cooler.

5.1 Measurements with two electron beam devices

5.1.1 Ion beam dragging with one and two electron beams

With the electron target and electron cooler at the TSR a new scheme of measurements is possible for electron-ion collisions. It is possible to use two electron beams at the same time. This solves one major problem of the merged-beam experiments in storage rings with one electron

beam device: Defining precisely the ion beam energy E_i with a velocity $v_i=v_{e,c}$ by electron cooling while alternatively using the electron beam as target at another velocity $v_{e,m}$ for measuring (Sec. 3.3.3). If $v_i=v_{e,c}\approx v_{e,m}$, i. e. $E_d\approx 0$ eV (Eq. 3.2), the ions will be efficiently accelerated or decelerated by the collisions with the electrons, resulting in what is called '*beam-dragging*'. If the ion beam velocity is not well defined, the collision or real detuning energy E_d between electrons and ions is not the one that is expected from the electron energy in the laboratory. In the case of dragging, the real collision energy will be smaller than the expected one.

With only one electron beam device the best solution is to switch the electron velocity according to fast cycles, that include sufficient time to maintain the phase space cooling (Sec. 3.3.3). In these phases the electron velocity is set to the same velocity $v_{e,c}$ as in the initial phase space cooling time. In addition, one can try to reduce the dwell time on the measurement velocity $v_{e,m}$ in these cycles so much, that no visible dragging occurs. But it takes a short time (~ 5 ms) for the electron velocity to stabilize on the new value after a jump, during which rates are not recorded. During this time, also the ion beam velocity v_i can be dragged.

This means one can solve the problem of beam dragging to some degree by using fast cycles including phase space cooling, but the effect cannot be avoided completely for very small detuning energies. Measurements at these low energies will therefore always average over a range of smaller values than the intended one.

With two electron beam devices, the effect of ion beam dragging can be very much reduced. Now one can apply one electron beam – that of the electron cooler – to permanently phase space cool the ion beam, in this way pinning down the ion beam velocity. Then the second electron beam – in the new electron target – is used to do the measurements as described in Sec. 3.4.4. The effect of ion beam dragging with two electron cooling devices was thoroughly investigated in the PhD thesis presenting the electron target [Spr04]. In tests using $^{19}\text{F}^{6+}$ at $E_i=46.4$ MeV with an electron density in the electron cooler of $n_{e,c}=2.6\cdot 10^7\text{cm}^{-3}$ the change of the ion beam velocity was monitored as a function of the electron target beam velocity. For an electron density of $n_{e,t}=4.5\cdot 10^6\text{cm}^{-3}$ at the electron target using the thermal cathode a visible change in the ion beam velocity (Schottky noise diagnostics [WAG⁺98]) occurred at a relative velocity $v_{e,c} - v_{e,t}\approx 35\text{ km s}^{-1}$ or $E_d=3.5$ meV [Spr04]. At $v_{e,c}-v_{e,t}\approx 8.6\text{ km s}^{-1}$ or $E_d=0.2$ meV, the average ion beam velocity was in the middle of the two electron beam velocities, i. e. the real detuning energy was only a quarter of the expected value. For a higher electron density of $n_{e,t}=2.2\cdot 10^7\text{cm}^{-3}$ the effects showed already at higher relative velocities and were stronger [Spr04].

The effect of the dragging on the ion beam velocity is visualized in Fig. 5.1 for two equal electron beams with the same longitudinal electron beam temperature $kT_{\parallel}=200\text{ }\mu\text{eV}$, which is

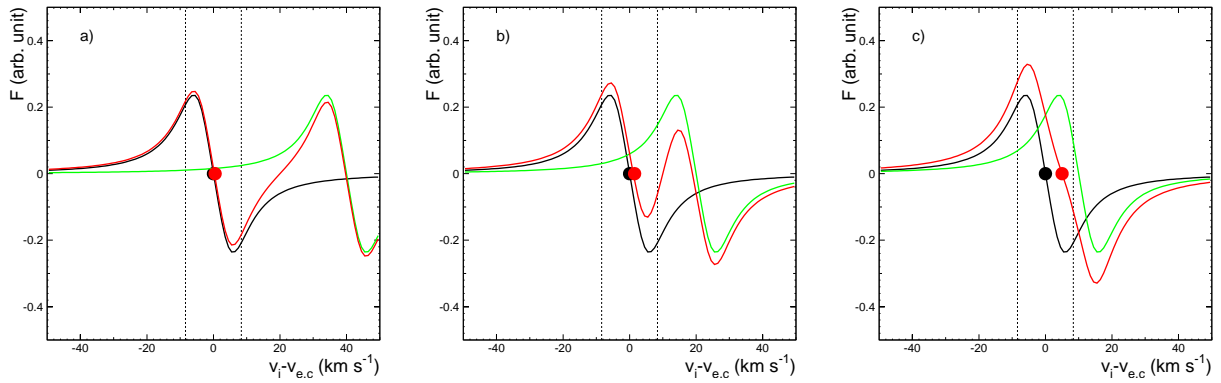


Fig. 5.1: Qualitative visualization of the dragging forces and effect with one and two electron beams. The black line shows the dragging force for one electron beam with velocity $v_{e,c}$ and longitudinal electron beam temperature $kT_{||}=200 \mu\text{eV}$. The black dot marks the equilibrium velocity of the ion beam v_i for this situation. The green line shows the dragging force of a second, equally strong electron beam with a slightly different velocity v_{e2} . The red line shows the sum of the two dragging forces, if they are working at the same time, and the red dot indicates the new equilibrium velocity v_i^{\dagger} that is reached, if the second beam is switched on in addition to the first one. From a) to c), the difference $v_{e2} - v_{e,c}$ is reduced stepwise. The black dashed lines show the thermal electron velocity spread at $kT_{||}$.

of the order of what is delivered in the electron cooler. One finds that the induced shift of the ion beam velocity lies within the thermal electron beam velocity spread (Fig. 5.1(c)). Visible shifts of v_i occur also, if the difference of the electron beam velocities is twice the thermal spread (Fig. 5.1(b)).

The dragging effect, however, can be minimized further by having a very strong electron beam for defining the ion beam velocity and a rather weak probing electron beam. This is almost automatically realized in measurements using the target with the photocathode. The densities of the electron cooler beam then is $\sim 1 \cdot 10^7 \text{cm}^{-3}$ while it is only $\sim 3 \cdot 10^5 \text{cm}^{-3}$ in the electron beam from the photocathode. We hence conclude that the ion velocity changes induced by the dragging influence the center of mass energy by a negligible amount ($\sim 0.3 \text{meV}$) for $E_d \geq 0.5 \text{meV}$. In measurements with the electron cooler alone, center of mass energies in the range of a few meV were affected by the dragging effect significantly in many cases.

5.1.2 Stability of the relative electron beam velocity

Another new problem with two electron beam devices operating at different and independent laboratory energies is that two power supplies are involved to deliver the respective acceleration voltages and that these need to be stabilized, especially with respect to each other. With only one device and one power supply, long time instability of the acceleration voltage only affects the detuning energy very little, because ion beam velocity ($v_i = v_e^{cool}$) and electron velocity at

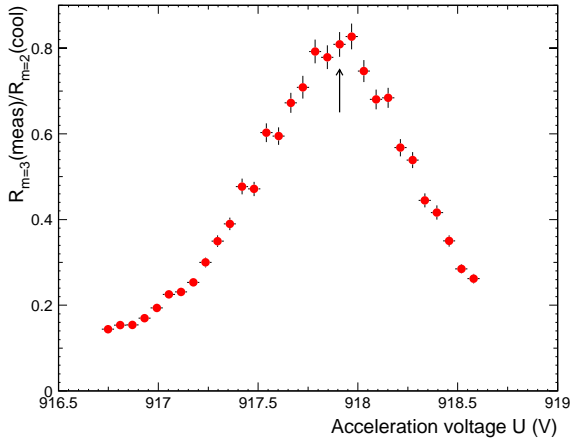


Fig. 5.2: Measurement of the relative HD^+ DR rate around the maximum at 0 eV using the electron target with the LN_2 -cooled photocathode (at $E_i=5.3$ MeV) in the scheme at the end of each injection as described in Sec. 3.4.4. The vertical arrow marks the peak, which corresponds to 0 eV, and the electron beam current and voltage measured are used for the calculation of electron beam velocity and density after taking into account the space charge correction [Pot90].

measurement v_e^{meas} vary in a correlated way and in the same direction. If the electron laboratory energies are E_0 and E_0+E at cooling and measurement, respectively, and the power supply voltage varies slowly (much slower than the switching frequency of the electron velocities) by 1 %, the change of the actually applied detuning energy is also 1 % ($\Delta E_0/E_0 \sim \Delta E_d/E_d$).

For two devices and two power supplies, the variations of v_i and v_e^{meas} are not correlated anymore and therefore the variations do not automatically compensate to a large degree. We have therefore coupled the two power supplies in the way that one delivers the acceleration voltage for one electron beam $U_0=E_0/e$ and the other one is stacked on top of this and only delivers the difference $U=E/e$ to the acceleration voltage of the other electron beam. In this case the variations can be reduced significantly.

To monitor longterm instability of the voltage between the two electron beams, scans around $E_d=0$ eV are included in each measurement (Sec. 3.4.4). Thus slow shifts of the position (acceleration voltage) of the 0 eV-peak, where ion velocity v_i and electron velocity in the target v_e are the same, can be identified. Only with the exact knowledge of this voltage it is possible to precisely calculate the detuning energies at which the measurement steps were spent during an energy scanning experiment. Slow drifts of the power supplies can be corrected for by dividing the measured data in to appropriate subsets with constant acceleration voltage at the $E_d=0$ eV-peak.

In Fig. 5.2, the DR rate normalized to the DE rate is plotted versus the acceleration voltage at the electron target for the peak around $E_d=0$ eV, for one measurement using the photocathode in the electron target. From the voltage at the peak position and the electron current measured at that point, the electron beam velocity and density are calculated after taking into account space charge corrections [Pot90]. In this way, slow drifts between the two beam devices were observed e. g. in the first measurements of HD^+ DR using the photocathode in the electron target. Fig. 5.3 gives an example of how the measured acceleration voltage for $E_d=0$ eV at the

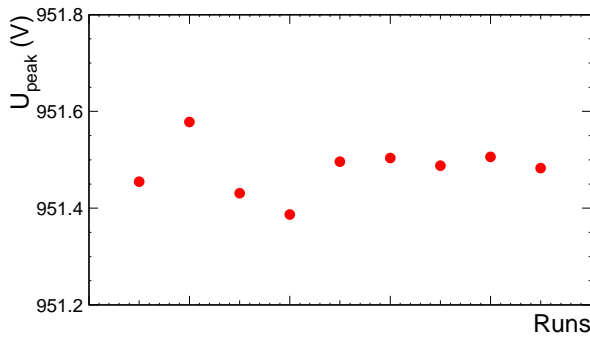


Fig. 5.3: Changes in the position of the HD^+ DR peak at $E_d=0$ eV in a series of measurements taken in October 2004, using the ultra-cold electron beam from the photocathode in the electron target and the electron cooler. The ion beam energy was $E_i=5.3$ MeV.

electron target changed in different measurements. Variations of 0.1 eV are found, that would lead to a 5 % error in the determination of the detuning energy at 4 meV, if they were not taken into account.

5.2 Improved energy resolution with electron target and photocathode

So far the best measurement of the energy dependence of the HD^+ DR rate coefficient with respect to energy resolution was performed in Stockholm at CRYRING [ARD⁺03]. A transverse electron temperature of $kT_{\perp}=2$ meV was realized and an absolute rate coefficient for the range from 0 to 30 eV was published.

With the new devices the relative DR rate coefficient of HD^+ was remeasured at the TSR and the results are compared to the data from CRYRING in Fig. 5.4. The CRYRING data is plotted in blue, the results obtained at the TSR using the electron target and a thermal cathode in red and the data measured, when the photocathode was applied in the electron target, are marked in green.

For the experiment making use of the LN-cooled photocathode at the electron target the ion beam energy was 5.3 MeV. The ion beam was phase space cooled by the electron cooler applying an electron density of $n_e=1.8 \cdot 10^7 \text{ cm}^{-3}$ and the electron density in the electron target at $E_d=0$ eV was $3.2 \cdot 10^5 \text{ cm}^{-3}$. The expansion factor was 40. The absolute normalization is done via the DR rate coefficient at the 9.8 eV peak, setting it to the value of $\alpha_{DR}(9.8 \text{ eV})=6.6 \cdot 10^{-9} \text{ cm}^3 \text{ s}^{-1}$ published by Al-Khalili *et al.* [ARD⁺03]. A very high energy resolution is reached in the measurement with the photocathode which is revealed by the stronger structures down to ~ 0.3 meV as compared to the CRYRING data.

In the measurement using the thermal cathode in the electron target the transverse electron temperature at cooling voltage E_{cool} was $kT_{\perp}=2.8$ meV ($kT_{\parallel}=45 \mu\text{eV}$) with an electron density of $n_e=2.85 \cdot 10^6 \text{ cm}^{-3}$ at an expansion factor of 40, so about a factor of 9 higher than in the measurement with the photocathode.. The ion beam energy was relatively low with $E_i=1.4$ MeV

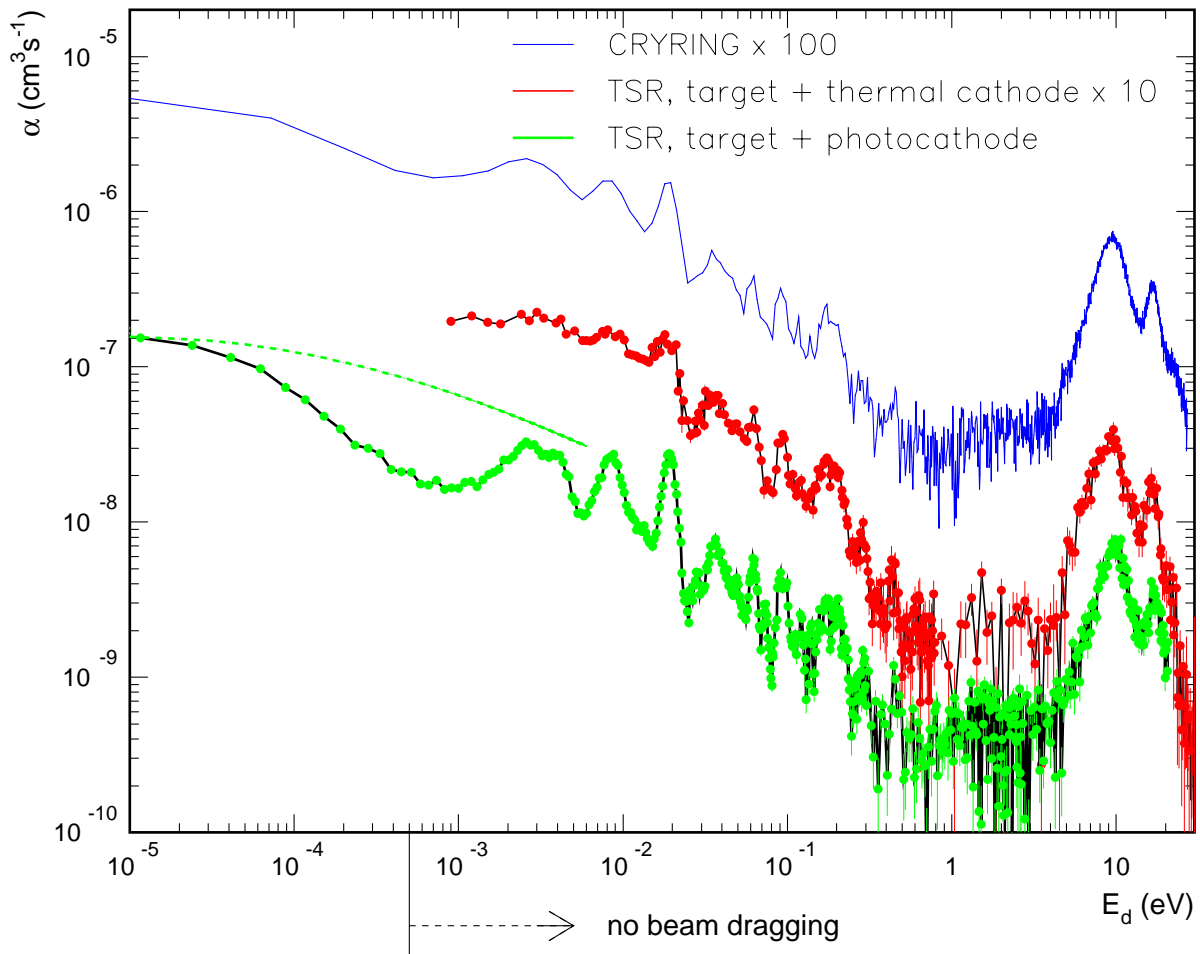


Fig. 5.4: DR rate coefficient of HD^+ as function of energy for 3 different measurements spanning 6 orders of magnitude in the detuning energy. Blue: CRYRING [ARD⁺03], $kT_{\perp}=2$ meV. Red: TSR with electron target and thermal cathode, $kT_{\perp}=2.8$ meV, 2 s and later after injection. Green: TSR with electron target and photocathode, $kT_{\perp}=0.6$ meV, $kT_{\parallel}=25$ μeV , 2 s and later after injection.. The blue and red data sets are scaled for clarity. The green dashed line is the rate coefficient to a model cross section $\sigma \sim A/E_d$ for the direct process folded with the electron temperature of the photocathode beam, matched to the measured rate coefficient at 10^{-5} eV.

and it was constantly phase space cooled by the electron cooler with an electron density of $5.5 \cdot 10^6 \text{cm}^{-3}$. As a result of the low beam velocity, DR rate coefficients at high detuning energies $E_d \geq 2$ eV will be measured too low for this particular case. This is because the kinetic energy release is so high for these detuning energies that for certain molecule orientations (i. e. the axis perpendicular to the beam velocity) at least the lighter fragment, the hydrogen, misses the $48 \times 48 \text{mm}^2$ surface barrier detector after approximately 11.5 m of flight path. The DR event thus will not be recognized correctly, but, if the deuteron hits the detector, accidentally mistaken

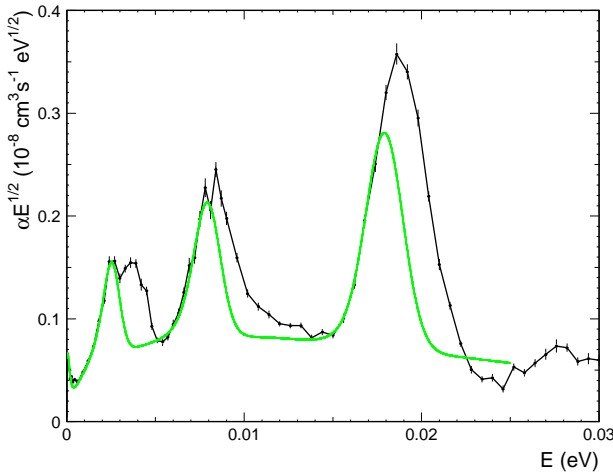


Fig. 5.5: Energy-scaled DR rate coefficient ($\alpha \cdot \sqrt{E}$) of HD^+ as function of energy for a measurement using the photocathode at the electron target (black). The green line is a rate coefficient calculated for 3 delta resonances on top of a $1/E$ dependent process convoluted with an electron temperature of $kT_{\perp}=0.6$ meV, $kT_{\parallel}=25$ μ eV [Orl06].

for a DE event; if neither particle hits, it will not be counted at all. The effect can be seen in Fig. 5.4. Therefore, the usual normalization to the DR rate at the vibrational peak at the reference energy of $E_d=9.8$ eV is not possible. Instead, the normalization was done in the low energy region of $E_d=1$ –200 meV, by scaling this DR rate coefficient by a certain factor. The factor was chosen so that dividing this rate coefficient by the one obtained with the photocathode yields an average of 1 over all measurement points in this range. The data presented here was taken between 2 and 10.5 s after the injection into the TSR.

The electron beam temperatures for these measurements with the photocathode were extracted from the data by fitting delta peak resonances folded with longitudinal and transversal electron temperatures to the low energy sides of the lowest 3 peaks in the DR spectrum (Fig. 5.5). The method is described in [OSL⁺05]. A transverse electron beam temperature of $kT_{\perp}=0.6(2)$ meV and a longitudinal temperature of $kT_{\parallel}=25$ μ eV can be found in this way¹. In measurements of the dielectronic recombination of Sc^{18+} , for which the resonance lineshapes can be well calculated by theory, the setup was measured to provide an electron beam with temperatures $kT_{\perp}=0.7(1)$ meV and $kT_{\parallel}=22(2)$ μ eV [Les06].

Folding a model cross section for the direct process $\sigma \sim 1/E_d$ with the found electron temperatures one obtains the rate coefficient marked by the green dashed curve in Fig. 5.4. It is scaled to match the value of the measured rate coefficient at $E_d=10^{-5}$ eV. One finds a steeper rise in the measured rate coefficient towards lowest energies as compared to the model. This is evidence for another structure in the range of 1 meV or below, the exact position depending on what level is the true direct process rate coefficient, i. e. if the structure is a peak or a dip.

For the comparison in the low energy region Fig. 5.6 focuses on the range up to $E_d=100$ meV. A

¹ This value is slightly higher than the previously published value [OSL⁺05], $kT_{\perp}=0.5$ meV and a longitudinal temperature of $kT_{\parallel}=20$ μ eV because of small changes in the analysis routines.

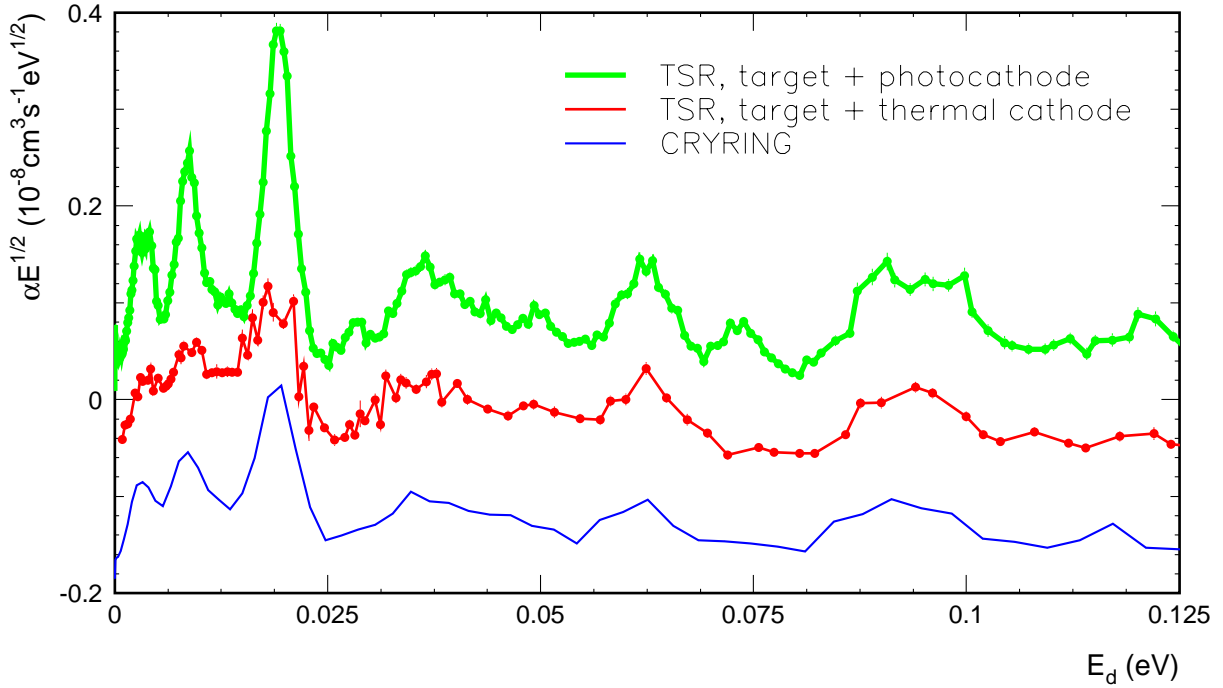


Fig. 5.6: Energy-scaled DR rate coefficient ($\alpha \cdot \sqrt{E}$) of HD^+ as function of energy for 3 different measurements. Green: TSR with electron target and photocathode, $kT_{\perp}=0.6$ meV, $kT_{\parallel}=25$ μeV . Red: TSR with electron target and thermal cathode, $kT_{\perp}=2.8$ meV, shifted down by $0.1 \cdot 10^{-8} \text{cm}^3 \text{s}^{-1} \text{eV}^{1/2}$ for clarity. Blue: CRYRING [ARD⁺03], $kT_{\perp}=2$ meV, shifted down by $0.2 \cdot 10^{-8} \text{cm}^3 \text{s}^{-1} \text{eV}^{1/2}$ for clarity.

scaled rate coefficient ($\alpha \cdot \sqrt{E_d}$) is plotted versus the detuning energy, to allow for a linear scale on the axis of ordinates. The colour code is the same as in Fig. 5.4

One finds that the rate coefficients from the two new experiments show all the peaks measured at CRYRING in this range at the same detuning energies. However, in the DR rate coefficient measured using the photocathode, the peaks are much sharper than in the other measurements and several additional structures are visible. There are peaks resolved which were not seen in the previous measurements. New peaks are found at 28, 50 and 73 meV. And the peak between 88 and 100 meV actually is composed of two peaks. All of these are very small structures and only visible due to the improved energy resolution.

Evidence for substructure is found in the lowest energy peak at $E_d=2.5$ meV. First, if one tries to fit a delta resonance folded with an electron temperature to this peak, one finds that it has to be much narrower than the measured peak to reproduce the steepness (Fig. 5.5). Second, one can identify two peaks at ~ 2.8 meV and ~ 3.5 meV (better seen in Fig. 5.4). The two next higher peaks are also wider in the experiment than the width due to the electron temperature, so that the underlying molecular processes determine the observed width.

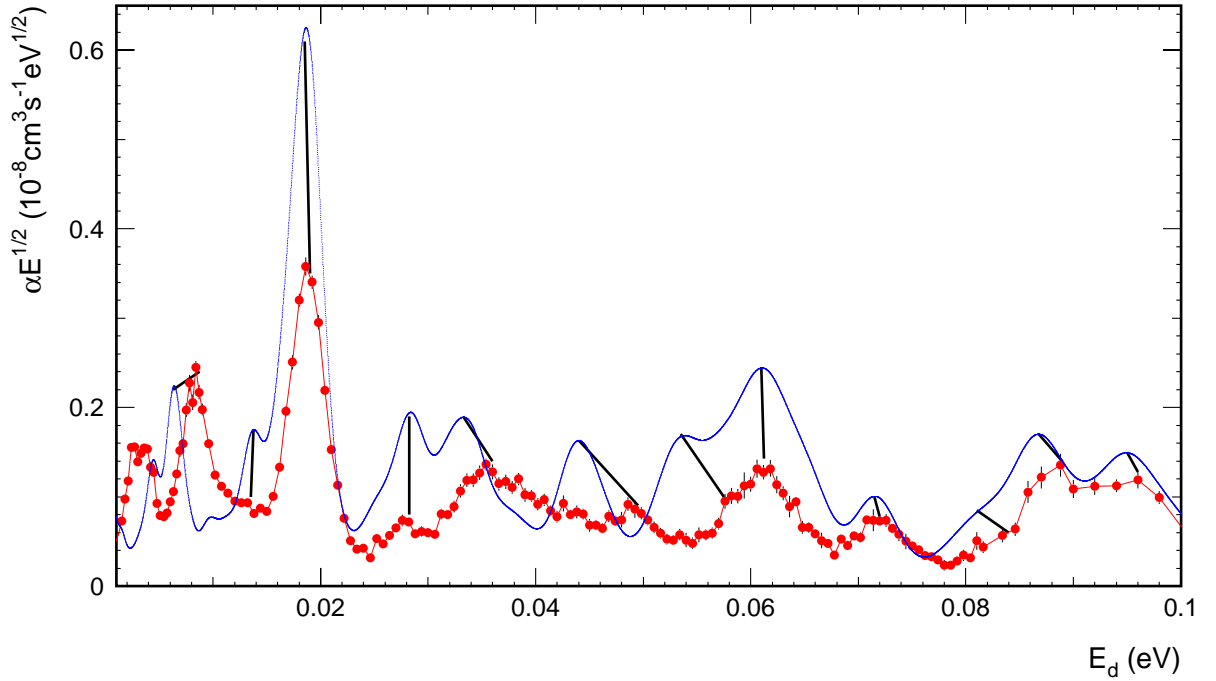


Fig. 5.7: Energy-scaled DR rate coefficient ($\alpha \cdot \sqrt{E}$) of HD^+ as function of energy from experiment and theory. Blue: Theoretical rate coefficient folded with electron temperature $T_{\perp}=0.5$ meV, $T_{\parallel}=20$ μeV (MQDT [Sch06]). Red: TSR with electron target and photocathode, $T_{\perp}=0.6$ meV, $T_{\parallel}=25$ μeV . The black lines indicate tentative correlations of peaks in the two rate coefficients.

So we have found three peaks that were not seen before, found an additional structure for $E_d \leq 1$ meV and shown that several peaks have some substructure. The ensemble of these observations opens up new possibilities for detailed comparison to theoretical calculations.

5.3 Comparison to MQDT

Theoretical calculations based on the MQDT formalism with rotational couplings as presented in [SSC⁺97] have succeeded to achieve an overall agreement with the low energy DR rate coefficient as it was measured at CRYRING [ARD⁺03]. With the detailed results in higher resolution and additional structures resolved, a new comparison is possible, especially in the very-low-energy region. The theory provides DR rate coefficients for the individual rotational levels of HD^+ in the vibrational ground state which will be discussed later (Fig. 5.11, Sec. 5.4). Using this method with updated molecular data, the total theoretical DR rate coefficient for a sample of HD^+ at any temperature (or other population of states) can be predicted. A calculation using a rotational temperature approximately equal to room temperature (300 K) yields the best

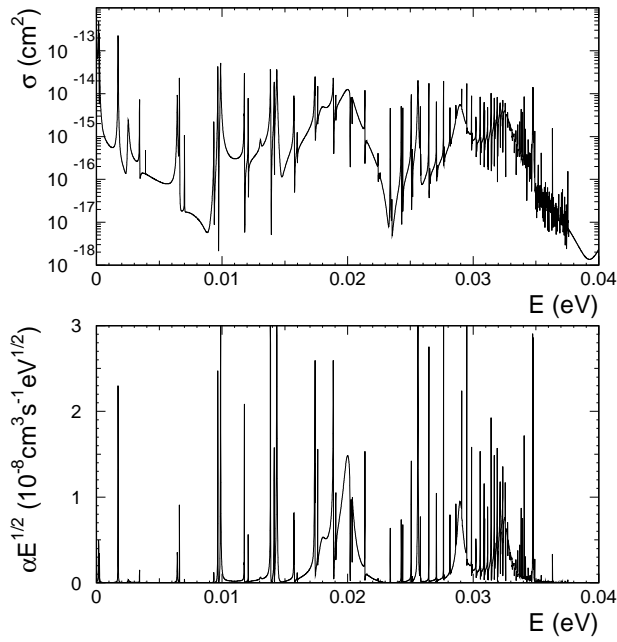


Fig. 5.8: The result of a MQDT calculation [SSC⁺97] for the cross section σ and the scaled DR rate coefficient $\alpha\sqrt{E_d}$ as a function energy. Rotational couplings are included. The initial rotational level of the molecular ion is $J=2$. The theoretical data is not convoluted with an electron temperature, i. e. it is given for infinite energy resolution. The convoluted scaled rate coefficient of this shown in Fig. 5.11.

agreement with the experimental results obtained with the photocathode at the TSR [Sch06]. Fig. 5.7 shows the comparison of the scaled rate coefficients of experiment and MQDT calculation as a function of the detuning energy in the range from 0 to 100 meV. The red curve depicts the experimental data taken with the photocathode, the blue curve is the calculated rate coefficient, folded with an electron temperature of $T_{\perp}=0.5$ meV and $T_{\parallel}=20$ μ eV.

Over all the range, the deviation in the DR rate coefficient between the two data sets is never bigger than a factor two and several features are very well reproduced, e. g. the peak at 19 meV. A detailed comparison peak after peak shows that, even if the absolute value of the rate coefficient is not perfectly matched in most places, the structures are very well reproduced. There are exactly 12 peaks present in the range from 5 to 100 meV in both curves. One can try to assign corresponding ones to each other as is done tentatively with the black lines in Fig. 5.7. This comparison shows that the theoretical peaks are always shifted to lower energies by 0 to 5 meV as compared to where they occur in the experiment. This agreement is very encouraging with respect to a future identification of the of the underlying molecular resonances.

As was seen in Sec. 2.5, the assignment of resonances is a difficult task due to the large number of possible contributors. Even to extract them from the theoretical calculations is a very time consuming process, because interference with non-resonant background and between the resonances mask the direct energy assignment and one has to compare results with certain resonances suppressed in the calculation which means a lot of computing time [Sch06].

To give an impression of the number of resonances occurring in the theoretical rate coefficient,

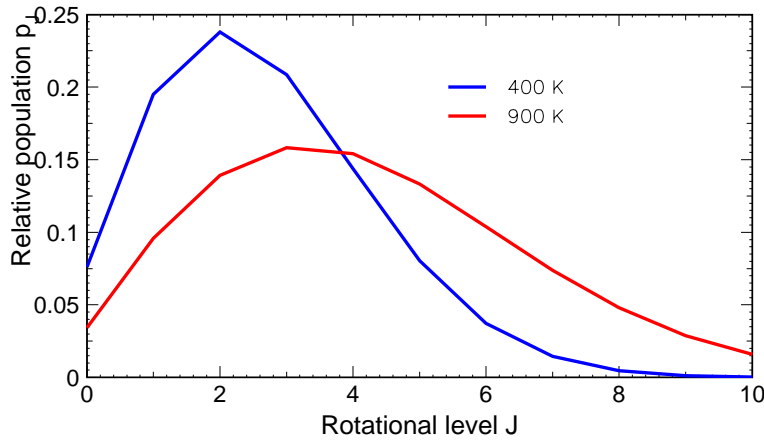


Fig. 5.9: Relative population distribution of rotational states in HD⁺ at temperatures of 400 K (blue) and 900 K (red).

Fig. 5.8 shows the calculated scaled rate coefficient without a convolution with the electron temperature for one single initial rotational state. In the range of 0 to 40 meV alone and for one initial rotational level, there is an infinite number of small resonances, because one Rydberg series ends at about 38 meV (compare to the dashed red lines in the Figs. 2.12, 2.13 and 2.14). Three very strong structures (20, 28, 32 meV) and three medium structures (11, 14, 25 meV) are visible. These structures remain observable after folding with the electron temperature (Fig. 5.11, $J=2$). Therefore concentrating the efforts on identifying these might seem useful as a next step. The labeling of the resonances is in progress [Sch06].

5.4 Time dependence in HD⁺ DR

The HD⁺ is produced at very high temperatures in a CHORDIS ion source [KNT89]. This means the molecular ions populate high vibrational and rotational levels when they are injected into the storage ring. The spontaneous vibrational deexcitation of HD⁺ is very fast – all vibrationally excited levels have lifetimes of less than 60 ms [AZF94]. The lifetimes of rotationally highly excited HD⁺ states in the vibrational ground state are below 0.5 s for $J \geq 6$ [AZF94]. Imaging experiments of the HD⁺ DR at BAMBI have shown that the rotational temperature after 3 s is below 600 K and that the asymptotic rotational temperature and the time to reach it depend on the electron density at cooling ($E_d=0$) [Noved]. The time to reach this level is shorter than 10 s and the asymptotic temperatures are ~ 400 K for $n_e=2.7 \cdot 10^6$ cm⁻³ and ~ 300 K for $n_e=1.5 \cdot 10^7$ cm⁻³, both measured at $E_i=1.4$ MeV.

Along with the rotational temperature also the relative populations p_J of the individual rotational levels changes. E. g. Fig. 5.9 illustrates the rotational populations for samples of HD⁺ molecular at 400 K and 900 K. One finds that p_J has a maximum at $J=2$ for 400 K, whereas the maximum is at $J=3$ for 900 K. When the temperature is reduced from 900 K to 400 K, p_J

is increased for $J=0-3$, while p_J decreases for $J \geq 4$.

The data measured with the electron target using the photocathode was split into four subsets based on the time of storage in the TSR. These sets are plotted together in Fig. 5.10. The purple curve depicts the scaled DR rate coefficient measured between 0.5 and 1.5 s after the injection, the black contains the data from 1.5 to 2.5 s, the red one that between 2.5 and 5 s and the blue curve for 5 to 10 s. There are only small differences visible in the comparison of these. The energies where these differences occur systematically are marked by a horizontal dashed line in Fig. 5.10.

The earliest data (purple) shows a DR rate coefficient which is a little smaller for the three lowest energy peaks at 3.5, 8.5 and 18.5 meV than the later sets. It also shows an additional peak in this range, at around 13 meV, which disappears for later times. At these early times, it might be traces of vibrational excitation or more probably high rotational states.

Further energies at which there is evidence for a time dependence are $E_d=24, 42, 54$ and 96 meV. At all these energies, there appear small peaks in the DR rate coefficient for short storage times which disappear in the following seconds. At 35 meV the rate coefficient seems to increase with time.

The phase space cooling might influence the earliest data set to a certain degree in the sense that there could be larger angles between ion beam and electron beam involved, but this should result in a broadening and shift of the peaks to lower detuning energies, not in the occurrence of new peaks. Phase space cooling of HD^+ is usually very fast (≤ 1 s) as we have seen in various imaging experiments ([Nov06]), and a shift is not observed here.

One can try to understand the time dependence observed in the experimental DR rate coefficient by comparison to the rate coefficients calculated with MQDT for the individual initial rotational levels of the molecular ion. The scaled rate coefficients obtained from these calculations are shown in Fig. 5.11 for ions in rotational levels $J=0-6$ in the vibrational ground state. The same energies as in Fig. 5.10 are marked by vertical dashed lines. If one now compares the energies at which a time dependence is observed with the rate coefficients for the single rotational states J , one can try to find the origin of the changing structures.

The two peaks at 3.5 and 8.5 meV that increase with time have no perfect match in the theoretical rate coefficients for those rotational levels (0-3) that increase in population for longer storage times (Fig. 5.9). The $J=1$ features a strong double peak between the two peaks in the experiment, making it the most likely source of the observed increase. It also fits that it increases over the full range of time, because this state is sensitive to changes in the temperature around 400 K, in the sense that its contribution to the total population changes much in absolute numbers.

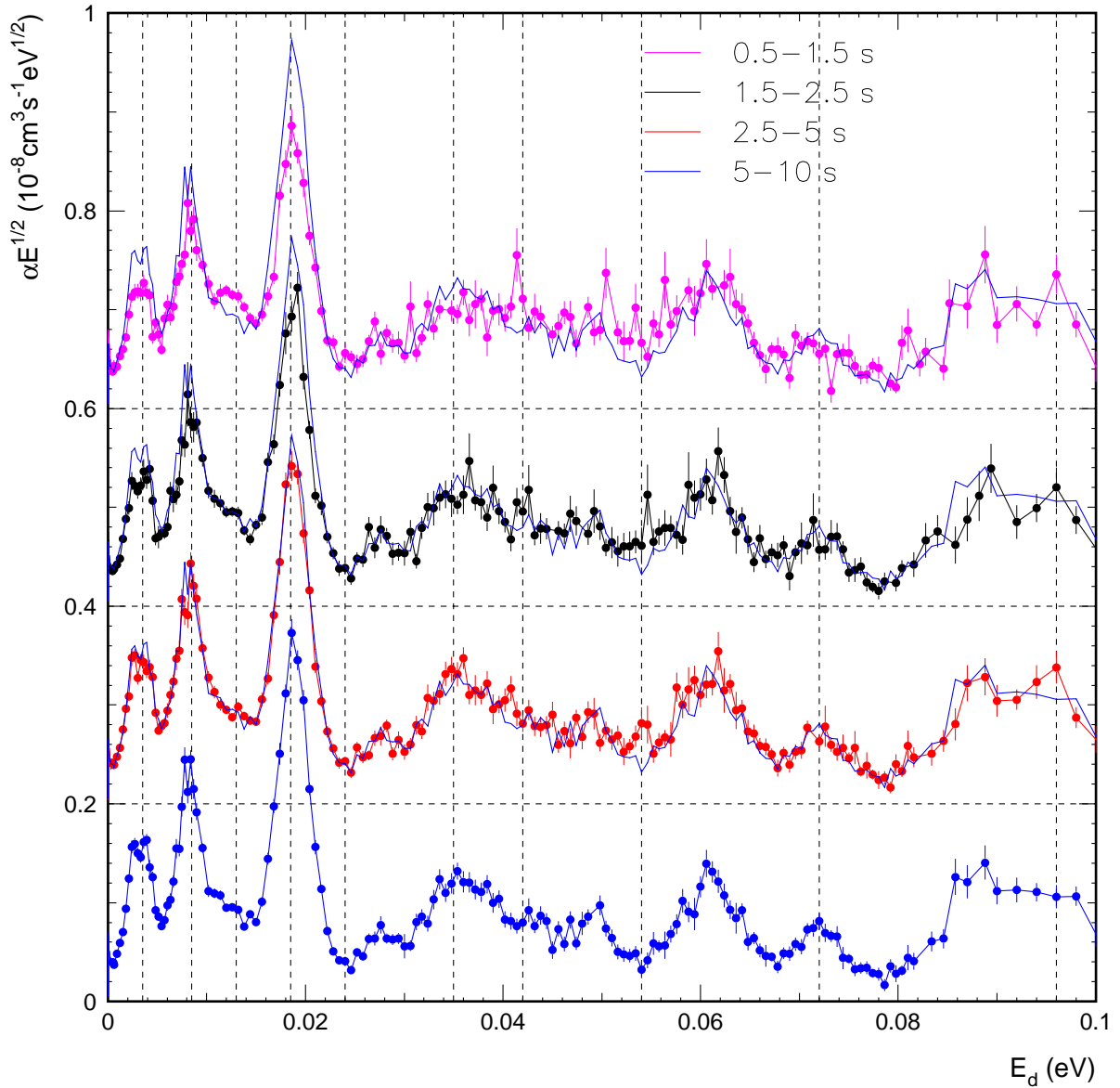


Fig. 5.10: Energy-scaled DR rate coefficient ($\alpha \cdot \sqrt{E}$) of HD⁺ as function of energy for 4 different storage time ranges, measured with the electron target and photocathode. Purple: Storage time 0.5–1.5 s, shifted up by $0.6 \cdot 10^{-8} \text{ cm}^3 \text{ s}^{-1} \text{ eV}^{1/2}$ Black: Storage time 1.5–2.5 s. shifted up by $0.4 \cdot 10^{-8} \text{ cm}^3 \text{ s}^{-1} \text{ eV}^{1/2}$ Red: Storage time 2.5–5 s. shifted up by $0.2 \cdot 10^{-8} \text{ cm}^3 \text{ s}^{-1} \text{ eV}^{1/2}$ Blue: Storage time 5–10 s. The shifts are made to improve the clarity. The dashed vertical lines indicate energies where there occur changes in the rate coefficient as the time increases. The blue thin line that is superimposed to all data sets is that for long storage times, to make comparison easier.

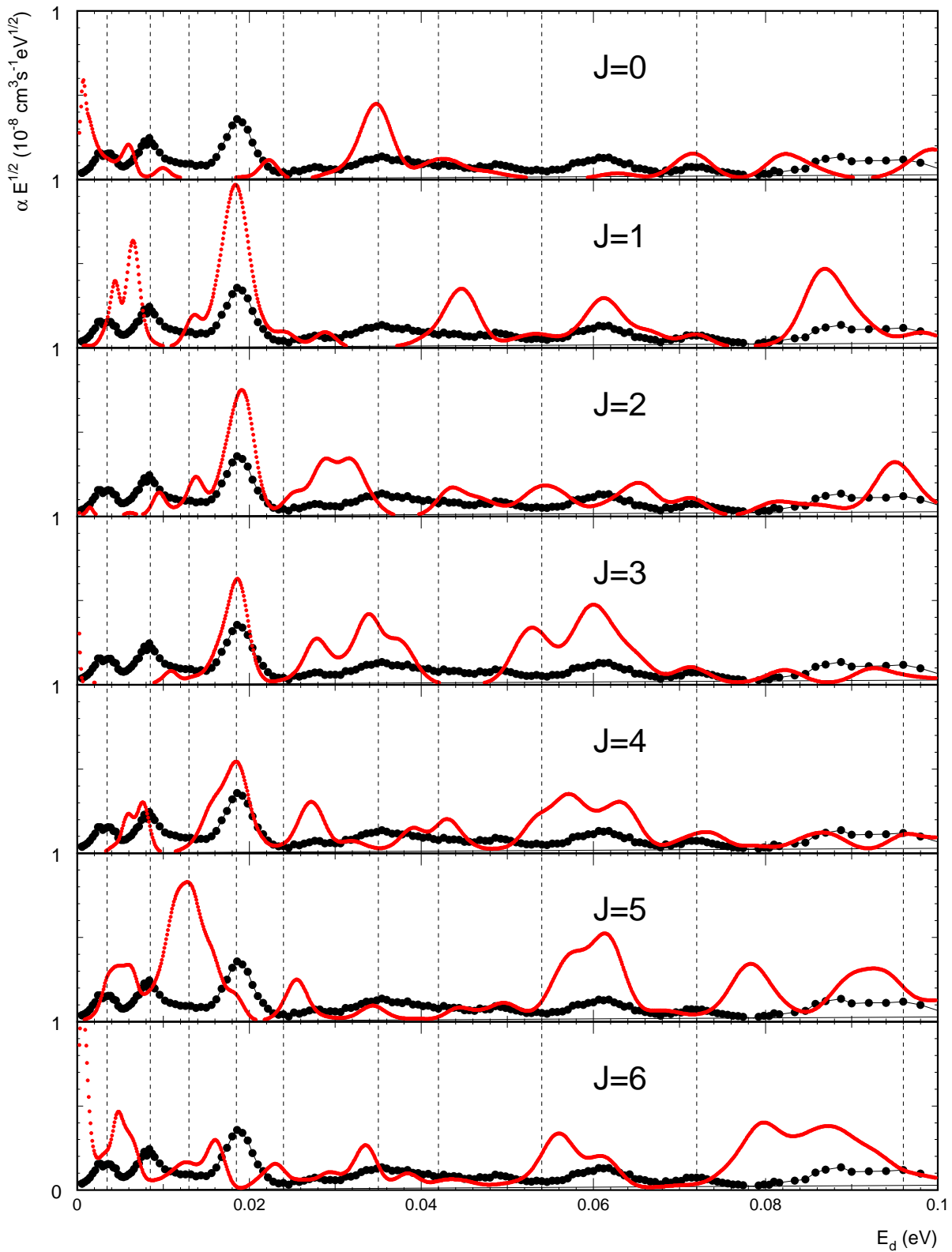


Fig. 5.11: Energy-scaled DR rate coefficient ($\alpha \cdot \sqrt{E}$) of HD^+ as function of energy. Black: Experimental DR rate coefficient acquired with electron target and photocathode. Red: MQDT-based calculated DR rate coefficient for individual rotational levels as initial molecular ion states in the ground vibrational state ($v=0$), for $J=0-6$. The dashed vertical lines mark the same detuning energies as in Fig. 5.10 for orientation.

Tab. 5.2: This table shows the radiative lifetimes of rotational levels in vibrational ground state HD⁺ as found in [AZF94].

	$J=1$	$J=2$	$J=3$	$J=4$	$J=5$	$J=6$
τ [s]	140.24	14.61	4.04	1.64	0.823	0.469

The peak at 13 meV is most probably due to the $J=5$ initial rotational state of HD⁺. The rate coefficient of this state features a huge peak at this energy, by far the biggest structure in this range for all the rotational levels under investigation here. It also fits that it disappears within 2.5 s, since the radiative lifetime of this level is only 0.8 s.

The most prominent peak in the whole energy range is the peak at 18.5 meV. This one increases significantly with time in the experimental rate coefficient. A comparison with the theoretical rate coefficients offers a very good explanation: All rotational levels between $J=4$ and $J=1$ have a strong peak at this energy, which is the higher, the lower J is. So a peak composed from the theoretical rate coefficients will get higher for lower temperatures. With the four strong peaks at almost exactly the same energy, this is a strong candidate for one of the $\Delta J=0$ resonances that were described in Sec. 2.5.3. This model, and also other predictions ([TKK⁺95],[SSC⁺97]) before, place a resonance with the ($n_{Ryd}=8, v=1$) Rydberg level approximately at this energy. The reason that it is not present in the $J=0$ might be that $J=0$ is a special case in the sense of the addition of angular momentum of molecular ion and incoming electron. Coupling to a $J=0$ ion state to a $J=0$ Rydberg state is only possible with an incoming s-wave electron, not with a d-wave electron, but whether this is the reason for the disappearance of the peak needs to be checked [SSC⁺97].

The very small change at 24 meV could arise from both the $J=5$ and $J=6$ states. The peak at 35 meV is slowly growing, and only very little. This might be due to an increase of the populations in $J=0$ or $J=3$. At 42 meV no rotational state is contributing strongly, but the most likely one to explain the very small decrease is $J=4$.

At 54 meV $J=3$, $J=4$ and $J=6$ have a high rate coefficient. The fact that the structure vanishes in the step from 5 to 10 s makes the $J=4$ the most likely candidate to be responsible for the peak that disappears – the population $p_{J=3}$ of $J=3$ was found to increase in the cooling down of a thermal population distribution in the temperature range of 900 K to 400 K, and $J=6$ can be expected to have reached a thermal equilibrium.

At 72 meV a slow increase is observed. Several rotational levels contribute here – $J=0-4$ –, but the $J=0$ is predicted to have the highest rate coefficient. However, all these levels are

significantly represented in a 400 K sample of HD⁺ ions. Showing almost the same energy for all levels this is another candidate for the $\Delta J=0$ resonances, although it does not match with one of the predicted energies in Fig. 2.15. This, however, is not a strong argument, given the simplifications included in the model underlying that figure.

5.5 Summary

We have shown that the application of the new electron target with the photocathode improves strongly the energy resolution with which a DR rate coefficient can be measured (Sec. 5.2). The electron beam temperatures were shown to be approximately $kT_{\perp}=0.6$ meV and $kT_{\parallel}=25$ μ eV. The improved energy resolution allowed to make visible several new structures in the low-energy region of the HD⁺ dissociative recombination, one even below 1 meV, and substructure e. g. in a peak at 3.5 meV (Figs. 5.4 and 5.6).

The first observation of the time dependence of the DR rate showed even more structures, one at $E_d=13$ meV vanishing within 2–3 s. It is possible to explain the changes with time as cooling of rotational excitation of the stored molecular ion sample. Comparing to the DR rate coefficients for the individual rotational levels of HD⁺ provided by MQDT [SSC⁺97] one finds changes where a population with a high rate coefficient changes significantly in population, as was shown in Sec. 5.4.

The theory is also successful in qualitatively modeling the low energy region with all its structures (Fig. 5.7), i. e. one observes the same number of peaks and only a small (consistent) shift in the peak energies. A couple of resonances were preliminarily assigned to arise either from certain rotational levels (i. e. the time dependent ones), or to resonances with $\Delta J=0$ like predicted by the simple model in Sec. 2.5 in the 'cold' rate coefficient.

6. Summary and outlook

The influence of rotational and vibrational excitation of molecular ions on electron collisions, especially on dissociative recombination was studied in this work for two systems, He_2^+ and HD^+ . Also the influence in the opposite direction, electron collisions acting on the vibrational excitation, was observed and analyzed carefully. By the construction of a new detection beam-line for neutral molecular fragments it became possible for the first time to use the electron target to measure molecular DR.

6.1 He_2^+ as a probe for rovibrational excitation

The He_2^+ system was shown to be ideally suited for observing even small changes in the vibrational states populations due to the high sensitivity of the DR rate coefficient for the initial vibrational state. The absolute rate coefficient for DR of vibrational ground state and excited $^4\text{He}_2^+$ was measured, and a factor of about 100 was found between them in qualitative agreement with the predictions due to the changes in the Franck-Condon overlap for these states with the dissociative state. A vibrational SEC rate coefficient was found for the $v=1$ to be about $\alpha_{SEC}^{v=1} = 1.8 \cdot 10^{-7} \text{cm}^3 \text{s}^{-1}$.

Inelastic collisions with electrons of a few eV were shown to excite He_2^+ vibrationally (Sec. 4.4). A distinct energy dependence was observed, with a maximum at approximately $E_d=4$ eV, similar for both isotopomers. This peak lies lower than the maximum rate coefficient observed for the DR, which is at about 7.3 eV. Rovibrational excitation by residual gas collisions was also observed (Sec. 4.5), thanks to the high sensitivity of the DR rate coefficient for vibrational excitation.

The energy dependent DR rate coefficient of $^4\text{He}_2^+$ was measured for several storage time intervals, showing a strong time dependence. Cold $^4\text{He}_2^+$ and $^3\text{He}^4\text{He}^+$ [PBA⁺05] show almost identical structures in the region of $E_d=1-40$ eV. Comparison with another storage ring experiment and theory show good agreement in the range between 1 and 15 eV considering the shape. The absolute DR rate coefficients measured at the TSR are about a factor of 2.5 higher than the other results.

Further structures in the range of $E_d=19\text{--}30$ eV were found and neutral and ionic states connected to atomic limits with two excited He-atoms or excited He-atom + He-ion were shown to be accessible in this energy region. Here calculations from the theoretical side are needed for comparison.

6.2 Improvement of the energy resolution seen with DR of HD^+

The electron target with the ultra-cold photocathode were taken into operation for molecular ion beams. The advantages of measuring DR rate coefficients using two electron beams at the same time – one for phase space cooling and one for the rate measurements – were demonstrated. Very low relative energies between electrons and stored molecular ions can be precisely set, decreasing the lower limit for reliable measurements of rate coefficients as function of energy. The improvement of the energy resolution in low-energy DR rate coefficient measurements was demonstrated in a very convincing way with HD^+ . The electron beam temperature extracted from the experimental data was $k_B T_{\perp}=0.6(2)$ meV and $k_B T_{\parallel}=25$ μeV . Thanks to this several new resonances in the low-energy region were discovered, some only for very short storage times. These latter ones are 'fingerprints' of rotationally highly excited HD^+ ions that relax by radiative deexcitation. Comparison to the DR rate coefficients of individual rotational levels helped to identify the most probable initial rotational state for these structures. An exact labeling of the visible resonances in the theoretical rate coefficients is on the way. Some resonances seem to be finally assigned.

The theoretical rate coefficients can model the low energy region quite well qualitatively by assuming a reasonable rovibrational temperature of 300 K. The total number of observable resonances is reproduced and only a small, consistent shift in energy is found. But we are still a step away from reaching a precision that would allow to extract quantitative information on the presence of certain rotational levels in the ion beam. It would be nice to imagine a DR rate coefficient as function of energy having a 'colour' telling the temperature of the ions like the spectrum of a light source or a black body, or to be more exact, to be able to recognize that 'colour', since the rate coefficient is specific for the temperature, as the calculated DR rate coefficients for the individual notational levels in Fig. 5.11 suggest.

6.3 Opportunities with the new system

With the ultra-cold electron beam, systems with a rich low-energy structure in the DR rate coefficient should be remeasured to provide the best available input to theoretical studies. The

cold electron beam can also serve as target in 2d- and 3d-imaging experiments. These profit from the low electron beam temperature, because the electron energy distribution smears the observed kinetic energy releases. In carefully designed experiments, the imaging technique can separate the individual rotational states [Shaed].

The two electron beams allow for more studies with controlled excitation by electron collisions of one collision energy while observing the effect on the rate coefficients for another electron energy. One could try to excite metastable electronic states and observe ion-pair production or measure the final states distributions of DR from these. A large number of new experiments can now be performed, that before were either impossible or only achievable with strong restrictions and probably low duty cycles.

6.4 Future experiments

The ultimate dream of a molecular ion experiment is to work with molecules in a well defined initial state and working under well defined conditions. We have shown that the present storage rings can help a lot in the fulfillment of this dream by phase space cooling the ion beam to have a very narrow spatial and velocity distribution. The electron cooler and now the electron target with ultra-cold GaAs-photocathode provide electrons with a very well defined collision energy. Long storage times together with radiative deexcitation in infrared active species also work towards this goal by reducing the rovibrational excitation to a thermal distribution. In most cases this reduces the system to one vibrational level, the ground state, being populated, but several rotational levels remain at 300 K. As was shown in the ${}^4\text{He}_2^+$ measurements, collisions with residual gas ions lead to efficient vibrational reexcitation and this can also reintroduce rotational excitation in radiative decays. The cryogenic storage ring CSR which is currently under construction at the Max-Planck-Institut für Kernphysik in Heidelberg will offer an environment in which such studies can be taken to the extreme. At wall temperatures of 2 K the thermal rovibrational distribution will be completely dominated by a single state. And the residual gas pressure will be lower by orders of magnitude compared to the TSR which allows even longer storage times and reduces dramatically the number of reexciting collisions.

References

- [ABG⁺96] F. Albrecht, M. Beutelsbacher, M. Grieser, R. von Hahn, L. Knoll, R. Repnow, D. Schwalm, K. Tetzlaff, and R. Wester. Slow extraction at the Heidelberg Heavy Ion Storage Ring TSR. *Fifth European Particle Accelerator Conference (Barcelona)*, 3:2459, 1996.
- [AH91] J. Ackermann and H. Hogreve. Adiabatic calculations and properties of the He₂⁺ molecular ion. *Chem. Phys.*, 157:75, 1991.
- [ARD⁺03] A. Al-Khalili, S. Rosén, H. Danared, A. M. Derkach, A. Källberg, M. Larsson, A. Le Padellec, A. Neau, J. Semaniak, R. Thomas, M. af Ugglas, L. Viktor, W. Zoge, W. J. van der Zande, X. Urbain, M. J. Jensen, R. C. Bilodeau, O. Heber, H. B. Pedersen, C. P. Safvan, L. H. Andersen, M. Lange, J. Levin, G. Gwinner, L. Knoll, M. Scheffel, D. Schwalm, R. Wester, D. Zajfman, and A. Wolf. Absolute high-resolution rate coefficients for dissociative recombination of electrons with HD⁺: Comparison of results from three heavy-ion storage rings. *Phys. Rev. A*, 68:042702, 2003.
- [AZF94] Z. Amitay, D. Zajfman, and P. Forck. Rotational and vibrational lifetime of isotopically asymmetrized homonuclear diatomic molecular ions. *Phys. Rev. A*, 50:2304, 1994.
- [Bar68] J. N. Bardsley. Configuration interaction in the continuum states of molecules. *J. Phys. B*, 1:349 and 365, 1968.
- [BO27] M. Born and J. R. Oppenheimer. Zur Quantentheorie der Molekeln. *Annalen der Physik*, 84:457, 1927.
- [BPA⁺ed] H. Buhr, H. B. Pedersen, S. Altevogt, V. M. Andrianarijaona, H. Kreckel, L. Lam-mich, M. Motsch, D. Schwalm, D. Strasser, X. Urbain, D. Zajfman, and A. Wolf. Dissociative recombination of rovibrationally excited ⁴He₂⁺ in a storage ring. *journal not yet known*, to be published.

References

- [Coh76] J. S. Cohen. Diabatic-states representation for $\text{He}^*(n \geq 3)+\text{He}$ collisions. *Phys. Rev. A*, 13:86, 1976.
- [COS99] L. Carata, A. E. Orel, and A. Suzor-Weiner. Dissociative recombination of He_2^+ molecular ions. *Physical Review A*, 59:2804, 1999.
- [CR95] W. Cencek and J. Rychlewski. Many-electron explicitly correlated Gaussian functions. II. Ground state of the helium molecular ion He_2^+ . *J. Chem. Phys.*, 102:2533, 1995.
- [DMCL76] R. Deloche, P. Monchicourt, M. Cheret, and F. Lambert. High-pressure helium afterglow at room temperature. *Physical Review A*, 13:1140, 1976.
- [ES99] B. D. Esry and H. R. Sadeghpour. Adiabatic formulation of heteronuclear hydrogen molecular ion. *Physical Review A*, 60:3604, 1999.
- [GBD83] A. Giusti-Suzor, J. N. Bardsley, and C. Derkits. Dissociative recombination in low-energy $e\text{-H}_2^+$ collisions. *Physical Review A*, 28:682, 1983.
- [Giu89] A. Giusti. A multichannel quantum defect approach to dissociative recombination. *Journal of Physics B: Atomic, Molecular and Optical Physics*, 13:3867, 1989.
- [Gre74] T. S. Green. Intense ion beams. *Rep. Prog. Phys.*, 37:1257, 1974.
- [Gub83] S. L. Guberman. The doubly excited autoionizing states of H_2 . *Journal of Chemical Physics*, 78:1404, 1983.
- [HBB⁺89] D. Habs, W. Baumann, J. Berger, P. Blatt, A. Faulstich, P. Krause, G. Kilgus, R. Neumann, W. Petrich, R. Stokstad, D. Schwalm, E. Szmola, K. Welti, A. Wolf, S. Zwickler, E. Jaeschke, D. Krämer, G. Bisoffi, M. Blum, A. Friedrich, C. Geyer, M. Grieser, H. W. Heyng, B. Holzer, R. Ihde, M. Jung, K. Matl, W. Ott, B. Povh, R. Repnow, M. Steck, E. Steffens, D. Dutta, T. Köhl, D. Marx, S. Schröder, M. Gerhard, R. Grieser, G. Huber, R. Klein, M. Krieg, N. Schmidt, R. Schuch, J. F. Babb, L. Spruch, W. Arnold, and A. Noda. First experiments with the heidelberg test storage ring TSR. *Nuclear Instruments and Methods in Physics Research B*, 43:390, 1989.
- [HK73] E. Herbst and W. Klemperer. The Formation and Depletion of Molecules in Dense Interstellar Clouds. *Astrophysical Journal*, 185:505, 1973.

-
- [Hofed] J. Hoffmann. Ion-pair production at the TSR. *journal not yet known*, to be published.
- [HYP74] G. Hunter, A. W. Yau, and H. O. Pritchard. Rotation–vibration level energies of the hydrogen and deuterium molecule ions. *Atomic Data and Nuclear Tables*, 14:11, 1974.
- [IPS83] V. A. Ivanov, N. P. Penkin, and Y. E. Skoblo. Dissociative recombination of molecular He_2^+ ions. *Optics and Spectroscopy*, 54:552, 1983.
- [IS88] V. A. Ivanov and Y. E. Skoblo. Dissociative recombination in helium afterglow. *Optics and Spectroscopy*, 65:445, 1988.
- [JG72] A. W. Johnson and J. B. Gerardo. Recombination and Ionization in a Molecular-Ion-Dominated Helium Afterglow. *Physical Review A*, 5:1410, 1972.
- [KAB⁺00] S. Krohn, Z. Amitay, A. Baer, D. Zajfman, M. Lange, L. Knoll, J. Levin, D. Schwalm, R. Wester, and A. Wolf. Electron–induced vibrational deexcitation of H_2^+ . *Phys. Rev. A*, 62:032713, 2000.
- [KLG⁺01] S. Krohn, M. Lange, M. Grieser, L. Knoll, H. Kreckel, J. Levin, R. Repnow, D. Schwalm, R. Wester, P. Witte, A. Wolf, and D. Zajfman. Rate coefficients and Final States for the Dissociative Recombination of LiH^+ . *Phys. Rev. Lett.*, 86:4005, 2001.
- [KMM⁺05] H. Kreckel, M. Motsch, J. Mikosch, J. Glosík, R. Plašil, S. Altevogt, V. Andrianarijaona, H. Buhr, J. Hoffmann, L. Lammich, M. Lestinsky, I. Nevo, S. Novotny, D. A. Orlov, H. B. Pedersen, F. Sprenger, A. S. Terekhov, J. Toker, R. Wester, D. Gerlich, D. Schwalm, A. Wolf, and D. Zajfman. High-Resolution Dissociative Recombination of Cold H_3^+ and First Evidence for Nuclear Spin Effects. *Physical Review Letters*, 95:263201, 2005.
- [KNT89] R. Keller, B. R. Nielsen, and B. Torp. Metal beam production using a high current ion source. *Nuclear Instruments and Methods in Physics Research B*, 37/38:74, 1989.
- [Kro02] S. Krohn. *Inelastic collisions and recombination between electrons and molecular ions*. PhD thesis, Universität Heidelberg, 2002.

References

- [KTS⁺98] H. Kubo, H. Takenaga, T. Sugie, S. Higashijima, S. Suzuki, A. Sakasai, and N. Hosogane. The spectral profile of the D_α line emitted from the divertor region of JT-60U. *Plasma Physics and Controlled Fusion*, 40:1115–1126, 1998.
- [Lan01] M. Lange. *Competition between Reaction Channels in Electron Collisions of the Hydrogen Molecular Ion HD^+* . PhD thesis, Universität Heidelberg, 2001.
- [Lar97] M. Larsson. Dissociative Recombination with ion storage rings. *Annual Review of Physical Chemistry*, 48:151, 1997.
- [LBK⁺04] L. Lammich, H. Buhr, H. Kreckel, S. Krohn, M. Lange, D Schwalm, R. Wester, A. Wolf, D. Strasse, D. Zajfman, Z. Vager, I. Abril, S. Heredia–Avalos, and R. Garcia–Molina. Coulomb–explosion imaging of CH_2^+ : Target–polarization and bond–angle distribution. *Phys. Rev. A*, 69:062094, 2004.
- [LCD⁺94] M. Larsson, M. Carlson, H. Danared, L. Broström, S. Mannervik, and G. Sundström. Vibrational cooling of D_2^+ in an ion storage ring as revealed by dissociative recombination measurements. *Journal of Physics B: Atomic, Molecular and Optical Physics*, 27:1397, 1994.
- [LDZ⁺00] Å. Larson, N. Djurić, W. Zong, C. H. Greene, A. E. Orel, A. Al-Khalili, A. M. Derkatch, A. Le Padellec, A. Neau, S. Rosén, W. Shi, L. Viktor, H. Danared, M. af Ugllas, M. Larsson, and G. H. Dunn. Resonant ion–pair formation in electron collisions with HD^+ and OH^+ . *Phys. Rev. A*, 62:042707, 2000.
- [Les06] M. Lestinsky. private communication. 2006.
- [Lesed] M. Lestinsky. *title not yet known*. PhD thesis, Universität Heidelberg, to be published.
- [LKL⁺03] L. Lammich, H Kreckel, M. Lange, H. B. Pedersen, S. Altevogt, V. Andrianarijaona, H. Buhr, O. Heber, P. Witte, D. Schwalm, A. Wolf, and D. Zajfman. Evidence fro Subthermal Rotational Populations in Stored Molecular Ions through State–Dependent Dissociative Recombination. *Phys. Rev. Lett.*, 91:143201, 2003.
- [LKS⁺00] J. Levin, L. Knoll, M. Scheffel, D. Schwalm, R. Wester, A. Wolf, A. Baer, Z. Vager, D. Zajfman, and V. Kh. Liechtenstein. Application of ultrathin diamond–like–carbon targets to Coulomb explosion imaging. *Nuclear Instruments and Methods in Physics Research B*, 168:268, 2000.

-
- [LO01] Å. Larson and A. E. Orel. Ion-pair formation and product branching ratios in dissociative recombination of HD^+ . *Phys. Rev. A*, 64:062701, 2001.
- [LWH⁺96] A. Lampert, A. Wolf, D. Habs, J. Kenntner, G. Kilgus, D. Schwalm, M. S. Pindzola, and N. R. Badnell. High resolution measurement of the dielectronic recombination of fluorine like selenium ions. *Phys. Rev. A*, 53:1413, 1996.
- [MGHO98] B. J. McCall, T. R. Geballe, K. H. Hinkle, and T. Oka. Detection of H_3^+ in the Diffuse Interstellar Medium Toward Cygnus OB2 No. 12. *Science*, 279:1910, 1998.
- [MGHO99] B. J. McCall, T. R. Geballe, K. H. Hinkle, and T. Oka. Observations of H_3^+ in Dense Molecular Clouds. *Astrophysical Journal*, 522:338, 1999.
- [MHS⁺04] B. J. McCall, A. J. Huneycutt, R. J. Saykally, N. Djuric, G. H. Dunn, J. Semaniak, O. Novotny, A. Al-Khalili, A. Ehlerding, F. Hellberg, S. Kalhori, A. Neau, R. D. Thomas, A. Paal, F. Österdahl, and M. Larsson. Dissociative recombination of rotationally cold H_3^+ . *Phys. Rev. A*, 70:052716, 2004.
- [NDH⁺02] A. Neau, A. Derkach, F. Hellberg, S. Rosén, R. Thomas, M. Larsson, N. Djurić, D. B. Popović, G. H. Dunn, and J. Semaniak. Resonant ion pair formation of HD^+ : Absolute cross sections for the $\text{H}^- + \text{D}^+$ channel. *Phys. Rev. A*, 65:044701, 2002.
- [NMF⁺03] V. Ngassam, O. Motapon, A. Florescu, L. Pichl, I. F. Schneider, and A. Suzor-Weiner. Vibrational relaxation and dissociative recombination of H_2^+ induced by slow electrons. *Phys. Rev. A*, 68:032704, 2003.
- [Nov04] S. Novotny. Fast-beam molecular fragmentation imaging using a high-speed gated camera system. Diplomarbeit, Universität Heidelberg. 2004.
- [Nov06] S. Novotny. private communication. 2006.
- [Noved] S. Novotny. HD^+ imaging. *journal not yet known*, to be published.
- [NTN87] K. Nakashima, H. Takagi, and H. Nakamura. Dissociative recombination of H_2^+ , HD^+ and D_2^+ by collision with slow electrons. *Journal of Chemical Physics*, 86:726, 1987.
- [OR06] A. E. Orel and J. Royal. private communication. 2006.

References

- [Orl06] D. A. Orlov. private communication. 2006.
- [OSL⁺05] D. A. Orlov, F. Sprenger, M. Lestinsky, U. Weigel, A. S. Terekhov, D. Schwalm, and A. Wolf. Photocathodes as electron sources for high resolution merged beam experiments. *Journal of Physics: Conference Series*, 4:290, 2005.
- [OWS⁺04] D. A. Orlov, U. Weigel, D. Schwalm, A. S. Terekhov, and A. Wolf. Ultra-cold electron source with a GaAs-photocathode. *Nuclear Instruments and Methods in Physics Research A*, 532:418, 2004.
- [paw] <http://paw.web.cern.ch>.
- [PBA⁺05] H. B. Pedersen, H. Buhr, S. Altevogt, V. M. Andrianarijaona, H. Kreckel, L. Lam-mich, N. de Ruelle, E. M. Staicu-Casagrande, D. Schwalm, D. Strasser, X. Urbain, D. Zajfman, and A. Wolf. Dissociative recombination and low-energy inelastic electron collisions of the helium dimer ion. *Phys. Rev. A*, page 012712, 2005.
- [PHT⁺05] A. Petrigiani, F. Hellberg, R. D. Thomas, M. Larsson, P. C. Cosby, and W. J. van der Zande. Electron energy-dependent product state distributions in the dissociative recombination of O_2^+ . *Journal of Chemical Physics*, 122:4311, 2005.
- [Pot90] H. Poth. Electron cooling: Theory, experiment, application. *Physics Reports*, 196:135–297, 1990.
- [PSG⁺96] S. Pastuszka, U. Schramm, M. Grieser, C. Broude, R. Grimm, D. Habs, J. Kennt-ner, H.-J. Miesner, T. Schüßler, D. Schwalm, and A. Wolf. Electron cooling and recombination experiments with an adiabatically expanded electron beam. *Nu-clear Instruments and Methods in Physics Research A*, 369:11, 1996.
- [Rei05] S. Reinhardt. *Measurement of Time Dilation by Laser Spectroscopy with Fast Stored Lithium Ions*. PhD thesis, Universität Heidelberg, 2005.
- [Rep02] R. Repnow. Progress and upgrading of the Heidelberg high current injector. *Pra-mana – journal of physics*, 59:835, 2002.
- [RO05] J. Royal and A. E. Orel. Dissociative recombination of He_2^+ . *Phys. Rev. A*, 72:022719, 2005.
- [roo] <http://root.cern.ch>.

-
- [Sch99] M. Schnell. Designstudie eines frequenzvariablen 4-Rod-Beschleunigers als Moleküloneninjektor für den Heidelberger Speicherring. Diplomarbeit, Universität Heidelberg. 1999.
- [Sch06] I. F. Schneider. private communication. 2006.
- [Shaed] D. Shafr. Master's thesis, Weizmann Institute Rehovot, to be published.
- [SKE⁺03] G. Saathoff, S. Karpuk, U Eisenbarth, G. Huber, S. Krohn, R. Munoz Horta, S. Reinhardt, D. Schwalm, A. Wolf, and G. Gwinner. Improved test of time dilation in Special Relativity. *Physical Review Letters*, 91:190403, 2003.
- [SLO⁺04] F. Sprenger, M. Lestinsky, D. A. Orlov, D. Schwalm, and A. Wolf. The high-resolution electron-ion collision facility at TSR. *Nuclear Instruments and Methods in Physics Research A*, 532:298, 2004.
- [Spr04] F. Sprenger. *Production of cold electron beams for collision experiments with stored ions*. PhD thesis, Universität Heidelberg, 2004.
- [SSC⁺97] I. F. Schneider, C. Strömholm, L. Carata, X. Urbain, M. Larsson, and A. Suzor-Weiner. Rotational effects in dissociative recombination: theoretical study of resonant mechanisms and comparison with ion storage ring experiments. *Journal of Physics B: Atomic, Molecular and Optical Physics*, 30:2687, 1997.
- [SSM⁺06] E. W. Schmidt, S. Schippers, A. Müller, M. Lestinsky, F. Sprenger, M. Grieser, R. Repnow, A. Wolf, C. Brandau, D. Lukić, M. Schnell, and D. W. Savin. Electron-Ion Recombination Measurements Motivated by AGN X-Ray Absorption Features: Fe XIV Forming Fe XIII. *Astrophysical Journal*, 641:L157, 2006.
- [SSS⁺95] C. Strömholm, I. F. Schneider, G. Sundström, L. Carata, H. Danared, S. Datz, O. Dulieu, A. Källberg, M. af Ugglas, X. Urbain, V. Zengin, A. Suzor-Weiner, and M. Larsson. Absolute cross sections of dissociative recombination of HD⁺: Comparison of experiment and theory. *Phys. Rev. A*, 52:4320, 1995.
- [ST93] B. K. Sarpal and J. Tennyson. Calculated vibrational excitation rates for electron - H₂⁺ collisions. *Mon. Not. R. Astron. Soc.*, 263:909, 1993.
- [SUP⁺00] D. Strasser, X. Urbain, H. B. Pedersen, N. Altstein, O. Heber, R. Wester, K. G. Bhushan, and D. Zajfman. An innovative approach to multiparticle three-dimensional imaging. *Review of Scientific Instruments*, 71:3092, 2000.

References

- [Tak93] H. Takagi. Rotational effects in the dissociative recombination of $\text{H}_2^+ + e$. *Journal of Physics B: Atomic, Molecular and Optical Physics*, 26:4815, 1993.
- [TEG⁺02] M. Tokman, N. Eklöw, P. Glans, E. Lindroth, R. Schuch, G. Gwinner, D. Schwalm, A. Wolf, A. Hoffknecht, A. Müller, and S. Schippers. Dielectronic recombination resonances in F^{6+} . *Phys. Rev. A*, 66:012703, 2002.
- [TKK⁺95] T. Tanabe, I. Katayama, H. Kamegaya, K. Chida, Y. Arakaki, T. Watanabe, M. Yoshizawa, M. Saito, Y. Haruyama, K. Hosono, K. Hatanaka, T. Honma, K. Noda, S. Ohtani, and H. Takagi. Dissociative Recombination of HD^+ with an Ultracold Electron Beam in a Cooler Ring. *Phys. Rev. Lett.*, 75:1066, 1995.
- [TT72] S. Takezawa and Y. Tanaka. Absorption Spectrum of HD in the Vacuum–uv Region. Rydberg States and Ionization Energy. *The Journal of Chemical Physics*, 56:6125, 1972.
- [TTK⁺99] T. Tanabe, H. Takagi, I. Katayama, K. Chida, T. Watanabe, Y. Arakaki, Y. Haruyama, M. Saito, I. Noumra, T. Honma, K. Noda, and K. Hosono. Evidence for Superelastic Electron Collisions from H_2^+ Studied by Dissociative Recombination Using an Ultracold Electron Beam from a Cooler Ring. *Phys. Rev. A*, 83:2163, 1999.
- [UDS⁺05] X. Urbain, N. Djuric, C. P. Safvan, M. J. Jensen, H. B. Pedersen, L. Vejby Sjøgaard, and L. H. Andersen. Storage ring study of the dissociative recombination of He_2^+ . *Journal of Physics B Atomic Molecular Physics*, 38:43, 2005.
- [WAG⁺98] R. Wester, F. Albrecht, M. Grieser, L. Knoll, R. Repnow, D. Schwalm, A. Wolf, A. Baer, J. Levin, Z. Vager, and D. Zajfman. Coulomb explosion imaging at the heavy ion storage ring TSR. *Nuclear Instruments and Methods in Physics Research B*, 413:379, 1998.
- [Wes99] R. Wester. *Spatial structure of stored molecular ions by Coulomb explosion imaging*. PhD thesis, Universität Heidelberg, 1999.
- [Wis02] G. Wissler. *A detector system for charge-changing and fragmentational experiments on stored ions*. PhD thesis, Universität Heidelberg, 2002.
- [ZGKV92] D. Zajfman, T. Graber, E. P. Kanter, and Z. Vager. Influence of multiple scattering on the Coulomb–explosion imaging of fast molecules. *Phys. Rev. A*, 46:194, 1992.